Investigation of Antiferromagnetic Chromium and Dysprosium Using the Pump-Probe Type Method on a New Pulsed Magnetic Field Setup

DISSERTATION
zur Erlangung des Doktorgrades des Department Physik
der Universität Hamburg

vorgelegt von
M.Sc. Karina Kazarian

Hamburg
2023
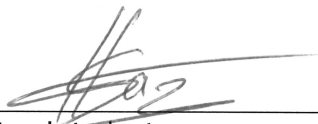
Declaration on oath

I hereby declare in lieu of oath that I have written this dissertation myself and that I have not
used any auxiliary materials or sources other than those indicated.

Hamburg, _8.06.2023_

_____
Signature of the doctoral student

Abstract

The growing amount of digital data requires the development of high-speed, low-power and high-density logic and memory electronic devices. Such technological progress requires a detailed understanding of the fundamental properties of the material and ways to manipulate them. One of the magnetic research areas which has great potential in solving the problem of big data storage is spintronics. Now ferromagnetic materials are the most common in spintronics, however, antiferromagnetic materials can overtake them due to the higher speed of spin switching, reduced noise level due to the low interaction between oppositely oriented spins. In the study of antiferromagnetic materials, the pump-probe method is often used with various pumping mechanisms: an optical laser, an electric current, or X-rays.

This project is focused on the first studies of antiferromagnetic materials using the pump-probe type method on a new Pulsed Magnet (PUMA) setup at MID instrument at Euroepan XFEL. For this research two different antiferromagnetic samples Dysprosium (Dy) and Chromium (Cr) were chosen to demonstrate the first application of the new method. Both samples feature structural change at low temperatures; however, Dy requires low magnetic field and Cr needs a high magnetic field to affect the spin direction.

The PUMA setup was successfully commissioned and several experiments were carried out. Using developed data analysis procedures, a temperature dependence for Dy lattice parameter agreed with theoretical expectations and phase diagram was confirmed. The evaluation of the the radiation damage was carried out using charge reflection of Cr sample, since both charge and magnetic reflections require significant X-ray energy for good signal to noise ratio. As a part of the confirmation of the magnetic nature of the found reflections, they were tracked along with the warming up over Neel temperature. Also the parameters of magnetic reflections were studied in the low temperature region of the spin polarization transition. Finally, both charge and magnetic reflections were tracked with application of magnetic field pulse up to 12.5 T above and below spin-flip transition temperature.

Zusammenfassung

Die ständig wachsende digitale Datenflut erfordert die Entwicklung von schnellen, effizienten elektronischen Logik- und Speicherbauteilen mit großer Speicherkapazität. Technologischer Fortschritt auf diesem Gebiet erfordert ein detailliertes Verständnis der mikroskopischen Materialeigenschaften und deren Manipulation. Eines der Forschungsfelder, das verspricht, das Problem große Datenmengen zu speichern, zu lösen, ist das Gebiet der Spintronics. Gegenwärtig werden hauptsächlich Ferromagneten unter Spintronic-Aspekten untersucht, allerdings könnten sich antiferromagnetische Materialien als überlegen erweisen weil sie schneller geschaltet werden können und einen größeren Rauschabstand aufweisen wegen der geringen Wechselwirkung zwischen gegensinnig orientiertes Spins. Antiferromagnetische Materialien werden oft mit der Pump-Probe-Methode untersucht, und zwar mit verschiedenen Anregungspulsen: denen eines optischen Lasers, mit elektrischen oder Röntgenpulsen.

Die vorliegende Forschungsarbeit konzentriert sich auf die ersten Untersuchungen von antiferromagnetischen Materialien mit der Pump-Probe-Methode an einem neuem Aufbau mit gepulstem Magneten (PUMA) an der MID-Endstation am European XFEL. Für die Experimente wurden die Antiferromagneten Dysprosium (Dy) und Chrom (Cr) ausgewählt um die erstmalige Anwendung dieses neuen Aufbaus und seiner Möglichkeiten zu demonstrieren. Beide Proben zeigen strukturelle Veränderungen bei tiefen Temperaturen, wobei Dy niedrige, Cr hingegen hohe magnetische Felder erfordert, um die Spinorientierung zu ändern.

Der PUMA-Aufbau wurde erfolgreich in Betrieb genommen und mehrere Experimente wurden mit ihm erfolgreich durchgeführt. Mithilfe eigens entwickelter Verfahren zur Datenanalyse, wurde die vorhergesagte Temperaturabhängigkeit der Gitterkonstante von Dy und sein Phasendiagramm experimentell reproduziert. Der Effekt von Strahlenschäden wurde anhand der Ladungsreflektion von Cr ermittelt, denn beide Proben verlangen sowohl in den Ladungs- als auch den magnetischen Reflektionen erhebliche Intensitäten in den Röntgenpulsen um einen guten Rauschabstand zu erzielen. Um die magnetische Natur dieser Reflektionen zu verifizieren, wurden sie beim Aufwärmen bis über die Neel-Temperatur beobachtet. Außerdem wurden die Parameter der magnetischen Reflektionen im Tieftemperaturregime des Spinpolarisierungsübergangs studiert. Zu guter Letzt wurden sowohl die Ladungs- als auch die magnetischen Reflektionen beim Anlegen magnetischer Felder bis zu 12.5 T gemessen, sowohl über als auch unter der Übergangstemperatur des Spin-Flips.

Contents

1 Introduction

The need for magnetic research is growing rapidly due to the widespread use of magnetic materials in various areas of life: from green energy development to big data storage. One of the important research areas is spintronics, which has the potential of providing high speed, low power and high density logic and memory electronic devices. In this regard, to create new and more efficient materials, one would need to understand the properties of the underlying materials and how to control these. Ferromagnetic materials have a permanent magnetic moment in the absence of an external field and can exhibit very large, permanent magnetisations. Antiferromagnets constitute a class of magnetic materials, which have no net magnetisation because the ordered moments are not aligned or even antiparallel between neighbouring atomic sites. For a long time, the essential features of antiferromagnets, such as: insensitivity to external fields, no interaction with neighbouring particles, short switching times, did not find wide application.

In his Nobel lecture Louis Neel noted that effects that depend on the square of the spontaneous (sublattice) magnetisation show the same variation in antiferromagnets as in ferromagnets [1].

In 1971 the very first experiment showing the manipulation and readout of antiferromagnetic ordering was conducted: W.B. Muir and J.B. Strom-Olsen observed that the electrical resistance of a Chromium single-crystal depends on how the sample was magnetically prepared [2]. The anisotropic magnetoresistance was studied at the same time in ferromagnets by T. McGuire and R. Potter [3] and was found to be an even function of the magnetic moment. It remains an open question whether antiferromagnets could overtake ferromagnets in the race for more efficient magnetic storage devices.

There are two main arguments supporting the future use of antiferromagnetic devices. The first is the stability of multiple magnetic configurations and reduced stray field that may interact with neighboring bits. Above the spin-flop field, the antiferromagnetic moments switch to align perpendicular to the field, resulting in constant susceptibility. On the other hand, in ferromagnets, magnetisation is reoriented by an external magnetic field proportional to the anisotropy. In common materials relativistic or dipolar magnetic anisotropy fields are many orders of magnitude weaker than exchange fields (also called molecular fields in Weiss model). Therefore, antiferromagnets generate zero stray fields, and thus eliminate unwanted magnetic crosstalk between neighbouring devices, but also provide magnetic storage that is robust against magnetic

field perturbations. The second argument is the faster spin switch of antiferromagnets. Reorientation of antiferromagnetic moments involves turning of the two spin sublattices from their equilibrium antiparallel state, which costs exchange energy. The zero-field resonance frequency of an antiferromagnet $\omega_{\text{AFM}} \approx \gamma\sqrt{2B_E B_A}$, where B_E exchange field and B_A anisotropic field. In ferromagnets, reorientation of the magnetisation does not involve relative movement of the moments; thus, the energy cost is related only to magnetic anisotropy $\omega_{\text{FM}} \approx \gamma B_A$ [4]. As a result, antiferromagnets typically have much faster dynamics than ferromagnets [5].

For the purpose of applications of antiferromagnets, it is essential to have a comprehensive understanding of antiferromagnetic dynamics at the microscopic level. The new phenomena may appear at high fields (for a review, see [6]) which can be studied by X-ray diffraction techniques [7]. In many studies of magnetic materials properties, it is necessary to change the temperature and/or the applied magnetic field during the measurements. A common method in ultrafast demagnetisation science is the pump-probe technique, when a pumping source triggers dynamics in the sample and then it is probed by X-rays. There are several pumps/triggers widely used: optical laser [8], electrical current [2] or X-rays. Here, the novelty of this project is the use of a magnetic field as a probe. This new approach will allow us to separate the effect of temperature and structural changes from purely magnetic effects in the sample.

X-ray and neutron diffraction under high magnetic fields already attracted a lot of attention worldwide: two Japanese groups are developing pulsed field installations for synchrotron experiments at Spring-8 [9]. Both groups employ split-pair coils in Voigt geometry, i.e., with the incident beam perpendicular to the magnetic field, which is preferable for single-crystal diffraction experiments. Another example of such a device, which also motivated this project, is a miniature pulsed magnet system on the beamline ID18 at European Synchrotron Radiation Facility (ESRF [10]). This split-pair coil has been successfully used for different X-ray spectroscopy experiments up to 30 T [11]. The combination of a relatively high magnetic fields, compact size, and temporal resolution motivated us to build a similar setup.

The European XFEL has a combination of properties that are attracting the attention of an increasing number of scientists around the world: the high repetition rate (4.5 MHz), photon energy range (3 - 25 keV), peak brilliance, beam coherence and beam duration.The linear accelerator equipped with superconducting niobium cavities provides provides electrons to three undulators, which serve six dedicated beamline instruments covering soft and hard X-rays. One of the hard X-rays instruments is "Materials Imaging and Dynamics" (MID), which started its operation in 2019 [12]. A number of different techniques were already demonstrated for studying various types of samples: coherent X-ray diffraction imaging (CXDI), X-ray photon correlation spectroscopy (XPCS), and time-resolved pump-probe X-ray scattering. Some experiments require special sample environments including low temperatures and applied magnetic fields.

Therefore, custom instrumentation for this project was needed to be located at the endstation of the MID beamline.

Hence, this project is focused on the first studies using the new Pulsed Magnet (PUMA) setup and developing a new type of pump-probe method. For this research two different antiferromagnetic samples Dysprosium (Dy) and Chromium (Cr) were chosen to demonstrate the first application of the new method. Both crystals feature structural change at low temperatures, however Dy require low magnetic field and has well-know magnetic phase diagram and Cr need high magnetic field to affect the spin direction and the magnetic phase diagram at high fields is still very poorly understood. Much of the experimental part of this project is devoted to studying the relationship between charge (CDW) and spin density waves (SDW), which remains a controversial topic, especially in a Cr crystal with a three-dimensional SDW. Thus, choice of these two sample is motivated by both demonstrating successful first operations of the new PUMA setup and at the same time to gain new insight in the magnetic properties of the materials by X-ray diffraction.

The thesis is structured as follows: in Chapter 2 an overview of the European XFEL and the MID instrument is given with its main properties and devices employed for this project. Chapter 3 provides a detailed description of the PUMA setup, including the manufacturing of the split-pair coil magnet, the cryostat operation, manipulations of the sample, software operation, synchronisation with X-ray, and future improvements. In Chapter 4, a brief overview of the theoretical basis underlying antiferromagnetic systems, phase transitions, and spin and charge density waves is given. The experimental method is introduced in Chapter 5 including the fundamentals of X-ray diffraction and in particular the case of non-resonant magnetic X-ray scattering. In Chapter 6 we describe the of sample preparation and characterization process, including ancillary measurements to verify the characteristics of the single-crystalline samples and parts of the setup. The technical aspects of experiments, which were carried out in the frame of this project are briefly given in Chapter 7, followed by presentation of the data processing and the main results in Chapter 8. Finally, in Chapter 9 conclusions and outlook are given.

2 European XFEL and MID instrument

Figure 2.1: A first medical X-ray picture of Roentgen's wife hand.

This year marks the one hundred year anniversary of the death of the pioneer X-ray scientist Wilhelm Conrad Roentgen, who in 1895 discovered X-ray radiation while working on cathode tubes. He was the first scientist to receive the Nobel Prize in Physics in 1901. Since then, not a single scientific overview work in the X-ray field has been complete without the first medical X-ray picture of Roentgen's wife hand. And this work is no exception (Figure 2.1). In 1912 a one-page report from the Bavarian Academy of Sciences announced the discovery of X-ray diffraction by crystals. Using X-ray radiation with photographic plates placed left, right, and behind the crystal the diffraction pattern of cubic crystalline ZnS was recorded. For this

experiment Max von Laue received the Nobel Prize in physics in 1914 "for his discovery of the diffraction of X-rays by crystals". Shortly afterwards in England, William Henry Bragg and William Lawrence Bragg, father and son, developed an alternative method, which confirmed the discovery. They received the Nobel Prize in 1915 "for their services in the analysis of crystal structure by means of X-rays". Bragg demonstrated that the diffraction pattern was due to the reflection of the "white Bremsstrahlen" from the crystal planes. The selection rule that determines the wavelengths that cause the diffraction patterns of a particular set of crystal planes became known as the Bragg condition. It took a few more months to show the equivalence of Laue's and Bragg's approaches.
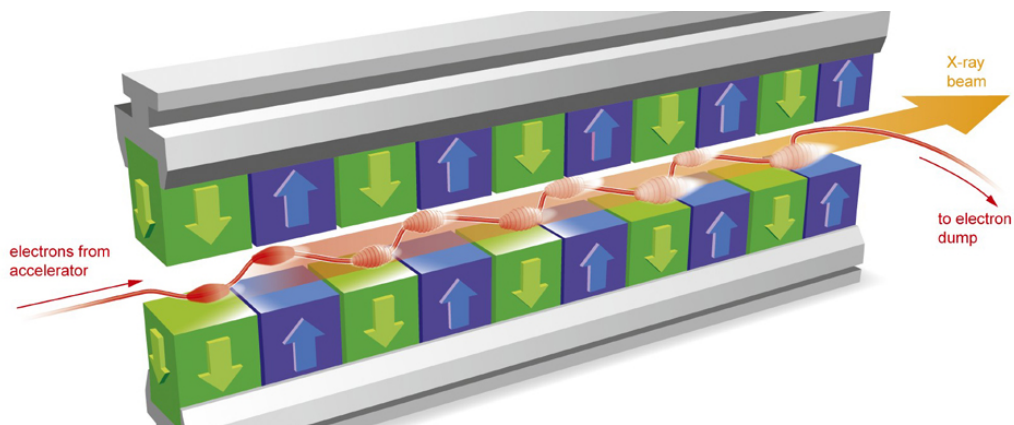

Figure 2.2: The undulator contains arrays of permanent magnets with alternating polarities. While travelling along the device the accelerated electrons have sinusoidal trajectory, split into groups, and emit highly coherent and brilliant X-ray [13].

Since then, X-ray generating devices have been developed rapidly with the aim of improving both the overall radiation quality and the use of a multitude of radiation characteristics. From common X-ray tubes or rotating anodes of different materials, which is used in crystallography laboratories, some experiments moved to the large synchrotron radiation facilities, whichconsist of a particle accelerator coupled with a storage ring, where they are maintained. The electrons are accelerated by a linear accelerator, enter a booster ring with small radius for the next stage of acceleration and afterwards enter into the storage ring. In first generation synchrotron radiation facilities the X-ray radiation are generated by the bending magnets keeping the electrons in the storage ring orbit. When electrons travel through a magnetic field with close to relativistic speed it deviates from a straight path according to the Lorenz force and in turn emit radiation in a narrow cone. This X-ray radiation (beam) is used in the experimental stations (beamlines with endstations) distributed around the storage ring. Next-generation synchrotrons have been upgraded with undulators, which consists of a series of evenly spaced magnets with an alternat-

ing magnetic field direction (up-down). While travelling along this insertion device, an electron undergoes a sinusoidal trajectory in the horizontal plane and emits electromagnetic waves that interfere constructively with higher coherence and brilliance than the bending magnet radiation. With proper combination of such parameters as the undulator length and small electron beam emittance, magnetic fields and undulator gap etc., the emitted radiation interacts with the electron bunch. This principle of self-amplification of spontaneous emission (SASE) defines a new type of big radiation source facilities namely X-ray Free-Electron Lasers (FELs). The key point of the SASE principle is that the emitted electric field travels faster than the electron bunch, and some part of electron bunch is slowed down as a result of the interaction with the field and another part is accelerated. Thus, from a random spatial distribution (dilute electron gas) the electron bunches are split into groups ("microbunches") (Figure 2.2). Since these microbunches emit synchronously and in phase the resulting radiation has a large transverse coherent length, extreme brightness (Figure 2.3), and a temporal structure of short flashes.
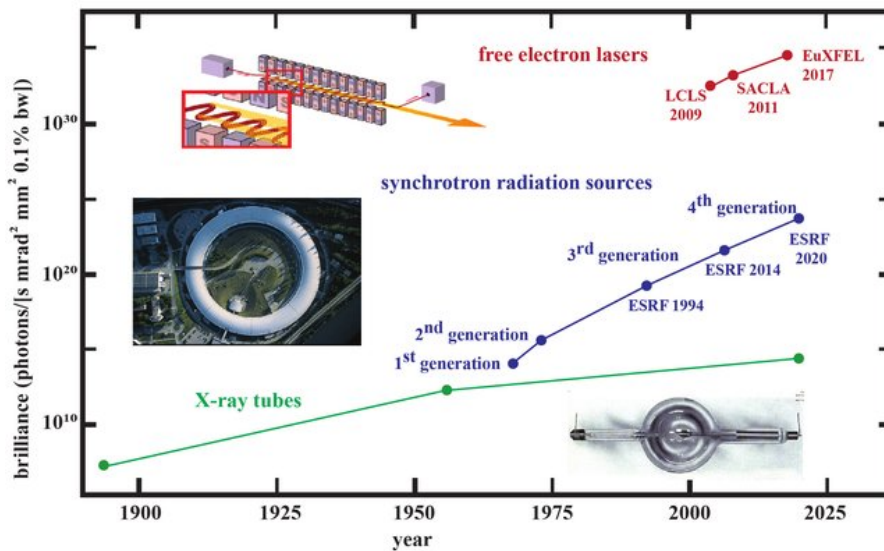
Figure 2.3: Historical evolution of X-ray brilliance over time and development of new X-ray sources. FELs values are given for the peak brilliance, during one pulse [14].

All XFEL experiments of this project so far were performed at the Materials Imaging and Dynamics (MID) instrument at European X-ray Free-Electron Laser (EuXFEL). At EuXFEL, a 1.7 km long superconducting accelerator provides electrons that have up to 17.5 GeV energy. The cryogenic cooling that enables niobium accelerator resonant cavities superconductivity allows to generate upto 2700 pulses in a train every 0.1 s despite the heating of the accelerator. Inside each train the pulses distributed at a frequency of up to 4.5 MHz. The electrons from Cs_2Te photo-

cathode are accelerated in superconducting Niobium cavities. To provide the high-quality SASE emission, this facility is equipped with 175 m long undulators for generation of hard X-rays.

The electron beam is distributed between three different undulators, that produce X-rays with different properties for three photon tunnels, each of which is equipped with two end-stations. Among these the MID instrument offers to study condensed matter physics with hard X-rays (7 – 18 keV). There are a number of important components located before the sample, which allow one to change the X-ray beam properties in accordance with the requirements of the experiment. One of them is the compound refractive lens unit (CRL). There are two such units in the tunnel, which main purposes are to collimate and focus the X-ray beam and together they give the possibility of reaching beam cross sections of 1-2 μm. Another crucial parameter is the beam intensity, which can be adjusted with two attenuator units. These devices contain six different filters of varying thicknesses made of Si, B_4C, and CVD diamond, which are cooled with water and equipped with temperature sensors. In addition, some experiments require to reduce the intrinsic bandwidth ($\sim 10^{-3}$) of SASE radiation, which is possible by two X-ray monochromator devices using Si(111) and Si(220) reflections. The monochromator has not yet been used in this project, but is planned for the next stages. Information about the development of the monochromator at MID instrument can be found in the article [15]. At the end of the instrument there is a diagnostic end-station (DES) equipped with a spectrometer, intensity detector, and an imaging unit. In this project it is used not only for the overall alignment of the beam and sample, but also for synchronisation of the magnetic field pump with the X-ray beam using a diamond-based intensity detector [16], which allows single pulse intensity measurements up to 4.5 MHz repetition rate. The synchronisation process is described in details in Chapter 3.
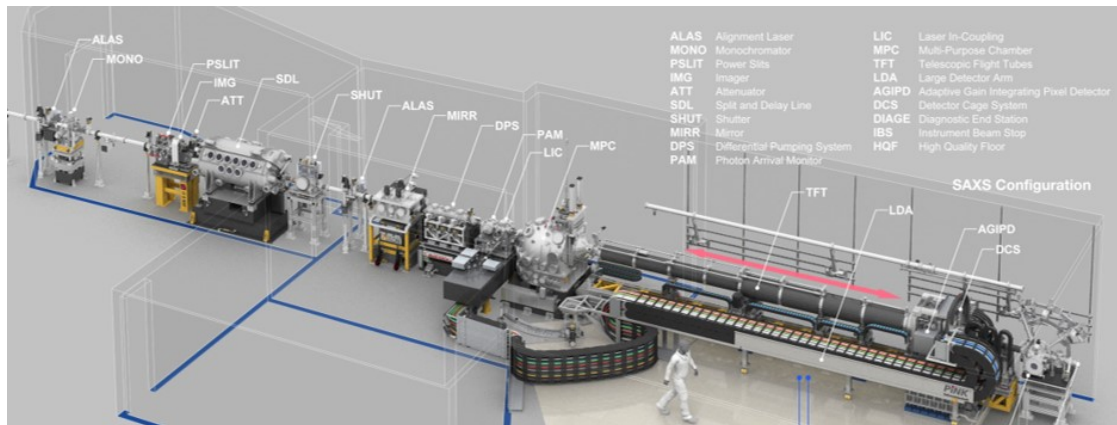
Figure 2.4: 3D CAD-models of MID's optics and experiment hutches and the components in SAXS geometry [12].

The main detector used for this project is AGIPD, which has 10^6 pixels each with a size of

200 μm x 200 μm and is able to resolve single pulses arriving at 4.5 MHz rate and storing up to 352 pulses from one pulse train. Using this detector MID offers three main scattering geometries: Small Angle X-ray Scattering (SAXS), Wide Angle X-ray Scattering (WAXS), and large field-of-view (LFOV). The horizontal detector movement is in the range of 2θ = 15 - 50°, which plays a crucial role in the design of our experiments. Detailed information about the MID instrumentation located in the tunnel, the optical hutch, and the experimental hutch one can be found in Ref [12].

3 Setup description

In addition to the standard configuration MID offers special sample environments, which are installed in the Multi Purpose Chamber (MPC) for specially designed experiment as a part of the preparation before beamtime starts. Hence, a pulsed high magnetic field and low temperatures setup was developed and commissioned as a significant part of this project. The PUlsed MAgnet setup (PUMA) can be split into three parts: magnetic field sample environment, cryogenic temperature sample, sample manipulation system.

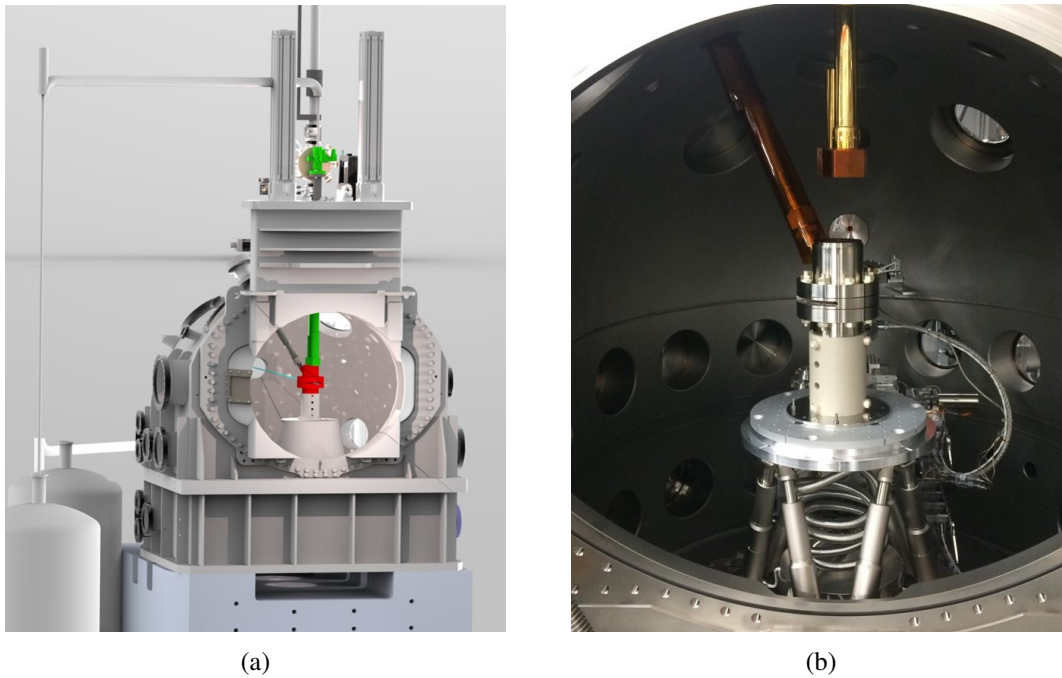(a)   (b)

Figure 3.1: (a) Multi Purpose Chamber (MPC) at MID instrument with two main components of the PUMA: cryostat in green and split-pair coil in red (b) Photo of the PUMA setup inside the MPC.

3.1 Magnetic field sample environment

Superconducting magnets have previously been used at synchrotron and XFEL facilities [17] they are, however, rather bulky for a non-permanent installation. Over the last few years the use of pulsed magnetic field at X-ray sources has grown, another approach, to manufacture miniature magnetic coils with the sample cooled in a helium exchange gas [11, 18, 19]. Based on this approach, for the MID instrument a concept of split-pair magnet coils with horizontal slit-opening was chosen, thus a X-ray detection path from transmission (forward scattering) up to 50 degrees scattering angle (2θ) is kept free of obstacles. One of the major constraints for both synchrotron and FEL experiments is the limited amount of time available. In our case it requires the optimisation of the duty cycle, which is defined as the ratio between duration of the pulse and waiting time between pulses. The former depends on the coil design and the supply. The latter is determined by all the software and hardware delays and the power supply charging time, which is dominating for low field pulses, as well as the coil cool down time, which is dominating for very high field pulses.

The choice of coil wire (material and size) and coil dimensions (bore, outside diameter and length) determine the number of windings and thus the coil resistance and inductance. The material properties such as tensile strength, electrical resistance, and heat capacity in turn define the limits for the maximum reachable magnetic field and the coil heating during a pulse. In addition, the choice of the power supply capacitor and its charge voltage yields the maximum current and pulse length, and thus the magnetic field and induced magnetic forces. Taking all this into account, suitable design choices must be made to find convenient values corresponding to the physical limits and that yield the desirable setup parameters.

One critical design choice for the PUMA setup was to separate the coil cooling from the sample cooling. This allows the sample cryostat and magnet system to be separated, which adds flexibility to the experimental design. In addition, for the magnet design it will minimize the time between pulses using direct cooling of the coil by liquid nitrogen (LN_2). On the other hand, this requires a larger coil bore to isolate with vacuum two cryogenic volumes, and hence increases the energy, needed to reach a given magnetic field (proportional to the third power of the bore size [20, 21]). To fulfill these requirements a stainless steel vessel for the coil was designed around a central bobbin that holds the windings. For the top and bottom lids, CF63 flanges were used to join the parts to ensure that they were vacuum-tight. The top lid of the vessel is connected to the central magnet bobbin using a CF25 seal with a central bore of 10 mm in inner diameter for sample insertion (a sample holder has a diameter of 6 mm). A bellows part between the flange and bobbin prevents tension on the flange, which could cause a vacuum leak at low temperatures (Figure 3.2). As mentioned above, it was crucial to preserve the wide-

<center>(a)   (b)</center>
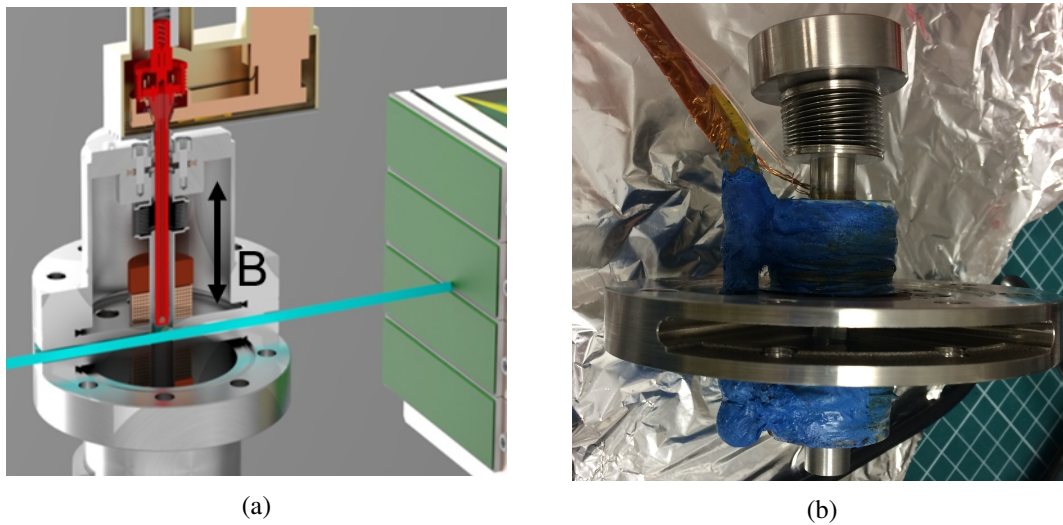
Figure 3.2: (a) Split-pair magnet coil vessel with sample holder (red) insert in the magnet. The X-rays (blue) are going through the central bobbin horizontal slit-opening. The top and bottom lids have a vacuum tight connection to the central bobbin (where blue X-ray beam is going through) and during operation is filled with LN_2. (b) Photo of the split-pair magnet coil with temperature sensor and pick-up coil. The blue part is Stycast 2850 blue epoxy, which forms a solid block between Polyether ether ketone (PEEK) flanges (not visible because of Stycast) and the central steel flange (metal tube in the center).

Figure 3.3: The scheme for X-ray path in scattering geometry. The view inside the central bobbin with has 90 deg horizontal opening (two white sectors of the circle) symmetrical for X-ray entrance (X-ray in) and exit (X-ray out).

angle range of the direct and scattered beam, for this slit with 90 degree horizontal and 8 mm vertical openings were machined into the central bobbin part (in the gap between two p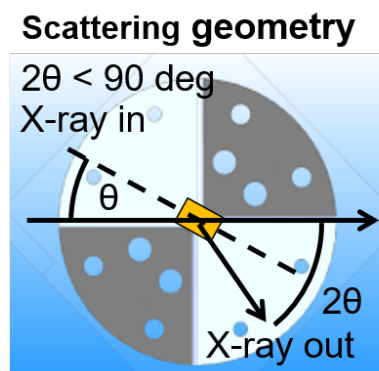arts of magnet pair). These openings are arranged symmetrically to provide entry and exit of X-ray, as shown in the figure 3.3. Finally, VCR-connector was attached to the top lid as a feed through for liquid nitrogen, the power-supply cable, coil temperature and magnetic field sensors. The current design solution allows only geometry, where X-ray access perpendicular to the magnetic field and scattering detection is possible only in the horizontal plane due to a small angular vertical opening. Hence, the momentum transfer is always perpendicular to the applied magnetic field.

The split-pair coil was designed using the PMDS software from K.U. Leuven [21, 22] in order to achieve 15 T maximum magnetic field and a pulse duration of 1 ms. Based on previous work [10], hard drawn copper with a 0.08% silver addition (CuAg) was chosen as wire material to avoid annealing, which reduces the ultimate tensile strength and pure copper shows it at around 200 °C. Usually, the strength of this kind of wire permits reaching magnetic fields on the order of 40 T. Using 1.4 mm^2 hardened CuAg wire with a square cross-section and 50 μm kapton-foil wound insulation we designed a coil with 50 μH inductance. Each half of the coil consists of 6 layers with 9 windings per layer and having a bore diameter of 12 mm and coil pair separation of 8 mm. Each CuAg layer was reinforced by 0.2 mm thick layer of wound Zylon fiber. Using the PMDS software it was determined that at maximum field the combination of CuAg wire plus Zylon fiber experienced a stress below 1 GPa in the Zylon and below 400 MPa in the CuAg, thus keeping both materials below the if respective yield strengths. While increasing the Zylon thickness would reduce the stress and increase from coil life-time, it is known from similar coils [10] that this amount of reinforcement achieves a few 1000 pulses suitable for an FEL beamtime. But on the other hand it also increases the time duration of the coil duty cycle (charge-discharge-cooling to the safe temperature) up to about one pulse every 10-30 sec (depending on the strength of magnetic field). In this way both coil halves were wounded around the central coil bobbin and connected in series. The technique developed in [10] was modified with the use of Stycast 2850 blue epoxy to form a solid block between Polyether ether ketone (PEEK) flanges and the central steel flange (figure). Kapton film was used to further isolate the coil winding from the metal bobbin. During the last construction steps a custom-made coaxial cable for connection to the power supply is soldered to the terminals of the magnet coil. In order to monitor the magnetic field induction a single-turn pick-up coil was wound around the steel bore next to the PEEK flange. In addition into this flange was inserted a Pt100 sensor to monitor the coil temperature during operation and it is fed through the VCR-connector along with the first two connectors (Figure 3.4).

The Metis CDMM power supply, which has a 1 mF capacitance and can be charged up to 3000 V, satisfies our design requirements. In order to fulfill the safety requirement of the PUMA setup
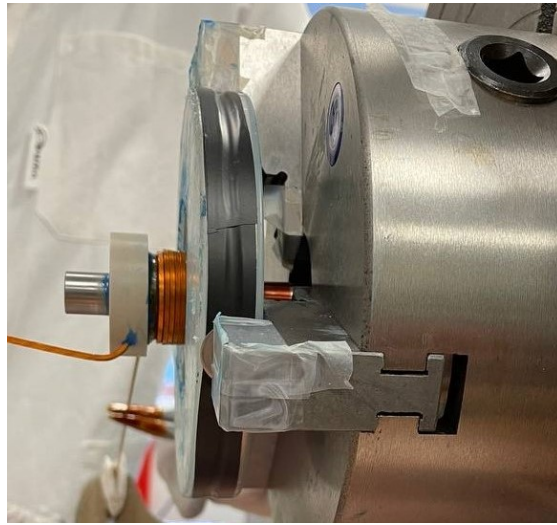
Figure 3.4: The central bobbin fixed in the winding machine, and horizontal opening slit is covered with tape to prevent contamination The five turns of coil wire in the first layer are finished. Above wire there is white PEEK flange with inserted inside Pt100 sensor.

at EuXFEL several modifications were made together with specialists from the Metis company. As it is a single 19 in. cabinet on wheels with a weight of 200 kg, it was possible to place it right above the experimental hutch in a rack room, with a designated fire protected area. Therefore, the length of the high voltage power cables is 15 m.

The coil integration consist of: the chamber mounting, the media feedthrough, safety components and the external media. The stainless steel coil vessel is mounted on the MID in-vacuum hexapod inside the MPC chamber and a DN63CF flange is used to connect a 3/4 flexible metal hose to the media port on the coil vessel. This can be done through two side-mounted DN200CF flanges to avoid a big configuration change with opening of MPC chamber from the detector connection side in case of tight time restrictions. The media feedthrough is the MPC chamber exit for coaxial cable connection to the coil terminal and electrical sensors for coil-temperature and magnetic induction mentioned above (Figure 3.5). In addition in this media feedthrough is located another group of elements, which provides safe and efficient coil cooling: the level-probe to monitor the fluid level of liquid nitrogen inside of the magnet coil vessel, the liquid nitrogen line for continuous refilling the 0.5 L internal capacity, and an exhaust line to safely vent the nitrogen gas that boiled-off during operation. In case of a short-circuit between the CuAg wire and the coil vessel, electrical safety is ensured by a ceramic isolator between the media feedthrough and the main chamber. Safety against ice build-up on the liquid nitrogen connection is ensured by an outer plastic housing that is connected to the nitrogen gas supply.
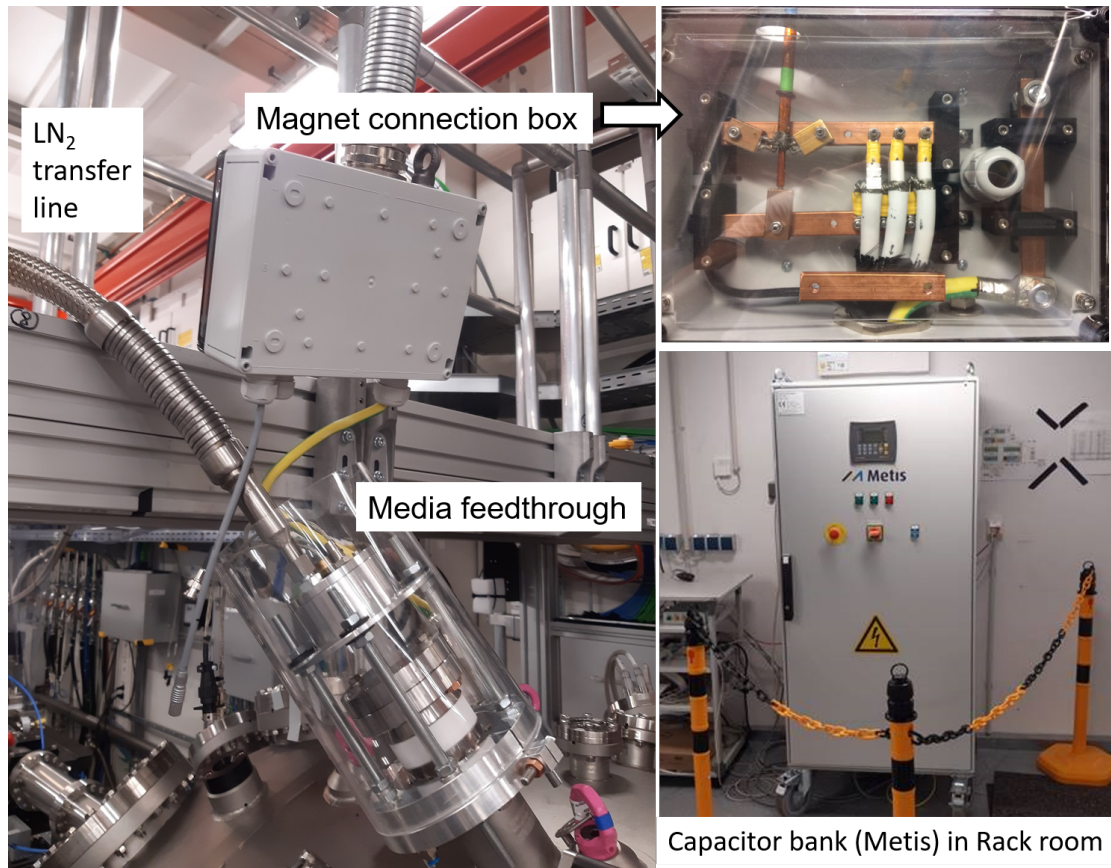
Figure 3.5: The media feedthrough containing: the coaxial cable, the electrical sensors for coil-temperature and magnetic induction, the tube for LN_2 flow, LN_2 level sensor and connection to the "Cryo-LC" level controller, the cable connection to the ground for electrical isolation. On the top right insertion is the view inside of the box with coaxial cable connection to the copper bars and further to the capacitor bank. On the bottom right insertion is the capacitor bank, which is located in the rack room right above the experimental hutch.

Last step of the integration is to connect the media feedthrough to a liquid nitrogen dewar and transfer hose. A type "Cryo-LC" level controller from the company Cryotherm GmbH is connected to the level-probe. The 1 m length home-made coaxial cable from the coil is connected to the Metis CDMM power supply via insulating box, where it is bolted to the copper busbars. The Pt100 and pickup coil sensors are connected to a data-acquisition module via protective relays, which prevents short circuit and are located inside the capacitor cabinet.

It is convenient to test the magnet coil offline in order to check its performance before experiments. In addition it is required to carry out "coil training" during the beamtime before operating in high magnetic fields. Training of the coil magnet involves steadily increasing the maximum magnetic field in small steps with waiting time for the coil temperature drop below 90 K. In this way the stress-level on the CuAg wire is also steadily increased and greatly reduces the risk of a sudden coil-failure. Discontinuities in the magnetic pulse shape often indicate irreversible damage of the coil and allows magnet pulsing to the stopped before a total coil-failure occurs.

3.2 Cryogenic temperature sample environment

The sample cryostat is a dynamic helium flow cryostat from the company Cryovac GmbH. Since the helium continuously passes by the sample this system is very efficient in Synchrotron and FEL experiments, where the sample is illuminated continually or on high-frequency rate. The cryostat is mounted on a manipulator stage, which allows translation/rotation/tilt degrees of freedom and will be described in next section. This type of cryostat is small enough to fit on a DN40CF flange and it also keeps vibrations to a minimum.

The basic working principle of a flow cryostat is that the over pressure produced by the natural evaporation of the liquid helium in the dewar is used to circulate the coolant toward the cryostat via a vacuum insulated line [23]. The coolant is circulating inside the cold-finger (copper heat-exchanger), which directly cools the sample holder. The coolant continues via a second annual heat exchanger, which surrounds the first one and acts as radiation shield. The radiation shield is connected to the first stage of the cryostat at 35 K and shields the sample holder from room temperature radiation. In our cryostat a vacuum roughing pump attached to the exhaust is an alternative way to get coolant through the cryostat. A variable solenoid valve on the pump and a needle valve on the siphon allow us to vary the flow rate depending on the temperature that is needed. The crystat is positioned off-axis and extends 900 mm into the vacuum chamber. The magnetic coil is cooled to 77 K in order to operate it and this additionally acts as radiation shield around the sample holder. The available temperature range is from 8 K up to 300 K, with accuracy of 0.2 K. The helium consumption at base temperature is around 1 L of liquid per hour.
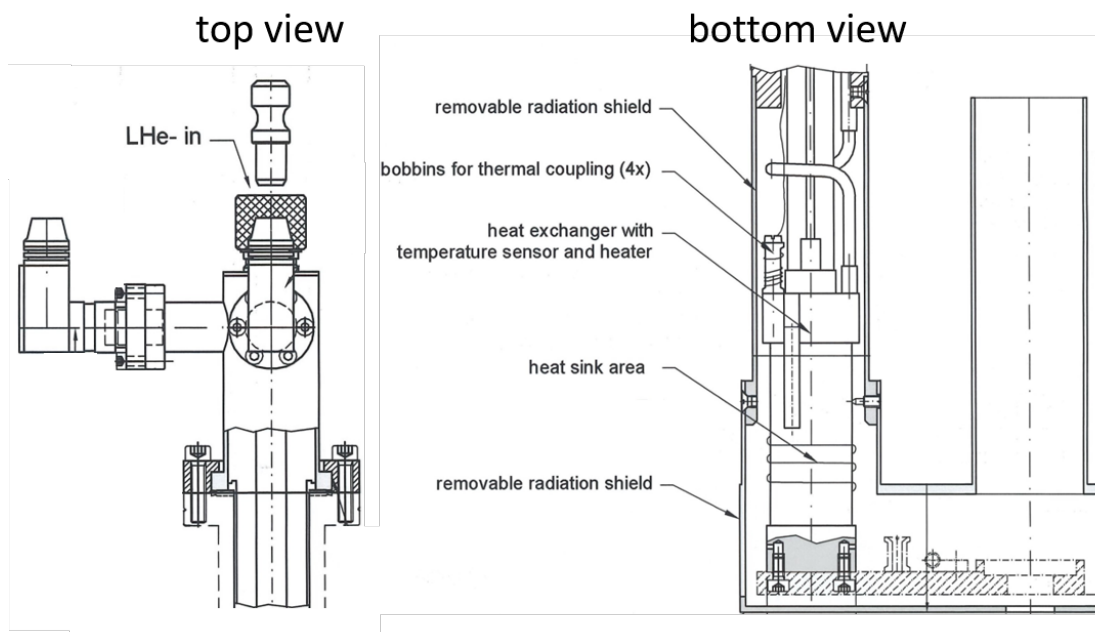
Figure 3.6: Schematic drawing of the continuous-flow helium cryostat.

The optimal cooling rate is 1 - 5 K/min, thus cool down from room temperature to minimum of 8 K is achieved in about an hour.

3.3 Sample manipulation system

The sample holder has two components: the sample stick and the sample cap (Figure 3.8). By changing the sample cap it is possible to change both the geometry of the experiment from scattering to transmission and the sample orientation (e.g inclined sample cap was used for crystal with (111) surface in order to put (001) plane in horizontally reflecting position). Sample holders have a hollow cylinder to enter the magnet bore and contain temperature and electrical contact wires. A Cernox temperature sensor is mounted at the end of the tube under the sample cap. Four wires are provided for making electrical contacts directly to the sample. We use Al_2O_3 for the tube as it is an excellent thermal conductor while being an electrical insulator to avoid the generation of eddy currents. If the magnet is not used we use the copper sample holder, which is easier to manufacture to any desired shape. In addition for easy connect and disconnect of the sample holder from the flow cryostat the connection to the cold-finger is done via an extension "dock" and solid-solid compressed thermal connection (Figure 3.7a). The dock has a cone shaped hole and the sample holder has a matching cone part, both are made of gold-

plated cooper. Alignment pins on the sample-holder help to guide it to the correct rotational position when inserted. Good thermal contract is then supplied by a screwing mechanism. An inner thread on the sample holder can rotate freely with respect to the cone and screws into a matching, but fixed outer thread on the dock. As all eight wires (four temperature wires and four electrical wires) are connected to the pogo-pins on the sample holder, when the sample holder joins with the dock connection is made to an electrical feedthrough on the flow cryostat. The temperature of the sample is regulated by the combination of a 75 W resistive heater attached to cold-finger and the Cernox temperature sensor (Figure 3.7b).

(a)

(b)
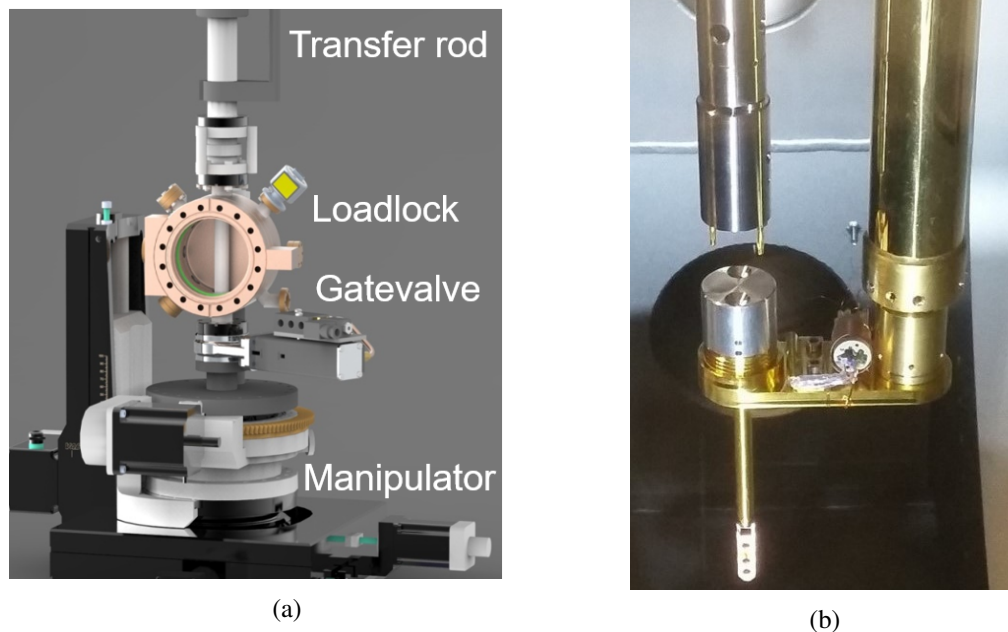
Figure 3.7: (a) Sample exchange and manipulation system consist of: transfer rod, loadlock, gatevalve and manipulator three translational motors X, Y, Z direction and one rotational. (b) The copper sample holder screwed into the cryostat dock and detached from the transfer rode using banana pins.

In order to be efficient, it is necessary to have quick sample-exchange system as well as sufficient degree of both sample and setup manipulation. By using a loadlock for the sample exchange we bypass the need for venting the MPC chamber and warming up the cryostat. This loadlock is mounted on the central axis of the manipulator next to the flow cryostat and separated with a gate-valve from the vacuum volume. The manipulator has four degrees of movements: three translational motors X, Y, Z direction and one rotational θ (Figure 3.7a). A magnetically coupled transfer rod extends directly above the loadlock to be able to transport the sample holder all the way down to the cryostat. The transfer rod has separated motor for vertical sample

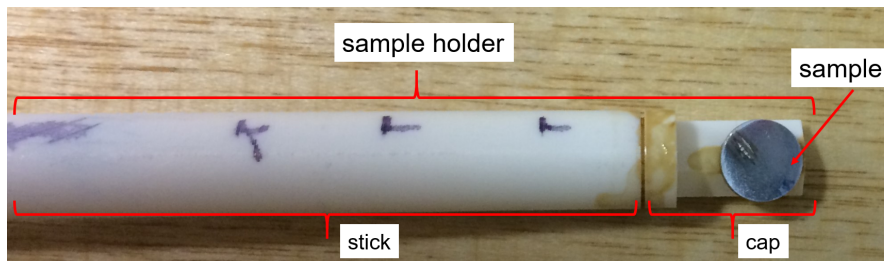Figure 3.8: The Al_2O_3 sample holder, which consist of two components: sample stick and sample cap.

transportation. In total five motors are used for sample holder exchanging, alignment in the magnetic bore and sample manipulation during experiment. The sample holder is then attached to the end of transfer rod in the loadlock and held in place by two banana pins. This design allows to withdraw the transfer rod by disengaging two banana pins as soon as sample holder is transported in the main chamber and screwed in the dock of the cryostat. There are two manual tilt-stages: the first one allows alignment of the transfer mechanism and the cold-finger dock, the second one allows ± 1 deg sample alignment for the vertical direction.

3.4 Software and Synchronisation

While integration of cryo-cooling device and motors into the controls system is straight forward, integration of the Metis capacitor bank and synchronization with the X-ray pulse pattern needs a more detailed explanation. The discharge is synchronized with the X-ray pulse pattern by using Metis' control signals, which requires using the Metis X12A connector's remote control signals (IO-connector 5V logic control). Additionally the control integration depends on the charge-discharge trigger cycle ("pulse-to-charge, pulse-to-trigger" mode) of Metis and the long charge times (1.5 s at 300 V rising to 3.8 s at 3000 V) relatively to the 10 Hz (100 ms) X-ray trains repetition rate. The repetition rate of the system is intrinsically slow and there is no need for a fast signal driven system. When both charge and trigger are driven with the same signal in such systems, it is common to have uncertainty in knowing what the next pulse will do. Thus in order to separate charge and trigger control handling the charge request is delivered via the Ethernet-to-Serial RS232 connector and the trigger is delivered to X12A via either pin 1 (forward field direction) or pin 3 (reversed field direction), where triggers are allowed if pin 2 is high (Figure 3.9).

To start the synchronisation the PUMA software provides a signal, which means that all setup components are ready for discharge, the conditions for this will be described in more detail be-

low. With this "ready" signal the software expects a trigger from the X2 timing board, which is a timing system developed at DESY and synchronised to beam delivery with LVDS (Low-voltage differential signaling) signals. The polarity and length of the trigger signal generated by the External Timing Adapter (ETA) are adjustable. However, the XFEL timing trigger is at 10 Hz while the PUMA "ready" signal is there once in $\sim$ 10-30 sec (coil duty cycle). This logical sum up of signals is done inside the timing system. It receives generated input "ready" signal via ITA (Internal Timing Adapter), which converts signal from (Transistor–transistor logic) levels to LVDS. Finally to receive trigger signal before Metis device this signal goes through an ETA, which converts signal back to TTL (Transistor–transistor logic) levels. The capacitor bank precision trigger upgrade (customization option) allows triggers with lengths of 10 ms (Figure 3.10).
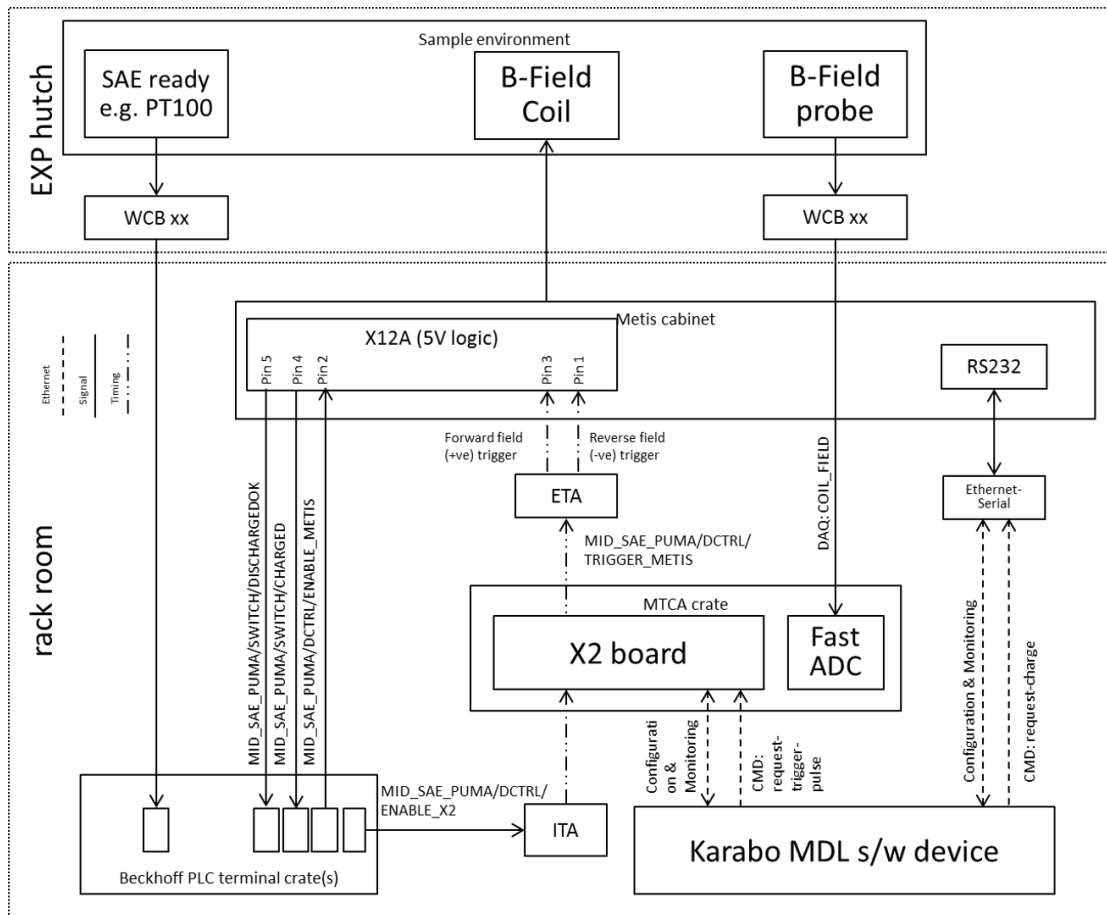

Figure 3.9: The diagram of split-pair coil part of PUMA setup with all elements for synchronization of capacitor bank Metis discharge and X-ray beam of European XFEL.
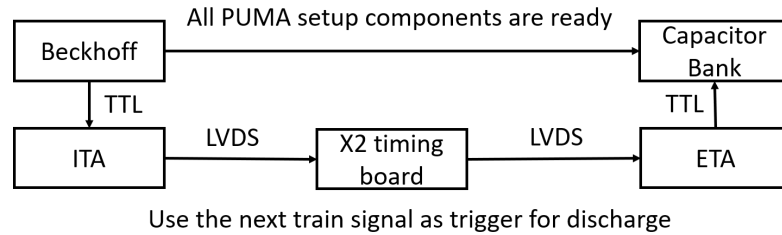
Figure 3.10: The flow diagram of timing synchronisation system components communication.

In the current operation mode only one trigger per discharge is allowed, thus one magnetic pulse contains only one X-ray train with a variable amount of X-ray pulses. To check how the X-ray pulses are overlapping with the magnetic discharge in time an X-ray detector close to the sample position is required. In our case we used a diamond-based intensity detector inside the sample chamber. The output signal was connected to an input channel on the same digital converter (in our case FastADC) which measures the magnetic field from the pick-up coil. The AGIPD detector trigger is precisely timed at the arrival of the X-ray pulse trains. Given this, we set the FastADC to be triggered 0.57 ms prior to the trigger of the AGIPD, and the PUMA to trigger 0.14 ms earlier with duration of 10 ms. The signal appeared on the FastADC approximately 0.1 ms after the triggering of the FastADC, giving an approximate time of 0.24 ms required to begin discharge (Figure 3.11a). Depending on the experimental requirements, different pulse patterns and timing are possible. The magnet can be configured to operate with pulse on demand (this X-ray regime is explained in details later), if X-rays are only desired during magnetic discharge. However, for many applications the X-ray beam is desired before and after the pulse as well. In this case, triggers will be delivered from the X2 timing board at 10Hz, unless disabled by the ITA box. In either case, one or multiple X-ray bunches can be delivered during the train, which can begin at a time specified with respect to the magnetic discharge. The magnet was designed so that magnetic pulse has a total length of approximately 1 ms, of which 0.4 ms is the rising edge and 0.6 ms is the falling edge. The latter coincides in time with the length of one X-ray pulse train with a maximum of 2700 pulses at 4.5 MHz repetition rate (Figure 3.11b,c).

As was mentioned above for synchronisation it is required to have an OK signal from software, showing that the whole setup is ready for a discharge. Karabo is the main software control system used the scientific instruments of European XFEL and those parts of the tunnel beamline and components that transport the X-ray photons. All Karabo applications have standardised interfaces, program-flow organisation, logging and communication. It allows simple integration and adaption to changing control requirements and the addition of new scientific analysis

(a)

(b)

(c)
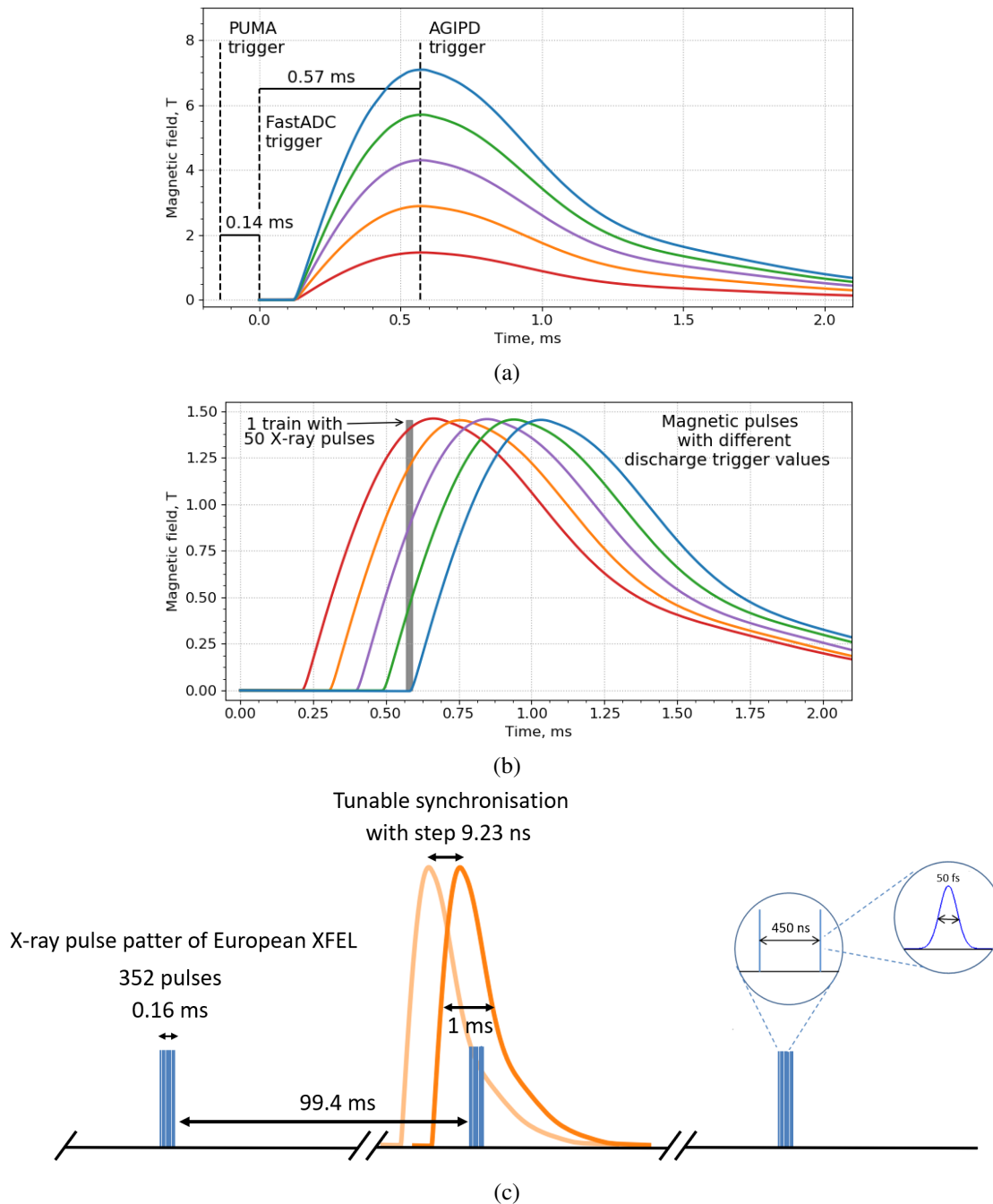
Figure 3.11: (a) The magnetic field time distribution for the split-pair coil. Different colors of the curves corresponds to different value of voltage discharge of the capacitor bank and, accordingly, a different magnetic power. Dotted lines indicate the point in time at which the trigger of different devices occurs: FastADC, PUMA and AGIPD on magnetic curve (b) The magnetic field time distribution for the split-pair coil with the same discharge voltage value. Different colors of the curves corresponds to different value of trigger signal for the capacitor bank discharge. The gray lines indicate the moment of interaction of the sample with the X-ray train, which consist of 50 pulses at 2.2 MHz. (c) The EuXFEL temporal structure for magnetic measurements.

algorithms. Similar to other popular control systems the basic building blocks of Karabo are controllable objects (devices) managed by a device-server. A large set of attributes is available to detail the description of the device properties and commands. Typical attributes for example are: default value, physical unit, displayed label, value-bounds, alarm and warn thresholds, access mode (initially configurable, re-configurable, read-only), etc. User can remotely control devices and device-servers, as well as utilized the self-description (available properties and commands) of each device. It is possible to run all Karabo interfaces using either the command line (CLI) or the graphical (GUI) interface. CLI interpreters based on Interactive Python (IPython) run the device-client, so any interactively given command can as well be written into a regular IPython script and be executed as a macro. Basic layout GUI is formed seven flexible panels: the navigation panel, the project panel, the notification panel, the configuration panel, the central panel (Figure 3.12) [24].

Since motors and sample cryo-cooling control is fairly straightforward, a full explanation of these scenes can be found in the supplementary materials. Here we describe in more detail the scene for magnet control, also explaining the special aspects of its operation:

MDL state reflects the state of capacitor bank state, which has "ON" state, when all the safety requirement are fulfilled and Metis device has been switched on and is in the remote control. The safety requirement consist of two parts: experimental hutch has to be interlocked and internal the Metis device safety switch has to be in deactivated position to disconnect the safety relay, which prevents capacitor bank to be charged.

Discharge Mode allows to choose the discharge trigger type. The manual trigger corresponds to a simple discharge with no synchronisation with the X-ray arrival. The pulse on demand (POD) trigger has synchronisation to the X-ray arrival and includes turning off the X-ray beam for several trains before and after one train, which contains the discharge. The Beckhoff trigger allows to synchronise to the next upcoming X-ray train and provide a discharge without affecting previous or following X-ray trains. All triggers require fulfilling the conditions that the capacitor bank was charged fully and reached voltage setpoint.

Pulse Loop Mode allows two different types of discharges series: equal voltage in a sequence of discharges, or equal steps is a discharge sequence with a uniformly falling or growing voltage.

Pulse Polarity allows two opposite directions of magnetic field perpendicular to the X-ray scattering plane: positive and negative.

Voltage SetPoint allows to set the voltage in a range from 300 V to 3000 V.

Requested Pulses shows the number of discharges requested for the sequence.

Remaining Pulses shows the number of discharges, which are remaining from the requested sequence.

Temperature (plot) shows the coil temperature as a function of time. One of the important built-in software safety measures is to block any charge and discharge if the coil temperature is higher than 90 K. This measure prevents the split-pair coil from early failure. As an additional electrical safety the measure temperature sensor wire is connected to the relay of the Metis device, which disconnects it from the Beckhoff terminals to prevent spread of short circuit. On this plot the moments of charge and discharge are visible as sharp raise of temperature.

Peak Field (plot) keeps the history of peak magnetic field.

Field per Voltage (plot) keeps track of the reproducibility of the magnetic field with the same voltage during continuous discharging.

Voltage (plot) pick-up coil signal. Once the discharge was detected shows measured magnetic pulse curve in volts units within time frame pre-settled in FastADC (channel 0).

Corrected ADC (plot) Noise corrected pick-up coil signal. Once the discharge was detected shows magnetic pulse curve with subtraction of noise level of FastADC.

Integrated ADC (plot) once the discharge was detected shows the integrated corrected magnetic pulse curve normalized on pick up coil coefficient. This calibration coefficient is calculated from the loop area of pick up coil and correction factor, which is taking into account difference between sensor and sample positions. The pick up coil is located above sample position, thus after manufacturing the new split-pair coil the test-pick up loop is temporarily placed on sample position and the correction factor is measured as a difference between two detected magnetic field values. (calibration coefficient $= \mathrm{area}^{-1} \times$ correction factor)

3.5 Challenges and future development

A big part of this project was focused on testing the setup operation in the laboratory, characterization and improvement of the components. During the experiments within this project several of problems were encountered and both hardware and software were developed to overcome them.
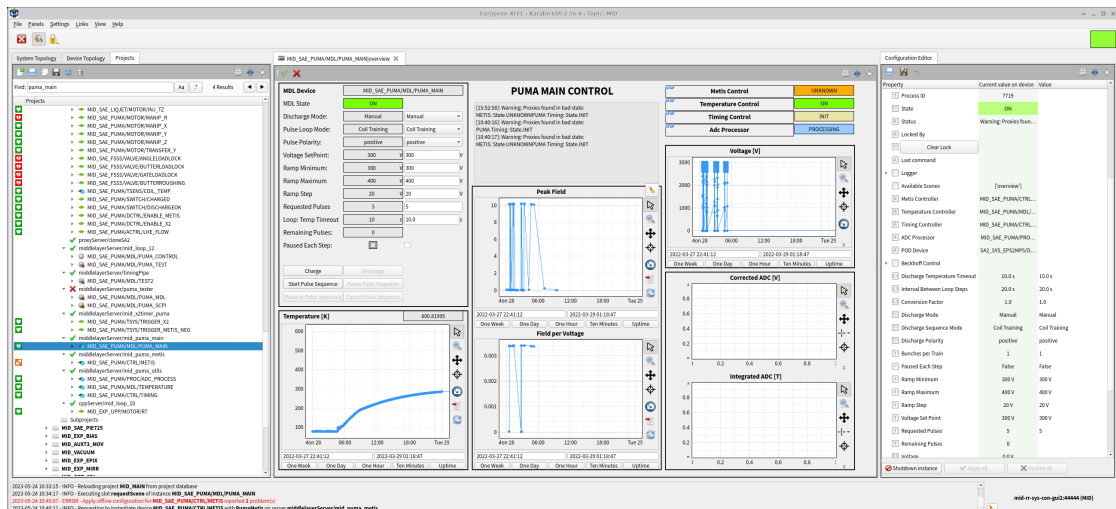
Figure 3.12: The Karabo scene for the PUMA main control system.

As an example of such on the first steps it took some iteration to come up with optimal design of the sample holder connection to the cryostat dock. To achieve and stabilise operation at low temperatures it was important to minimize contact with any heat sources to the sample. In this regard, the transfer rod, which is used to mount the sample in the cryostat, potentially limits the lowest possible achievable temperature. This tests were carried out in the laboratory and presented in Chapter 6. At the same time additional weight pressure on the connection between the sample and the cryostat improves the thermal contact. In the lab, three different approaches were tested: grub screw connection, double thread connection, combination of banana pins and screw. The latter showed both the most reliable mechanical operation and efficient cooling.

Another big issue, which was encountered during the first operations was sample precession. This had several negative consequences for the experiment: a significant increase in the time required to align the sample, increased risk of sample holder running into the magnet vessel and breaking the holder. This also effected the first data, as the rocking curves measured with the PUMA setup at MID had larger FWHM than curves which were measured in advance on the laboratory X-ray diffractometer (The Helmholtz-Zentrum Hereon). The reason for such sample holder behaviour was mechanical force on the cryostat caused by the siphon, which with an arm of 900 mm length result in a significant holder tilt. To solve this problem in the current design of the PUMA setup is implemented a siphon holder, which is attached to the manipulator, and holds the majority of the siphon weight allowings unrestricted sliding during sample rotation.

Overall the PUMA setup has a great potential, thus there are several improvements, which are planned in future. During last operation we ran into a problem of vacuum leak appearing during continuous operation with high magnetic fields. To solve this problem during the experiment

takes a significant amount of time, as it requires warming up the magnet, venting the MPC, tightening the screws on magnet vessel, pumping the chamber and cooling the magnet down. This issue is yet to be further investigated and a solution to be found. In addition, with the improvement of the central bobbin of the magnet in the direction of reducing the amount of the cooper material around the coil and, consequently, the resulting eddy currents, the power of the magnetic field can be increased from 12.5 T at least to originally planned 15 T. Finally, current design allows only the magnetic field perpendicular to the scattering plane, thus one of the next steps is to develop a second coil design to cover experiments with coplanar magnetic field.

4 Theoretical Concepts

4.1 Types of magnetic structures

In regular crystalline structures each atom carries a magnetic moment, associated with a total angular momentum, which is a sum of the orbital angular momentum $\mathbf{L}$ and the spin angular momentum $\mathbf{S}$. The magnetic moment of the atom can be affected by the neighbouring atoms and by an external magnetic field. Here we use the concept of solids in which magnetic ions are localized at lattice sites. In an external magnetic field, the spins tend to align with the field and point roughly in the same direction or the opposite one. In most of the cases the ratio between magnetic moment per volume (magnetisation) and magnetic field is linear: $\mathbf{M} = \chi \mathbf{H}$, from here χ is defined as the magnetic susceptibility. Material with a negative susceptibility is called diamagnetic and material with a positive susceptibility is called paramagnetic. Diamagnetism is the phenomenon of the appearance of a magnetic field opposite to the external one as a result of an induced current. Although diamagnetism appears in all materials, it can be overwhelmed by the much stronger effects caused by the unpaired electrons. One of such dominating behaviours is paramagnetic, which enhances an external magnetic field by orienting the magnetic moment of the unpaired electron in the same direction as the applied field. In paramagnetic state with decrease of an external magnetic field the long-range spin order (correlation, which is maintained over large number of atomic diameters) disappears, thus the magnetisation goes to zero with decrease of the field. If there were no magnetic interaction, the individual magnetic moments in the absence of a field would be disordered at any temperature, and the values of the magnetic moment averaged over all directions would be equal to zero. However, for some solids below the characteristic temperature value (critical temperature), the average magnetic moment of an individual ion does not vanish. Thus in the ferromagnetic state the long-range spin order decreases, but the local interactions among the spins are strong enough to maintain a non-zero net magnetisation even in the absence of an external magnetic field, this is spontaneous magnetisation.

The distinction between paramagnetic and ferromagnetic behaviour was first made by Pierre Currie in 1895 as well as the presence of a temperature dependence in the transition between them. Wilhelm Lenz introduced a theoretical understanding of the phase transition from ferro-

magnetic to paramagnetic in 1920 [25] as the Ising model. The name "Ising model" (sometimes called the Lenz–Ising model, as suggested by Ising himself) was coined in a famous paper by Rudolph Peierls [26] in reference to Ernst Ising's 1925 PhD thesis [27], which was carried out under Lenz's supervision and devoted to the one-dimensional version of the model [28].

The more common case is when the sum of individual local moments is equal to zero, thus spontaneous magnetisation is zero and microscopic level ordering does not lead to the macroscopic magnetisation. This magnetically ordered state is called antiferromagnetism. In the simple cases of ferromagnets, all local moments have the same value and average direction. The simple antiferromagnetic case is, when local magnetic moments form two nested sublattices with the same structure. Thus in each sublattice the average value is the same, but the sum of opposite directions results in zero net magnetisation.

The same classification is applied to metals, despite the lack of a local magnetic ions concept. In this case, the spin density along the chosen z direction , $s_z(\mathbf{r}) = \frac{1}{2}[n_\uparrow(\mathbf{r}) - n_\downarrow(\mathbf{r})]$), which is defined in each point $\mathbf{r}$, describes the ordering in a system. Here $n_\uparrow(\mathbf{r})$ and $n_\downarrow(\mathbf{r})$ denote the contribution of electrons in the corresponding spin states to the total electron density (the projections of the spin on the z-axis). In ferromagnetic metals, both the local spin density and integral along some axis are non-zero, while for antiferromagnets the integral is equal to zero along all directions, but the spin density is non-zero. Complex magnetic structures can also be observed in metals: Chromium is an antiferromagnet characterized by a periodic distribution of the spin density, which under normal conditions is not related to the lattice period but is determined by the geometry of the Fermi surface. The rare-earth metal Dysprosium has a helical antiferromagnetic ordering between 85 K and 180 K in absence of an external magnetic field. Both of these cases are described in more detail below.

4.2 Heisenberg model

Various forms of magnetic interaction contribute to the exchange of magnetic moments within solids and the establishment of long-range order.Therefore, it is logical to commence the discussion with an introduction to the magnetic dipolar interaction. Two magnetic dipoles μ_1 and μ_2 at a distance $\mathbf{r}$ energy:

$$E = \frac{\mu_0}{4\pi r^3}\left[\mu_1 \cdot \mu_2 - \frac{3}{r^2}(\mu_1 \cdot \mathbf{r})(\mu_2 \cdot \mathbf{r})\right] \tag{4.1}$$

, here μ_0 is the the magnetic permeability in a vacuum. It is easy to estimate the order of magnitude for this effect: magnetic dipole moment of atom $\mu_1 \approx \mu_1 \approx g\mu_B$, where the Bohr magneton is $\mu_B \approx \frac{e\hbar}{2m_e}$ and g-factor $g \approx 2$ and the common distance in solid magnetic is $r \approx 1 - 2$

Å. Thus, the interaction energy does not exceed 10^{-4} eV, which corresponds to about 1 K in temperature.

The other type of interaction, which is responsible for the long-range magnetic order is exchange interaction. It is connected to electrostatic interaction of charges with the same sign, which cost energy when they are close together and save energy when they are apart. Due to the Pauli principle magnetic effect is appearing even, when the Hamiltonian does not depend on the spin. Considering a simple model with just two electrons which have spacial coordinated $\mathbf{r_1}$ and $\mathbf{r_2}$ respectively and wave function $\psi(\mathbf{r_1r_2})$ obeys the Schrödinger equation with the following Hamiltonian:

$$\hat{H}(\mathbf{r_1},\mathbf{r_2}) = \frac{\mathbf{p_1}^2}{2m_e} + \frac{\mathbf{p_2}^2}{2m_e} - \frac{2e^2}{4\pi\varepsilon_0|\mathbf{r_1}|} - \frac{2e^2}{4\pi\varepsilon_0|\mathbf{r_2}|} + \frac{e^2}{4\pi\varepsilon_0|\mathbf{r_2}-\mathbf{r_1}|} \tag{4.2}$$

here $\mathbf{p}$ is electron momentum, m_e is electron mass, ε_0 is dielectric constant of the vacuum. In the ground state the spatial part of the total wave function is symmetric because both electrons are in the same orbital. Therefore due to the Pauli exclusion principle the spin part has to be asymmetric:

$$\psi_{\text{gs}}(\mathbf{r_1s_1};\mathbf{r_2s_2}) = \psi_{\text{sym}}(\mathbf{r_1},\mathbf{r_2})\chi_{\text{as}}(\mathbf{s_1},\mathbf{s_2}) \tag{4.3}$$

The actual calculation of ground state energy can be found here [29]. This requirement of an asymmetric total wave function is crucial in case of excited states, which correspond to the rwo electrons occupying different orbitals and there is an energy splitting. The combination of two electrons $s = \frac{1}{2}$ results: in singlet state with spin quantum number $S = 0$ and the component of the spin along a specified axis $M_S = 0$, where the spin function is asymmetric; and triplet state with $S = 1$ and $M_S = -1, 0, 1$, where the spin function is symmetric [30].

The difference between energies of singlet and triplet states, can be described using algebra based on defining the total spin angular momentum operator $\hat{\mathbf{S}}$ through Pauli spin matrices:

$$\hat{\mathbf{S}} = \begin{pmatrix} S_x \\ S_y \\ S_z \end{pmatrix} \tag{4.4}$$

$$\hat{S}_x = \frac{1}{2}\begin{pmatrix} 0 & 1 \\ 1 & 0 \end{pmatrix} \qquad \hat{S}_y = \frac{1}{2}\begin{pmatrix} 0 & -i \\ i & 0 \end{pmatrix} \qquad \hat{S}_z = \frac{1}{2}\begin{pmatrix} 1 & 0 \\ 0 & -1 \end{pmatrix} \tag{4.5}$$

Here we omit the detailed explanation of singlet and triplet states nature and calculations of the eigenvalues, but these details can be found in several books, for example [31].

To build the two electron system Hamiltonian, it is required that each electron

operator satisfies the equation $\hat{\mathbf{S}}_i^2 = \frac{1}{2}(\frac{1}{2}+1) = \frac{3}{4}$, thus for full spin $\hat{\mathbf{S}}$ expression: $\hat{\mathbf{S}}^2 = (\hat{\mathbf{S}}_1 + \hat{\mathbf{S}}_2)^2 = \frac{3}{2} + 2\hat{\mathbf{S}}_1\hat{\mathbf{S}}_2$. Since the eigenvalue is $S(S+1)$ for the operator $\hat{\mathbf{S}}^2$ with spin states S, for operator $\hat{\mathbf{S}}_1\hat{\mathbf{S}}_2$ eigenvalue is $-\frac{3}{4}$ in singlet state (S = 0) and $+\frac{1}{4}$ for triplet state (S = 1). Thus, the desired spin Hamiltonian is [31]:

$$\hat{H}^{\text{spin}} = \frac{1}{4}(E_s + 3E_t) - (E_s - E_t)\hat{\mathbf{S}}_1\hat{\mathbf{S}}_2 \tag{4.6}$$

Here, the eigenvalue E_s corresponds to the singlet state and E_t to each of the triplet states. The energy reference point can be shifted by omitting the constant, which is the same for all states:

$$\hat{H}^{\text{spin}} = -J\hat{\mathbf{S}}_1\hat{\mathbf{S}}_2 \text{ , where } J = E_s - E_t \tag{4.7}$$

For a system with more than two ions located at a large distance from each other, it is possible to construct an operator function depending on $\hat{\mathbf{S}}_i$:

$$H^{\text{spin}} = -\sum_{ij} J_{ij}\hat{\mathbf{S}}_i\hat{\mathbf{S}}_j \tag{4.8}$$

This spin Hamiltonian is called the nearest neighbour Heisenberg model, where J_{ij} is the constant of exchange interaction and the $\langle ij \rangle$ summation goes over the nearest neighbors. This model might also apply to the total angular momenta $\mathbf{J}_i$ in the case of rare-earth ions.

Since spins are treated as three-dimensional vector in a lattice, it is important to distinguish between dimensionality d of the lattice and dimensionality D of the spins themselves. For Heisenberg model D = 3, however, a lattice of these spins can be considered in 1,2, and 3 dimensions. In this regard, an important limiting case is obtained when the exchange interaction is anisotropic, and the interaction between z components (or equivalently x and y) is much stronger than all others. A related model is the Ising model in which the spins are only allowed to point up or down, and thus the order parameter D is equal to 1:

$$\hat{H}^{\text{spin}} = -\sum_{ij} J_{ij}\hat{\mathbf{S}}_i^z\hat{\mathbf{S}}_j^z \tag{4.9}$$

4.3 Phase transitions

To describe the temperature dependence of the magnetic structure in solids, it is necessary to determine the configuration of the moments, which minimises the free energy, taking into account the influence of increasing temperature and magnetic disorder on the interaction. Deriving from the foundational principle of the first law of thermodynamics concerning a closed thermodynamic system, the internal energy is recognized as a state function. Its alteration during any

thermodynamic process can be quantified as the cumulative effect of heat transferred into the system, mechanical work exerted upon the system, and other potential modes of energy exchange (if they exist). The free energy is a thermodynamic potential that measures the useful work obtained from the closed thermodynamic system at a constant temperature. This free energy is connected to the entropy (for more details [32]), which is the measure of the disorder of a thermodynamic system, thus the increase in entropy means that system became more disordered. Within mean-field theory (which is described in the next section), the entropy is the same for the same relative ordered magnetic moment **M**, so the stable structure has a minimum energy [33]. In the systems with dominated exchange interaction, the ordered magnetic moment approaches a saturation value at low temperature [34]. As the temperature increases, because of renormalisation of the effective interactions, the minimum energy structure may change. This change can occur in two ways: as a first-order transition characterized by discontinues change of some order-parameter, or as a second-order transition, in which the order-parameter goes continuously to zero. At elevated temperatures, the entropy may favour a structure, such as the longitudinal wave, in which the degree of order varies from site to site. A conceptually simple but powerful means of calculating magnetic properties and their temperature dependence is provided by the molecular field approach, or mean field theory [33].

4.4 Mean-field theory of magnetic ordering

The earliest approach for the quantitative description of ferromagnetic transition was suggested by Weiss so called molecular field approximation or mean-field theory. This is the simplest model that can be constructed to describe different types of phase transition and is often taken as a starting point for more complex calculations. For a ferromagnet in an applied magnetic field **B** the Hamiltonian to solve is:

$$H = -\sum_{ij} J_{ij} \hat{\mathbf{S}}_{\mathbf{i}} \hat{\mathbf{S}}_{\mathbf{j}} + g\mu_B \sum_{j} \hat{\mathbf{S}}_{\mathbf{j}} \mathbf{B} \tag{4.10}$$

The exchange constants for nearest neighbours are positive for such ferromagnetic alignment. The first term in this sum is the Heisenberg exchange energy, and the second term is the Zeeman energy. In this case, molecular field at the ith site is given by:

$$\hat{\mathbf{B}}_{mf} = -\frac{2}{g\mu_B} \sum_{j} J_{ij} \hat{\mathbf{S}}_{\mathbf{j}} \tag{4.11}$$

The ith spin energy is sum of Zeeman part and an exchange part, thus total exchange interaction between the ith spin and its neighbours can be written as:

$$-2\hat{\mathbf{S}}_{\mathbf{i}} \sum_{j} J_{ij} \hat{\mathbf{S}}_{\mathbf{j}} = -g\mu_B \hat{\mathbf{S}}_{\mathbf{i}} \hat{\mathbf{B}}_{mf} \tag{4.12}$$

Hence the exchange interaction is replaced by an effective molecular field produced by the neighboring spins and the effective Hamiltonian now looks like the Hamiltonian for a paramagnet in a magnetic field $\mathbf{B} + \hat{\mathbf{B}}_{mf}$

$$\hat{H} = g\mu_B \sum_{j} \hat{\mathbf{S}}_{\mathbf{i}} (\mathbf{B} + \hat{\mathbf{B}}_{mf}) \tag{4.13}$$

The assumption behind this approach is that all magnetic ions experience the same molecular field. For a ferromagnet, the molecular field influences the alignment of neighbouring magnetic moments. The strength of the molecular field is proportional to the magnetisation $\hat{\mathbf{B}}_{mf} = \lambda \mathbf{M}$, where λ is a strength of molecular field:

$$\lambda = \frac{V}{N} \frac{J_0}{(g\mu_B)^2} \text{ , where } J_0 = \sum_{R} \mathbf{J}(\mathbf{R}) \tag{4.14}$$

Thus, the expression for magnetisation using mean-field theory is:

$$M = M_0 \left(\frac{\mathbf{B} + \hat{\mathbf{B}}_{\mathbf{mf}}}{T} \right) \tag{4.15}$$

where M_0 magnetisation in a magnetic field B with temperature T in the absence of magnetic interaction. Spontaneous magnetisation $M(T)$ at temperature T is defined as a non-zero solution of the equation in the absence of an external field B = 0:

$$M(T) = M_0 \left(\frac{\lambda M}{T} \right) \tag{4.16}$$

The easiest way to find the solution for this equation is graphically by representing it as system of two equations:

$$M(T) = M_0(x), \qquad M(T) = \frac{T}{\lambda} x \tag{4.17}$$

Solutions exist at the points where the function $M_0(x)$ overlaps with the plot $\frac{T}{\lambda}x$. They overlap in a non-zero x value only when the lateral incline exceeds the incline of $M_0(x)$ at the origin of the coordinate system. The first derivative of $M_0(x)$ is equal to magnetic susceptibility in zero field in the absence of interaction and can be compared with the explicit expression for the Curie law:

$$\chi = \frac{N}{V} \frac{(g\mu_B)^2}{3} \frac{S(S+1)}{k_B T} \tag{4.18}$$

Thus the critical temperature is determined:

$$T_c = \frac{N}{V} \frac{(g\mu_B)^2}{3k_B} S(S+1)\lambda = \frac{S(S+1)}{3k_B} J_0 \tag{4.19}$$

The critical temperature, below which material becomes ferromagnetic, is named the Curie temperature and for antiferromagnetic phase is named the Néel temperature. However, mean-field theories fail to accurately describe critical region close to magnetic phase transition temperatures, do not predict the existence of spin waves at low temperatures, and at high temperatures reproduce only the fundamental correction for the Curie laws. The values obtained using mean field theory almost exceed the exact values by a factor of two; this disagreement improves with increasing lattice dimension and coordination number. The expression for susceptibility in this theory is found by differentiating:

$$\chi = \frac{\partial M}{\partial H} = \chi_0(1 + \lambda\chi) \tag{4.20}$$

$$\chi = \frac{\chi_0}{1 - \lambda\chi_0} = \frac{\chi_0}{1 - (T_c/T)} \tag{4.21}$$

Here χ_0 is the susceptibility in the molecular field B_{mf}. This relation is called the Curie-Weiss law. Although near T_c the measured and calculated susceptibilities of a three-dimensional ferromagnet diverge. This law shows that the high-temperature correction increases the susceptibility value of a ferromagnet compared to that given by the Curie law.

Adding the external magnetic field results in a solution with non-zero magnetisation $M \neq 0$ for all temperatures, and thus the point of phase transition is moved. For ferromagnets, it is energetically profitable to have nonzero magnetisation with magnetic moments aligned in the direction of the magnetic field. In this model it is not necessary to consider the direction of the magnetic field, because the magnetisation will always rotate round to follow this direction. However, in a real ferromagnet crystals the effect of magnetic anisotropy needs to be considered. At $T = T_c$ the effect of a magnetic field can be analytically evaluated, such as magnetisation $M \sim B^{\frac{1}{3}}$ for small magnetic fields. Finally, to evaluate the effect of a strong magnetic field on antiferromagnets, one should consider $T = 0$ avoiding complications caused by thermal fluctuations. If an external magnetic field is strong enough, it must eventually overcome the molecular field and force all magnetic moments to align parallel. However, the route to this result depends on the direction of the applied magnetic field relative to the sublattice magnetisation. If the magnetic
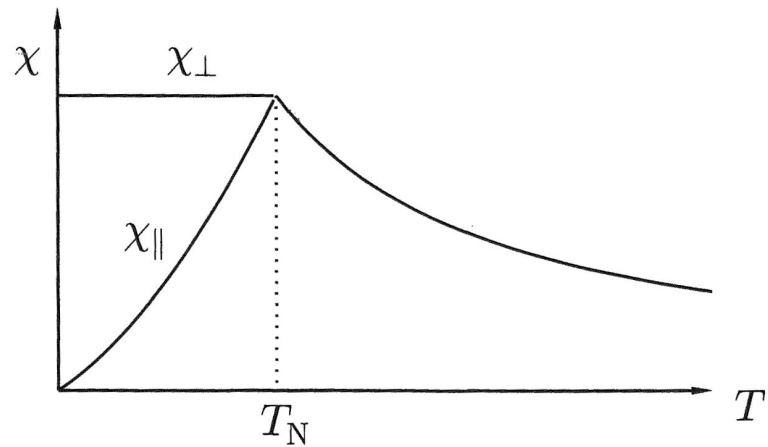
Figure 4.1: The effect of temperature on the magnetic susceptibility. In case of magnetic field applied perpendicular to the sublattice magnetisation $\chi_\perp$ and parallel to the sublattice magnetisation $\chi_\parallel$ [35].
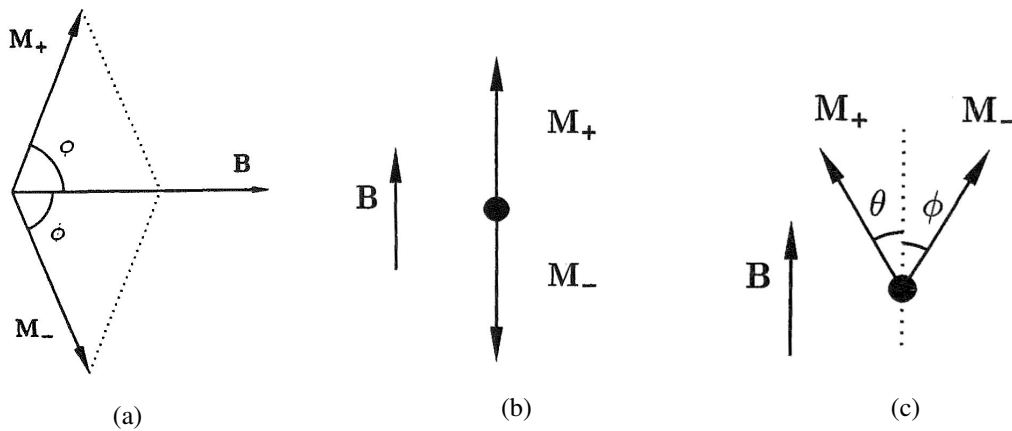

Figure 4.2: (a) A small magnetic field B, applied perpendicular to the magnetisation direction of the sublattices, causes the tilt of these directions so that there is a magnetisation component along the applied magnetic field. (b) A small magnetic field B, applied parallel to the sublattices magnetisation, has no effect on antiferromagnetic phase. (c) A magnetic field stronger than critical value, applied parallel to the sublattices magnetisation, causes a spin-flop transition, magnetisation rotation [35].

field is perpendicular to the sublattice magnetisation, the field bends the magnetic moments so that the angle between these vectors decreases until moments line up with the field direction. More complicated mechanism is appearing in case when the magnetic field is parallel to the sublattice magnetisation. If the strength of applied field exceeds the critical value the system undergoes sudden change of configuration, which is called a spin-flop transition. With further increase of magnetic field, the magnetic moments will eventually line up with its' direction [35]. To evaluate this effect quantitatively, it is necessary to define: the angle of two sublattice magnetisations $\mathbf{M}_+$ measured counterclockwise θ and $\mathbf{M}_-$ measured clockwise ϕ. Thus, the antiferromagnetic phase corresponds to $\theta = 0$ and $\phi = \pi$ and the spin-flop phase corresponds to $\theta = \phi$. It is necessary to determine which phase has lower energy. The total energy E is the sum of the Zeeman energies of the individual sublattices and a term for exchange coupling, which depends on their relative orientation. Also, to consider the effect of magnetic anisotropy, a term of the form is added. This term accounts for the fact that the magnetisation prefers to lie in a certain crystallographic direction ($\theta = 0$ and $\phi = \pi$ and not somewhere inbetween):

$$E = -MB\cos\theta - MB\cos\phi + AM^2\cos(\theta + \phi) - \frac{1}{2}\Delta(\cos^2\theta + \cos^2\phi) \qquad (4.22)$$

Here A is a constant connected with the exchange coupling and Δ is a small constant.

For antiferromagnetic phase (independent of field): $\qquad E = -AM^2 - \Delta \qquad (4.23)$

For spin-flop phase: $\qquad E = -2MB\cos\theta + AM^2\cos 2\theta - \Delta(\cos^2\theta) \qquad (4.24)$

The first derivative for spin-flip phase shows minimum energy, when $\theta = \cos^{-1}[B/2AM]$, ignoring the anisotropy term. The result leads to the graph on Figure 4.3.

   The magnetisation of antiferromagnets in a large parallel magnetic field is shown in Figure 4.4a. There is no effect until the spin-flop transition, above which the magnetisation increases steadily until saturation. However, if the anisotropy effect is strong (Δ is large), another effect can occur instead, which is called spin-flip. In this case, when the critical field is reached, the magnetisation of the sublattices suddenly reverses in a single step (Figure 4.4b).

4.5 Helical order and Magnetostriction

Since one of the materials studied in this project is rare-earth dysprosium (Dy), it is necessary to focus on one more type of magnetic ordering. For many rare-earth metals (relevant for dysprosium) the alignment of atomic moments within the plane is ferromagnetic. Consider that the
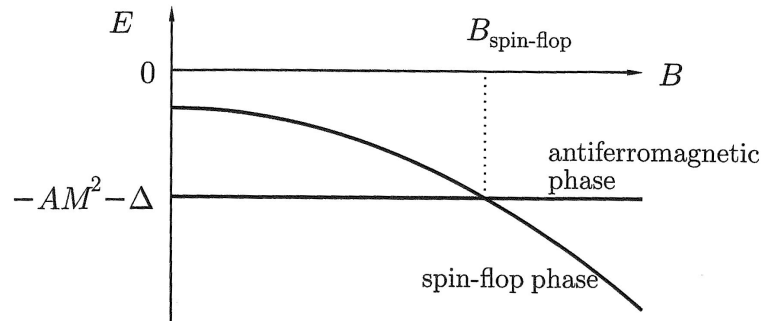
Figure 4.3: The energy of the antiferromagnetic phase and the spin-flop phase as a function of magnetic field B [35].
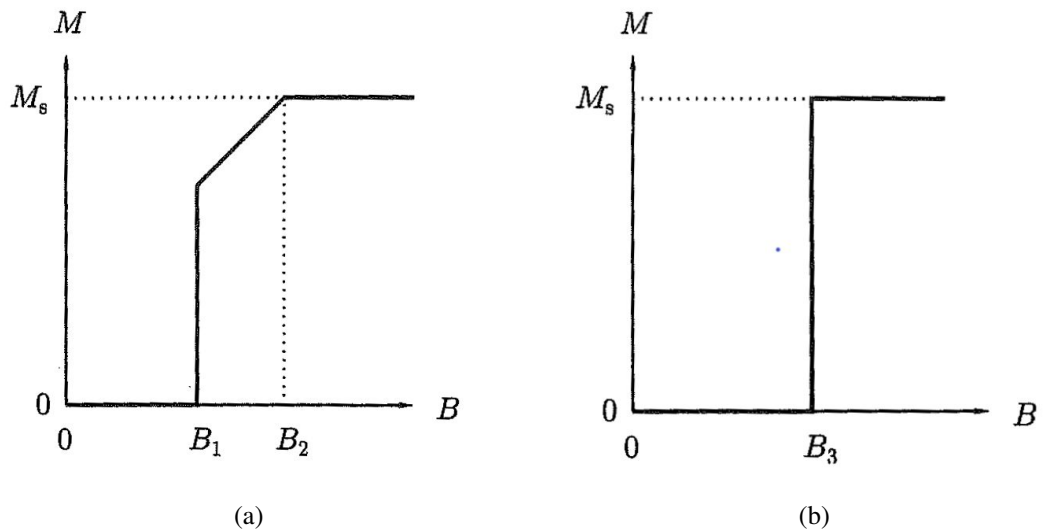

(a) (b)

Figure 4.4: If a parallel magnetic field is applied to an antiferromagnet (T = 0 K): (a) a spin-flop transition occurs at B_1, after which magnetic moments rotate until saturation is achieved at B_2. (b) a spin-flip occurs at B_3, if there is a strong preference for spins to lie along the parallel to applied field [35].

interaction between the layers can be described by a nearest-neighbour exchange constant J_1, a next-nearest-neighbour exchange constant J_2 and the angle between the magnetic moments in successive basal planes is Θ. And J_0 is the sum one all the exchange interactions of a given magnetic moment with other moments in the same ferromagnetically aligned (J_0, J_1, J_2 model [36]). The energy of this system (Figure 4.5a) is:

$$E = \frac{S^2}{2}(J_0 + 2J_1 \cos\Theta + 2J_2 \cos 2\Theta) \qquad (4.25)$$

where all spins have the same value S. The energy minimum is at points, where the first derivative is equal to zero, this is true when: $\theta = 0$ (ferromagnetism) or $\Theta = \pi$ (antiferromagnetism) or $\cos\Theta = -\frac{J_1}{4J_2}$. This last solution corresponds to helical order and has the lowest energy when $J_2 < 0$ and $|J_1| < 4|J_2|$ (Figure 4.5b).
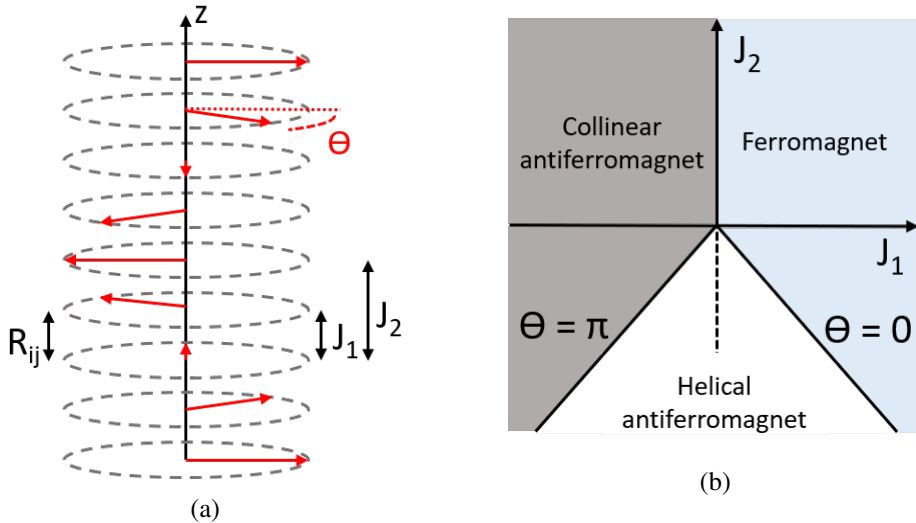

(a)

(b)

Figure 4.5: (a) Helical antiferromagnetic ordering. (b) The phase diagram for the model J_0, J_1, J_2 model [36]. In the helical antiferromegnetic region the turn angle between magnetic moments in adjacent layers along the helix axis $0 < \Theta < \pi$.

The indirect coupling mechanism that leads to magnetic interaction between the magnetic moments of the localised 4f-electrons in rear-earth metals is denoted the Rudderman-Kittel-Kasuya-Yosida (RKKY)-interaction. Large but localized magnetic moments interact through the spin polarization of itinerant conduction band electrons. It is a long-range interaction and has an oscillatory dependence on the distancw bwtween the magnetic moments $|\mathbf{R}_i - \mathbf{R}_j|$. The coupling of the localised spins with the electron gas is treated as a perturbation to the Hamiltonian of the

free electron system and described by a Heisenberg Hamiltonian of the type:

$$\hat{H} = -\sum_{i,j} J_{i,j}^{\text{RKKY}} \hat{\mathbf{S}}_{\mathbf{j}} \hat{\mathbf{S}}_{\mathbf{i}} \tag{4.26}$$

where indirect exchange constant [37]:

$$J_{i,j}^{\text{RKKY}} = \frac{J^2 \mathbf{k}_F^6}{E_F} \frac{h^2 V^2}{N^2 (2\pi)^3} F(2\mathbf{k}_F R_{ij}) \tag{4.27}$$

$$F(2\mathbf{k}_F R_{ij}) = \frac{\sin 2\mathbf{k}_F R_{ij} - x \cos 2\mathbf{k}_F R_{ij}}{(2\mathbf{k}_F R_{ij})^4} \tag{4.28}$$

Here J is the direct exchange constant, E_F the Fermi energy of the free electron gas, $\mathbf{k}_F$ corresponding Fermi vector, R_{ij} distance between two spins, V the volume of the system and N the number of electrons in the system. The exchange constant gets an oscillatory behaviour through the function of the distance between magnetic ions. Thus, depending on the separation R_{ij}, the interaction is either ferromagnetic or antiferromagnetic.

Since the pitch of the spiral generally is not commensurate with the lattice parameter, no layer in the crystal will have exactly the same spin direction, thus spatial oscillation of J_{ij}^{RKKY} describes helical order. A further feature is the large effect of the crystal field in rare-earth metals. The crystal field influences the shape of the electron orbits and through spin orbit coupling indirectly the alignment of the spins. The long-range and oscillatory indirect exchange gives rise to incommensurable periodic structures, the crystal fields and anisotropic two-ion coupling induce magnetic anisotropy and the magnetoelastic interactions cause magnetostriction strains.

The magnetostriction ,which was first discovered by Joule in 1842 in Nickel [38], is the effect of material dimensions change depending on change in magnetisation. It is commonly measured as the relative change of the length or volume of a material:

$$\text{Linear magnetostriction : } \lambda = \frac{\Delta l(T, B)}{l} \tag{4.29}$$

$$\text{Volume magnetostriction : } \omega = \frac{\Delta V(T, B)}{V} \tag{4.30}$$

Magnetostriction effects can be categorized into two types based on the driving mechanism:

1. forced magnetostriction, when the change in magnetisation is due to the application of an external magnetic field

2. spontaneous magnetostriction, when the magnetisation change is temperature driven

The atoms in the crystal lattice assume the energetically favorable position that minimizes their free energy which has a contribution of the harmonic elastic energy potential, the potential due to RKKY-exchange striction, and the potential due to the crystal field contribution. The details for the theory are summarized in a review by Doerr et al. [39].

Here, it is important to describe the effect of a magnetic field applied in the plane of a helical structure. As the field is increased, the helical first distorts and undergoes a first-order transition to a fan structure, in which the momenta oscillate from layer to layer about the field direction. A further increase in the field reduces the opening angle of the fan which, in the absence of magnetic anisotropy, goes continuously to zero, establishing a ferromagnetic phase at a second-order transition. The analytical mean-field treatment of the effect of a magnetic field on periodic magnetic structure was done by Nagamiya et al [40] for the helical structure without planar anisotropy, to which the field was applied in the plane. The ferromagnetic structure is reached at a field:

$$\mathbf{B_c} = \frac{\mathbf{S}[J(\mathbf{q}) - J(\mathbf{0})]}{g\mu_B} \qquad (4.31)$$

Here $\mathbf{q}$ is the wave vector for which indirect-interaction $J(\mathbf{q})$ has its maximum value. There is an intermediate transition, occurring approximately $\frac{\mathbf{B_c}}{2}$, at which the helix transforms abruptly to a fan structure, in which moments make an angle Θ with the field direction. The nature of intermediate stable helifan phase may be considered as blocks of moments with components alternately parallel and antiparallel to the field (Figure 4.6) [33].
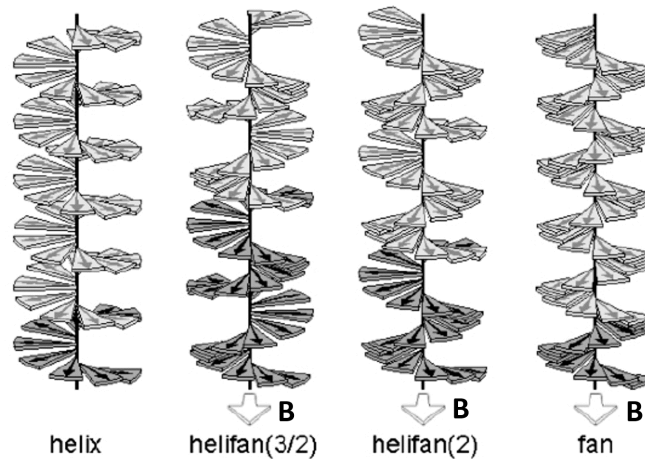

Figure 4.6: The helix, helifan(3/2), helifan(2) and fan structure on the example of Holmium at 80 K [41]. A magnetic field **B** is applied along the b-axis in the basal plane to the helifans and fan. The moments lie in planes and their relative orientations, indicated by arrows, rotate from plane to plane. The shaded parts of the illustrations indicate the respective magnetic unit cells.

4.6 Spin density wave

Spin density waves were first postulated by Overhauser in 1962 [42]. In mean-field theory, it is stated that all spins "feel" an identical average exchange field produced by all their neighbours. In metals, the molecular field can magnetise the electron gas due to Pauli paramagnetism χ_P. In this regard, the condition for system to become ferromagnetic and save energy is known as the Stoner criterion: $Ug(E_F) \geq 1$, where U is a measure of the Coulomb energy and $g(E_F)$ is a density of states at the Fermi energy. Thus, the condition for spontaneous ferromagnetism is strong Coulomb interactions and a large density of states at the Fermi energy. The Coulomb interaction leads to enhancement of magnetic susceptibility χ_P by a factor of $(1 - Ug(E_F))^{-1}$, this phenomenon known as Stoner enhancement. In addition, the q-dependent susceptibility $\chi_q^0 = \chi_P f(q/2k_F)$ is also enhanced and its maximum may occur at $q \neq 0$. Therefore, an oscillatory static magnetisation could spontaneously develop in the sample, and in the general case the order is spin-density wave (SDW) structures with wave vector **q**. The results for 1,2,3-dimensional q-dependent susceptibility for the electron gas is shown in Figure (4.7). The peak
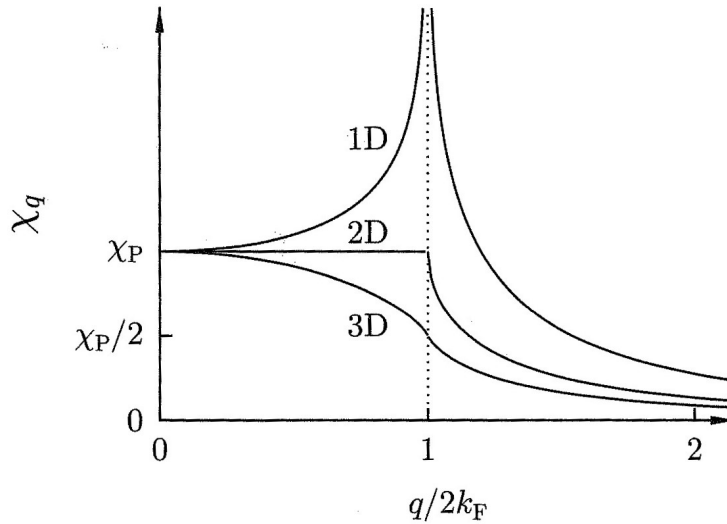

Figure 4.7: The paramagnetic susceptibility dependence of wave vector **q** in 1,2,3-dimensions. The dependence in 1-dimension diverges at $q = 2k_F$, this is known as a Kohn anomaly [35]

in one-dimension at $q = 2k_F$ is known as a Kohn anomaly and shows that electron gas is unstable to the formation of spin density waves with wave vector $2k_F$. Thus a periodic modulation of the magnetisation with wavelength $2\pi/q$ and wave vector **q** opens up a gap in the energy dispersion. If $q/2 = k_F$ the gap is at the Fermi surface and this reduces the total energy. A SDW can produce

energy gaps along the Fermi surface region, for which one part of the surface with translation by a vector **q** can be placed on top of another part (Fermi surface nesting Figure 4.9). If the nesting wave vector $|\mathbf{q}| \sim \pi/a$, where a is the spacing between atoms, the spin density wave is commensurate with the antiferromagnetic order lattice; otherwise it is incommensurate.
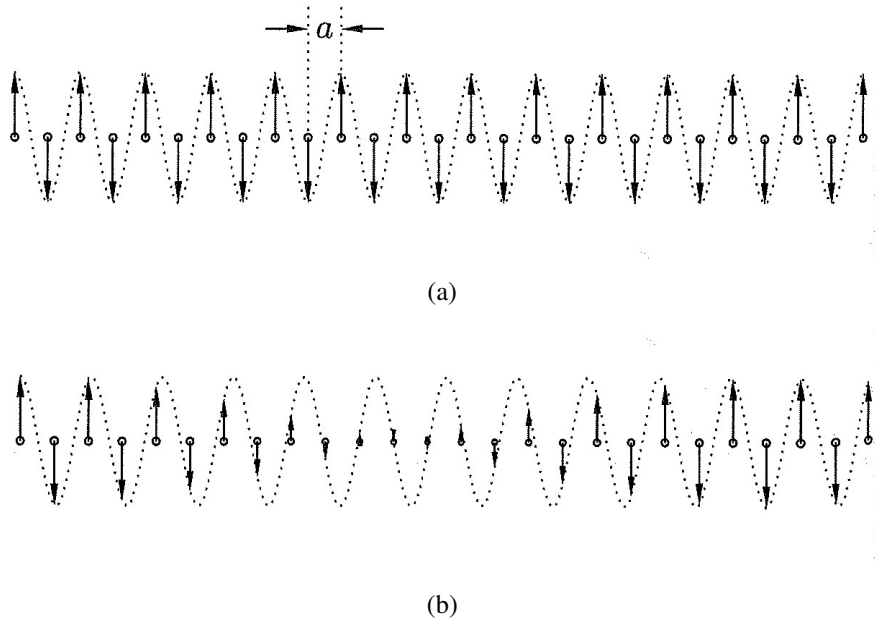

(a)

(b)

Figure 4.8: (a) Commensurate spin density wave with wave vector $q = \pi/a$. (b) Incommensurate spin density wave. [35]

4.7 Charge density wave

Density waves are broken symmetry states in metals caused by electron-phonon or electron-electron interactions. The ground states are the coherent superposition of electron-hole pairs and displays periodic spatial variation. Charge density waves were first discussed by Fröhlich in 1954 [43] and by Peierls in 1955 [44]. It was recognised that highly anisotropic band structures are important in leading to these ground states. Periodic charge density modulation is accompanied by a periodic lattice distortion, both periods being determined by the Fermi wavevector k_F. It is described by the behavior of a one-dimensional coupled electron-lattice system, with the electrons forming a one-dimensional electron gas, and the ions forming a linear chain. To describe the transition to the charge density wave ground state here considered a one-dimensional free electron gas coupled to the underlying chain of ions through electron-phonon interaction. In this case the Fröhlich Hamiltonian is written as:

$$\hat{H} = \hat{H}_{\text{electron}} + \hat{H}_{\text{phonon}} + \hat{H}_{\text{electron-phonon interaction}} =$$
$$= \sum_k \varepsilon_k \hat{a}_k^\dagger \hat{a}_k + \sum_q \hbar \omega_q \hat{b}_q^\dagger \hat{b}_q + \sum_{k,q} g_q \hat{a}_{k+q}^\dagger \hat{a}_k (\hat{b}_{-q}^\dagger + \hat{b}_q) \tag{4.32}$$

where $\hat{a}_k^\dagger$ and $\hat{a}_k$ are the creation and annihilation operators for electron states with energy $\varepsilon_k = \hbar^2 k^2 / 2m$, $\hat{b}_k^\dagger$ and $\hat{b}_k$ are the creation and annihilation operators for phonons characterised by the wave vector q, g_q is the electron-phonon coupling constant. The effect of the electron-phonon interaction on the lattice vibrations can be described by establishing the equation of motion of the normal coordinates. This equation and the underlying math can be found in Ref. [45], which gives a renormalised phonon frequency:

$$\omega_{\text{ren, q}}^2 = \omega_q^2 + \frac{2g^2 \omega_q}{M\hbar} \chi(q, T) \qquad , \text{here M is ionic mass} \tag{4.33}$$

One-dimensional electron gas $\chi(q, T)$ has maximum value at $q = 2k_F$. The transition temperature, when a distortion occurs defines when renormalised phonon frequency goes to zero:

$$k_B T_{\text{CDW}}^{\text{MF}} = 1.14 \varepsilon_0 e^{-1/\lambda} \tag{4.34}$$

where λ is the dimensionless electron-phonon coupling constant.

$$\lambda = \frac{g^2 n(\varepsilon_F)}{\hbar \omega_{2k_F}} \tag{4.35}$$

Below the phase transition the renormalized phonon frequency is zero, indicating a lattice distortion. Through a series of calculations with Hamiltonian, which can be found here [46], it is shown that instead of the linear dispersion relation for metallic state $\varepsilon_k - \varepsilon_F = \hbar v_f (k - k_F)$ the spectrum of excitations develops a gap in the charge density wave state. The opening of the gap leads to the lowering of the electronic energy and the lattice distortion leads to an increase in the elastic energy. By comparing the total energy for normal state and for the CDW ground state in 1D, it is confirmed that the latter is more energetically favorable. The dispersion relation, the electronic density and the equilibrium lattice positions are shown both above $T_{\text{CDW}}^{\text{MF}}$ and at $T = 0$ in figure (here the density wave is commensurate).

At finite temperature, thermally induced transitions across the gap lead to the screening of the electron-phonon interaction, to the reduction of the energy gain by the gap, and eventually to a phase transition. Under the assumption that photons act as a static potential on the electrons, a CDW is described as an electron-hole pair condensation in the same was as Bardeen–Cooper–Schrieffer (BCS) theory describe a condensate of electron-electron pairs lead-
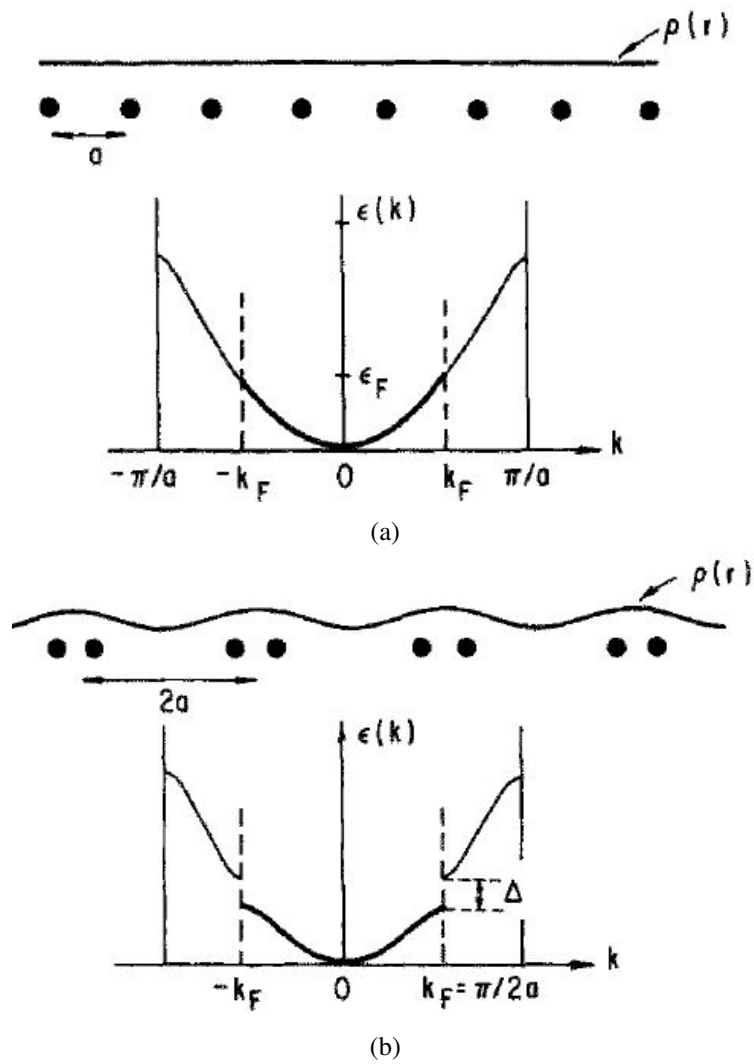
Figure 4.9: The single particle band, electron density, and lattice distortion in the metallic state (a) above $T_{\text{CDW}}^{\text{MF}}$ (b) in the charge density waev state at T = 0 K [46].

ing to superconductivity. Due to this significant overlap between the mean-field description of CDW and the BCS theory of superconductivity, the gap temperature dependence $\Delta(T)$ the same as given by the BCS theory:

$$\frac{\mid \Delta(T) \mid}{\mid \Delta(0) \mid} = 1.74 \left(1 - \frac{T}{T_{\text{CDW}}^{\text{MF}}} \right)^{1/2} \tag{4.36}$$
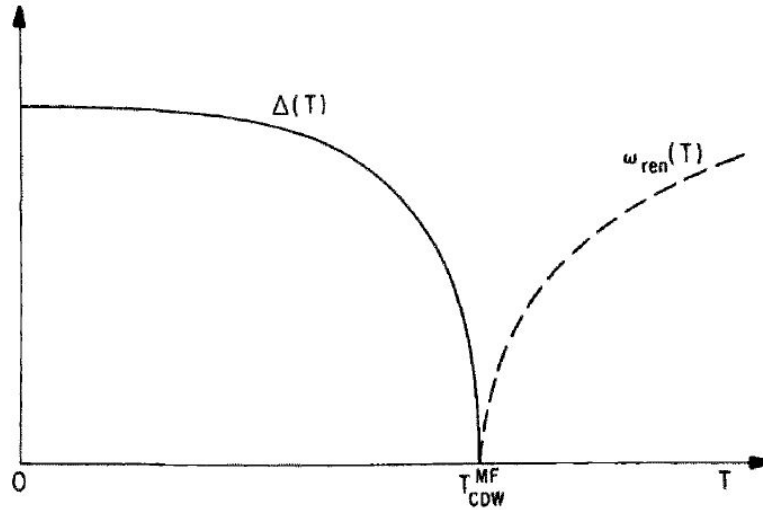

Figure 4.10: The temperature dependence of the magnitude of the single particle gap $\Delta(T)$ for $T < T_{\text{CDW}}^{\text{MF}}$. The renormalised phnon frequency $\omega_{\text{ren},2k_F}^2$ for $T > T_{\text{CDW}}^{\text{MF}}$ [46].

Both SDW and CDW ground states open up a gap at Fermi level, however the CDW develops as a consequence of electron-phonon interaction and SDW is arised as a consequence of electron-electron interaction. The nature of the relationship between CDW and SDW remains the subject of research.

5 Experimental method concepts

5.1 X-ray scattering from a crystal

The simplest approach to scattering is based on the concept of a plane wave. A wave is plane if its phase is constant at any point in the plane perpendicular to the direction of its propagation (wave front). When such a wave interacts with a three-dimensional atomic lattice, each scattering center produce spherical waves. Thus, it is convenient to use the wavevector $\mathbf{k}$ to describe the incident wave and $\mathbf{k}'$ for scattered wave. At the position $\mathbf{r}$ the phase difference is $\Delta\phi(\mathbf{r}) = (\mathbf{k} - \mathbf{k}') \cdot \mathbf{r} = \mathbf{Q} \cdot \mathbf{r}$. Thus the scattering vector is defined as:

$$\mathbf{Q} = \mathbf{k} - \mathbf{k}', \text{ which is usually expressed in units of } \text{Å}^{-1} \tag{5.1}$$

The atom can be represented as a nucleus surrounded by a charge cloud with electron density $\rho(\mathbf{r})$. Thus, the scattered amplitude is estimated by integrating over the volume elements $d\mathbf{r}$, taking into account the phase factor $e^{i\mathbf{Q}\mathbf{r}}$:

$$f^0(\mathbf{Q}) = \int \rho(\mathbf{r}) e^{i\mathbf{Q}\cdot\mathbf{r}} d\mathbf{r} \tag{5.2}$$

where, $f^0(\mathbf{Q})$ is the atomic form factor. The crystal lattice can be presented as a group of atoms. The smallest group of atoms, which has the overall symmetry of a crystal, and from which the entire crystalline lattice can be built up by periodic arrangement in three dimensions is called the unit cell. It is characterised with 3 edges a, b and c and 3 angles α, β and γ between the respective edges). To specify the lattice a set of vectors $\mathbf{R}_n = n_1\mathbf{a} + n_2\mathbf{b} + n_3\mathbf{c}$ can be used, where $\mathbf{a}, \mathbf{b}, \mathbf{c}$ are the lattice vectors (basis) and n_1, n_2, n_3 are integers. A given lattice has characteristic symmetries: translations, rotations, reflections, and compound symmetries.

Based on description of the scattered amplitude by atom, the scattered amplitude by the unit cell is:

$$F^{\text{unit cell}}(\mathbf{Q}) = \sum_j f_j(\mathbf{Q}) e^{i\mathbf{Q}\cdot\mathbf{r_j}} \tag{5.3}$$

where $f_j(\mathbf{Q})$ is the atomic form factor at $\mathbf{r_j}$ position of an atom within the unit cell.

The scattering amplitude from a crystalline material is calculated as a composition of unit

cells:

$$F^{\text{crystal}}(\mathbf{Q}) = \sum_j f_j(\mathbf{Q}) e^{i\mathbf{Q}\cdot\mathbf{r_j}} \sum_n e^{i\mathbf{Q}\cdot\mathbf{R_n}} \qquad (5.4)$$

Here, the second sum is the sum of phase factors, which is close to 1 except, when all phases are multiple 2π:

$$\mathbf{Q}\cdot\mathbf{R_n} = 2\pi \times \text{integer} \qquad (5.5)$$

To find a solution, it is necessary to construct a lattice in the wavevector space. This space of wave vectors is called the reciprocal space, it is defined by the basis vectors, which fulfill:

$$\mathbf{a}^* \cdot \mathbf{b}^* = 2\pi\delta_{ij} \qquad (5.6)$$

,where δ_{ij} is the Kronecker delta, defined so that $\delta_{ij} = 1$ if $i = j$, otherwise $\delta_{ij} = 0$. Thus, the points on the reciprocal lattice are described with the vector $\mathbf{G} = h\mathbf{a}^* + k\mathbf{b}^* + l\mathbf{c}^*$, where (h,k,l) all integers (Miller indices). The general relationship between the direct and reciprocal space can be understood by considering the Fourier transform of the one-dimensional lattice function. The corresponding X-ray diffraction condition in the reciprocal space is:

$$\mathbf{Q} = \mathbf{G} \qquad (5.7)$$

Thus, the condition for non-vanishing of the scattering amplitude on the crystal is the vector equation for the scattering vector and the reciprocal lattice vector. This equation is the Laue condition for the observation of X-ray diffraction. If the wavelength of X-rays is close to the distance between the scattering centres, the result of adding the amplitudes of all scattered waves is the formation of strong reflections along several directions. The other description of diffraction phenomenon for a crystal was obtained by Bragg [47]. Strong diffraction peak is a result of adding all waves in phase, in case of crystalline planes the condition to be fulfilled for diffraction is:

$$n\lambda = 2d\sin\theta \qquad (5.8)$$

Here, n is integer, to describe the order of diffraction reflection; λ is a wavelength; d is a distance between reflecting planes; θ is an angle between scattering plane and incident or diffracted beam (Figure 5.1).

The crystalline arrangement can be formally defined by the Bravais concept, in which all the atoms at specific lattice points are identical or the surrounding of each lattice point is the same. The 14 Bravais lattices are grouped into 7 lattice systems. On the other hand, crystal system is a set of point groups (the group of geometric symmetries with at least one fixed point) and
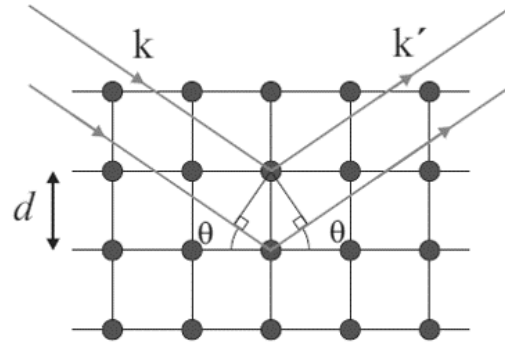
Figure 5.1: Bragg diffraction in 2D square lattice. The wave with wave vector **k** and incident angle θ elastically scatters by atoms in planes at a distance d with reflected angle θ and wave vector **k**′ [48].

corresponding space groups (the symmetry group in three dimensions), which are assigned to a lattice system. Here we will not go into details of crystallography, which can be found, for example, in Ref [49]. This project is focused on two types of crystalline structure:

1. body-centered cubic (bcc): unit cell vectors $a = b = c$ and angles $\alpha = \beta = \gamma = 90°$;

2. hexagonal close-packed (hcp): unit cell vectors $a = b, c$ and angles $\alpha = \beta = 90°, \gamma = 120°$;

The X-ray diffraction from the crystalline material is formed by scattering from atoms that are lying within families of planes. These planes are conveniently described using the Miller indices, defined in such a way that the plane closest to the origin has intercepts $(a/h, b/k, c/l)$ on the axes $(\mathbf{a}, \mathbf{b}, \mathbf{c})$. For a given equally spaced plane family it is possible to define the lattice spacing d:

$$\text{for cubic lattice } \frac{1}{d^2} = \frac{h^2 + k^2 + l^2}{a^2} \tag{5.9}$$

$$\text{for hexagonal lattice } \frac{1}{d^2} = \frac{3}{4}\left(\frac{h^2 + hk + k^2}{a^2}\right) + \frac{l^2}{c^2} \tag{5.10}$$

However, even when a set of lattice planes of a crystal satisfies the Bragg condition, its reflection intensity may vanishes if its crystal structure factor F^{crystal} turns to zero. Such a reflection is called forbidden reflection and the selection corresponding lattice planes is defined based on type on the unit cell with diffraction selection rules. In our case:

Unit cell type	Allowed reflection	Forbidden reflection
body-centered cubic	$h + k + l$ even	$h + k + l$ odd
hexagonal close-packed	l even and $h + 2k \neq 3n$	l odd or $h + 2k = 3n$

Ewald proposed a simple geometric construction that makes it possible to visualize various experimental methods methods for determining the crystal structure. For this, a sphere is constructed with its center at the end of the wave vector **k** of the incident wave and with radius $|\mathbf{k}|$, which is passing through the origin of the reciprocal lattice. Thus, for the existence of a wave vector $\mathbf{k}'$, which satisfies the Laue condition, it is needed that one of the points of the reciprocal lattice, in addition to the initial one, lies on the surface of the sphere. In this case Bragg reflection takes place from a planes family in direct lattice perpendicular to this reciprocal lattice vector [48].

In addition to scattering, any radiation is absorbed to some level in the material. This phenomenon is well described by the Beer-Lambert law:

$$\frac{I}{I_0} = \exp\left(-\mu t\right) \tag{5.11}$$

Here, I and I_0 are penetrated and incident radiation intensity, μ is a linear absorption coefficient, t is distance travelled in the material.
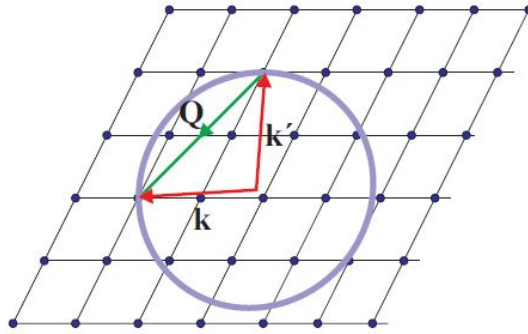

Figure 5.2: The Ewald circle in two dimensions (purple). The reciprocal lattice (black) with scattering triangle: the incident radiation with wave vector **k**, which terminating on the origin of the reciprocal lattice (red); the scattered radiation with wave vector $\mathbf{k}'$, which is terminating on the circle of radius k (red) and scattering vector **Q** (green). The scattering occurs if one or more reciprocal lattice points fall on the Ewald circle. [48].

5.2 Non-resonant X-ray magnetic scattering

Non-resonant X-ray magnetic scattering (NRXMS) is one of the techniques to study the magnetic structure. Since X-rays are an electromagnetic wave, they are sensitive to both magnetic and charge distribution in condensed matter. The key properties of NRXMS are: the difference in

contribution from orbital (L) and spin (S) angular momentous; and the simple correspondence between measured structure factor and magnetisation. Furthermore, NRXMS studies benefits from the high-Q resolution available at new bright X-ray sources like XFELs. This method finds applications in three directions: magnetic Compton scattering [50], magnetic Bragg scattering at high energy [51], and experimental separation of L and S [52].

In the 1970s theoretical and experimental studies showed that X-rays can be scattered not only by the charge distribution, but also by the magnetic order within materials. This came out of relativistic treatment of photon scattering, where terms coupling to the spin and orbital angular momentum of the electron appear in the cross-section. The generalization from the scattering from the single magnetic moment to the diffraction patterns of magnetic solids is built up from the fundamental amplitude of the interaction in the same way that the description of X-ray scattering purely from charge begins with Thomson scattering and introduces atomic scattering factors and finally structure function. Even with the large enhancement at absorption resonances, magnetic reflections are orders of magnitude weaker than charge scattering, so the kinematic limit of X-ray scattering applies. Thus, the total non-resonant scattering factor for a magnetic ion is the sum of Thomson scattering f_0, anomalous scattering correction and the magnetic contribution:

$$f = f_0 + f' + if'' + f_{\text{non-res}}^{(\text{mag})} \tag{5.12}$$

The Thomson scattering cross-section depends only on the classical radius of the electron r_0 and on the direction of the scattered radiation relative to the plane in which the incident beam is polarized.

$$f_0 = \rho(\mathbf{Q}) r_0 (\hat{\varepsilon} \times \hat{\varepsilon}') \tag{5.13}$$

Here $\hat{\varepsilon}$ is the polarisation of the incident beam and $\hat{\varepsilon}'$ is the polarisation of the scaterred beam. The magnetic scattering factor, as was mentioned above, depends on orbital the $\mathbf{L}(\mathbf{Q})$ and spin the $\mathbf{S}(\mathbf{Q})$ angular momenta:

$$f_{\text{non-res}}^{(\text{mag})} = ir_0 \frac{\hbar\omega}{mc^2} f_D \left[\frac{1}{2}\mathbf{L}(\mathbf{Q}) \times \mathbf{A} + \mathbf{S}(\mathbf{Q}) \times \mathbf{B} \right] \tag{5.14}$$

Here $\mathbf{A}$ and $\mathbf{B}$ matrices describe the polarization and energy dependence of the magnetic interaction. And f_D is the Debye-Waller factor, which is added to account for the effect of thermally excited perturbations of atomic order on magnetic scattering.

The intensity of the magnetic scattering is a small fraction of the intensity of structural reflection from Thomson scattering [53]. This is coming from the fact that all electrons contribute to the structural scattering, however only small fraction ordered spins of total number lead to a net magnetisation. For example in antiferromagnetic MnF_2 the non-resonant magnetic Bragg reflec-

tion is a factor of 10^8 smaller than the structural reflections coming from Thomson scattering. The ordered magnetic moment in the antiferromagnetic lattice corresponds to 1 electron out of a unit cell consisting of 48 electrons [51]. A similar large ratio is expected for all other materials including Cr.

Non-resonant magnetic scattering from Cr is well understood in terms of the magnetic cross-section [54]. In scattering geometry used in experiments with Cr in this project, the polarization of the SDW is perpendicular to the scattering vector in the transverse phase (TSDW, spins are perpendicular to the direction of the wave vector) and parallel to it in the longitudinal phase (LSDW, spins are parallel to the direction of the wave vector). Blume and Gibbs [55] have shown that the magnetic scattering arising from the non-resonant cross-section is most sensitive to the component of the SDW, which is perpendicular to the scattering plane. Furthermore because the magnetism of Cr arises purely from electron spin angular momentum, the cross-section given in equation 5.16 can be simplified. The intensity of the magnetic scattering from Cr:

$$ I \sim [\mathbf{S}(\mathbf{Q})(\hat{k}\times\hat{k}')]^2 + \left[\frac{Q^2}{2k^2}\mathbf{S}(\mathbf{Q})\hat{k}\right]^2 \tag{5.15} $$

The factor $\frac{Q^2}{2k^2} = 2\sin^2\theta_{\text{Bragg}}$ for hard X-ray photon energies makes contribution of the second term much smaller than the first. To a good approximation, the resulting cross-section of $[\mathbf{S}(\mathbf{Q})(\hat{k}\times\hat{k}')]^2$, which is proportional to the magnitude of the spin pointing out of the diffraction plane defined by incident and diffracted beam wavevectors $\hat{k}$ and $\hat{k}'$. The crystal orientation, with [100] and [010] as in-plane directions, with respect to the scattering plane, and the fact that the Cr SDW polarization vector is along the principal lattice directions means that there always will be a component perpendicular to the scattering plane in the transverse phase for the (001) reflection. In the longitudinal phase the polarization is always parallel to the scattering plane for the (001) reflection.

5.3 Formation of satellites

A long-range order at the atomic level is defining the periodical crystal structure, which allows it to be described as a lattice of unit cells. However for a long time it is known that certain crystalline materials are not periodic, which means that the position of the atoms is modulated with a wavelength that is an irrational fraction of a lattice parameter. Such materials are called incommensurate. As was mentioned in 4 in case of chromium the CDW and SDW modulations are incommensurate with the crystal lattice and this new periodicity in the sample induces new reciprocal lattice points where scattering is observed. A simple example for this 1D crystal with

only 1 atom per unit cell, *n* number of unit cells and with lattice parameter *a*. It's electron density with CDW phase is:

$$\rho(x) = \sum_{n=1}^{N_{\text{cell}}} \rho_{\text{at}}[x + na + \Delta_x \cos \mathbf{q}_{\text{CDW}} na] \tag{5.16}$$

where $\Delta_x = \sqrt{\frac{2\hbar}{NM\omega(2k_F)}} \frac{\Delta}{g(2k_F)}$ is the amplitude of the atoms displacement and $\mathbf{q}_{\text{CDW}}$ stands for the CDW wavevector [46]. Then the equation for diffracted amplitude is:

$$A(\mathbf{Q}) = \sum_n e^{i\mathbf{Q}[na + \Delta_x \cos \mathbf{q}_{\text{CDW}} na]} f_{\text{at}}(\mathbf{Q}) = \sum_n e^{i\mathbf{Q}na} e^{i\mathbf{Q}\Delta_x \cos \mathbf{q}_{\text{CDW}} na} f_{\text{at}}(\mathbf{Q}) \tag{5.17}$$

Assuming Δ_x to be small enough to apply the Taylor expansion of the second phase factor around $i\mathbf{Q}\Delta_x$:

$$\frac{A(\mathbf{Q})}{f_{\text{at}}(\mathbf{Q})} \approx \sum_n e^{-i\mathbf{Q}na}[1 - i\mathbf{Q}\Delta_x \cos q_{\text{CDW}} na] f_{\text{at}}(\mathbf{Q}) =$$

$$= \sum_n e^{-i\mathbf{Q}na} - i\mathbf{Q}\frac{\Delta_x}{2} \left(\sum_n e^{-i(\mathbf{Q}+\mathbf{q}_{\text{CDW}})na} + \sum_n e^{-i(\mathbf{Q}-\mathbf{q}_{\text{CDW}})na} \right) \tag{5.18}$$

The final equation 5.18 consist of three sums: the first one is standing for the perfect 1D crystal Bragg reflections; the second term satisfies the Laue condition, when $\mathbf{Q} + \mathbf{q}_{\text{CDW}} = \mathbf{G}_h \rightarrow \mathbf{Q} = \mathbf{G}_h - \mathbf{q}_{\text{CDW}}$, it is CDW satellite peak at a distance of q_{CDW} from Bragg; and the last term is the CDW satellite from the other side of Bragg reflection at $\mathbf{Q} = \mathbf{G}_h + \mathbf{q}_{\text{CDW}}$ (Figure 5.3). This equation is correct for non-resonant X-ray diffraction, which is the method used in this project. Finally, equation 5.18 is correct at zero temperature. In order to take the temperature effect into account the expression need to be multiplied by a Debye-Waller factor. Based on this simple 1D case, a more general formula can be given for a three dimensional CDW crystal phase with more than 1 atom per unit cell (using Taylor expansion in the first order on the small parameter $\Delta_{x,i}$):

$$A_{\text{CDW}}(\mathbf{Q}) = \sum_{n_1 n_2 n_3} e^{-i\mathbf{Q}\mathbf{R}_{n_1 n_2 n_3}} \sum_{p=1}^{N_{\text{at}}} e^{-i\mathbf{Q}\mathbf{r}_p} f_{\text{at p}}(\mathbf{Q})$$

$$- i\frac{1}{2} \sum_{i=1}^{N_{\text{at, CDW}}} \mathbf{Q}\mathbf{u}_i \Delta_{x,i} e^{-i\mathbf{Q}\mathbf{r}_i} f_{\text{at i}}(\mathbf{Q}) \times \tag{5.19}$$

$$\sum_{n_1 n_2 n_3} \left[e^{-i(\mathbf{Q}-\mathbf{q}_{\text{CDW}})\mathbf{R}_{n_1 n_2 n_3}} + e^{-i(\mathbf{Q}+\mathbf{q}_{\text{CDW}})\mathbf{R}_{n_1 n_2 n_3}} \right]$$

where $f_{\text{at p}}(\mathbf{Q})$ is atomic form factor for atom p. The first term is the sum of all the atoms in the unit cell, thus this term corresponds to the crystal lattice Bragg peak. The last sum corresponds to CDW satellite peaks from both sides of Bragg peak. And the term in the middle is the

modulation of intensity, which can be seen as a structural factor for the displaced atoms. As it is shown in the equation 5.19 the structural factor for the CDW satellites peaks and the Bragg peaks are not connected, thus, the reflection intensities are also independent of each other in experimental measurements [56].
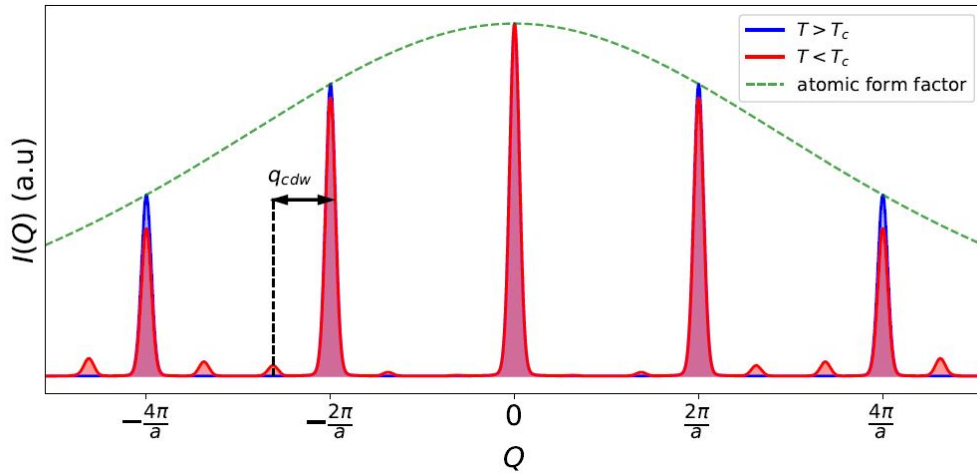

.

Figure 5.3: Comparison of diffracted pattern from a 1D atomic chain above (blue) and below (red) the CDW transition temperature T_C. Several peaks named as CDW satellites, appear at a distance $\pm q_{\mathrm{CDW}}$ from the Bragg reflection [56]

6 Sample treatment and characterisation

6.1 X-ray diffractometer

One of the first steps for preparation of the experiments with crystalline samples is an orientation and structural characterisation. It is a crucial step in any measurement based on tracking of Bragg reflections, and even more important under the stringent time limitations for experiments at large-scale facilities like the European XFEL. Single-crystal X-ray diffraction is a common technique for the study of crystal structures. In this project we used the laboratory X-ray diffractometer (XRD) RÖDI at the Helmholz-Zentrum Geesthacht(HZG) located in The Petra III hall at DESY to clarify the orientation, evaluate the crystalline quality and miscut.

This diffractometer consists of: X-ray tube with copper anode, Goebel mirror, set of slits (during the measurements is commonly used 1 mm pinhole and 0.2 mm slit), goniometer and 2D detector Dectris with 1200 pixels and rotation angle 2θ (Figure 6.1). The goniometer sample stage provides motorised rotation in omega and chi directions and manual manual change of x and y positions (Figure 6.2c).
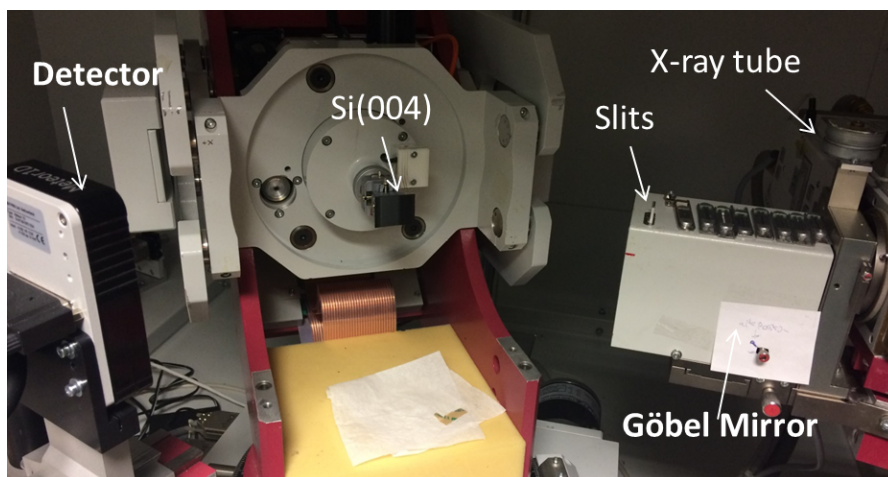

Figure 6.1: Diffractometer RÖDI in Helmholz-Zentrum Geesthacht(HZG)

The rocking curve of a crystal reflection is a plot showing the dependence of scattered X-ray intensity from the sample as a function of omega. It indicates the quality of the crystalline lattice.
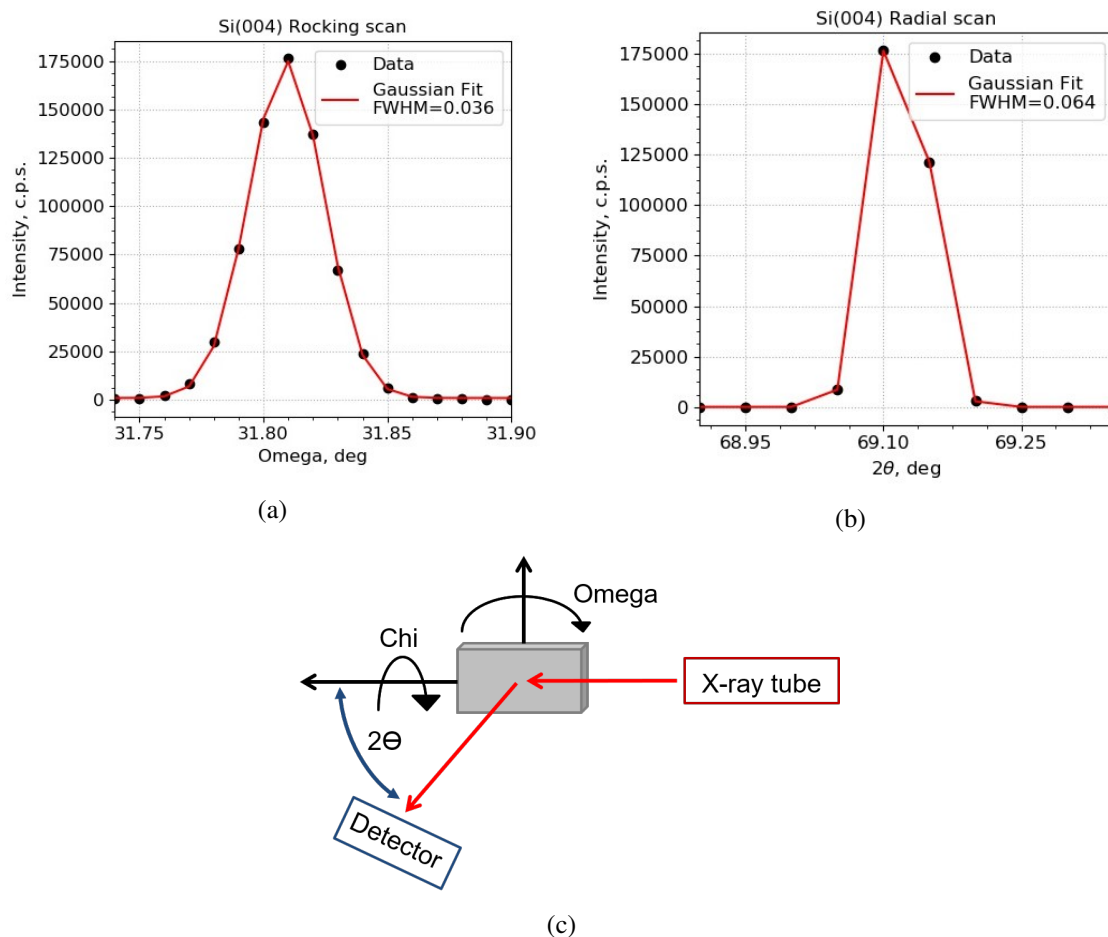
(a)

(b)

(c)

Figure 6.2: (a) The rocking scan for Si(004): dependence of reflection intensity on omega angle (sample rotation). For Si(004) reflection (FWHM) the theoretically calculated FWHM is about 0.001 deg. (b) The radial scan for Si(004): dependence of reflection intensity on 2θ angle (detector rotation). (c) The RÖDI diffractometer scheme with motors names.

The measurement resolution is limited and the resulting curve is a convolution of the geometric instrument profile, the wavelength profile and the specimen broadening function (imperfect crystal). In case of Si(004) reflection in a perfect crystal a theoretical curve full width on half maximum (FWHM) is ~ 0.001 deg and the measured curve FWHM = 0.036 deg. Thus, this curve gives a clear estimation of the RÖDI diffractometer resolution.

Crystal imperfections cause a broadening of the rocking curve. Usually the half-width of the measured rocking curve is compared to the one calculated assuming a perfect crystal.

During this project each sample was characterised several times in experiments using this and similar setups at the Technical University of Hamburg-Harburg and the Solid State Physics Laboratory at University Paris-Saclay (LPS, Paris-Saclay). Additionally, surface treatments were carried out to improve single crystal qualities: increase the intensity and decrease the Bragg reflection width using chemical etching and mechanical polishing.

Below is a list of the samples that were used in the measurements, the results of which will be presented in Chapter 8, with a brief description of the processing applied. Here we use the following notation: the Bragg reflection is described using a set of parallel reflecting planes (for bcc crystal (hkl) and for hcp $(hkil)$, where $i = -h - k$);

1. **Dysprosium (0001)** (Dy #1), Obtained from G. Gruebel (DESY), size 7 mm x 3.5 mm x 2 mm
   One side polished by MaTeck (May 2020)
   Bragg peak (0002) FWHM = 0.2 deg.
   Due to missing information about the manufacturer or any previous treatment, first of all it was proved that the crystal had (0001) orientation. To improve the crystal surface, which had visible damage (rough surface and scratches), it was decided to apply chemical etching. The original idea was to mix the etching agent in-house in the chemistry laboratory at XFEL to have opportunity of quick sample restoration in case of radiation damage during experiment. As a result of literature review [57] was found one variant of recipe and tested on a dummy Dy piece, using one drop for 2 sec on one side. Components were mixed in the following amounts and sequence:10 mL lactic acid (>80 %) ,20 mL acetic acid (100 %), 30 mL nitric acid (65 %), 10 mL phosphoric acid (85 %). However, the reflection parameters did not show any improvements (etching time and proportion of acids mixture need to be improved), thus within a limited time frame the sample was sent to MaTeck company for expert treatment.

2. **Chromium (100)** (Cr #2), MaTeck, disk with diameter 5 mm and thickness 1 mm
   One side polished and chemically etched in LPS, Paris-Saclay (Feb 2020)
   Bragg peak (002) FWHM = 0.12 deg.

During the first sample quality check the Cr(002) reflection was found, however its parameters could be improved (FWHM = 0.9 deg). Similar to Dy, the original idea was to practice in-house sample recovery, thus a first etching experiment was carried out in the laboratory using standard chromium etchant (TechniEtch Cr01) with support of the Sample Environment and Characterisation group at XFEL. Reflection parameter was improved to FWHM = 0.68 deg. To gain experience in chromium surface treatment next attempt was carried out in LPS, Paris-Saclay with Vincent Jacques. This time we used combination of mechanical polishing and chemical etching above room temperature, which results in better improvement of the reflection FWHM = 0.12 deg. This procedure will be described in more detail below.

3. **Chromium (100)** (Cr #3), MaTeck, diameter 5 mm, thickness 0.2 mm
   Bragg peak (002) FWHM = 0.08 deg.
   The reflection Cr(002) was found with a good quality. However, in order to carry out X-ray diffraction in transmission (Laue) geometry with 11 keV energy (the choice of energy is determined by the geometry of the experiment, which is described in more detail Chapter 7) and have sufficient reflected intensity on the detector, it was needed to decrease the thickness at least down to 0.1 mm. The first attempt to make the sample thinner was made using the Leica Microtome device in XFEL Biology Infrastructure laboratory. However the dimensions of the crystal were too big for efficient cutting. Also, a sharp diamond knife clung to the edge of the sample, which led to the breakage of the sample edges. As the alternative, was chosen time consuming, but reliable chemical etching procedure. To increase the efficiency and decrease the required time it was performed in several attendees with refreshing of acid. The heating plate kept etchant with sample at 50 degree Celsius. As a result of these procedure current thickness of the sample measured with electron microscopy is 50 micron, but as a drawback, the sample is a bit bent , it is not uniform across the diameter.

4. **Chromium (111)** (Cr #4), MaTeck, diameter 5 mm, thickness 1 mm, polished
   Bragg peak (002) FWHM = 0.08 deg. Reflection (002) was found with a good quality. No treatment was applied.

Repetition of the rocking curve measurements at different positions and several showed slight variety of peak characteristics, such as shape (appearance double peak structure or peak broadening) and intensity (up to 10 % difference between peak intensities), to orientation. This must be taken into account when aligning and searching for different kind of reflections. In case of magnetic field application, it is useful in addition to out of surface orientation, to know in plane axis orientations. To do this, we put Cr(011) plane in the reflecting position by setting the tilt

angle to 45 degrees (for sample with surface orientation (100)) and azimuthal rotation until the intensity appears on the detector. This azimuth position corresponds to one of the principal axes being parallel to the incoming X-rays.

6.2 Mechanical polishing and chemical etching

A common method to obtain a small-sized single-crystal piece is cutting from a plate using special disks with diamond abrasive edges. Before cutting, the ingots are oriented by the X-ray method so that the surface is parallel to the desired crystallographic plane. The second step is grinding to improve the alignment of the sides and achieve the required thickness parameters. After that, the mechanical polishing is carried out using diamond polishing paper, in order to reduce the surface roughness and depth of the destroyed layer inside of the crystal. The depth and structure of the deformed layer depend on a number of technological factors: abrasive material and particle size, polishing mode, process speed, etc (Figure 6.3a). The deformed surface layer of the single crystal has a complex structure and can be divided into two zones by thickness [58] (Figure 6.3b).
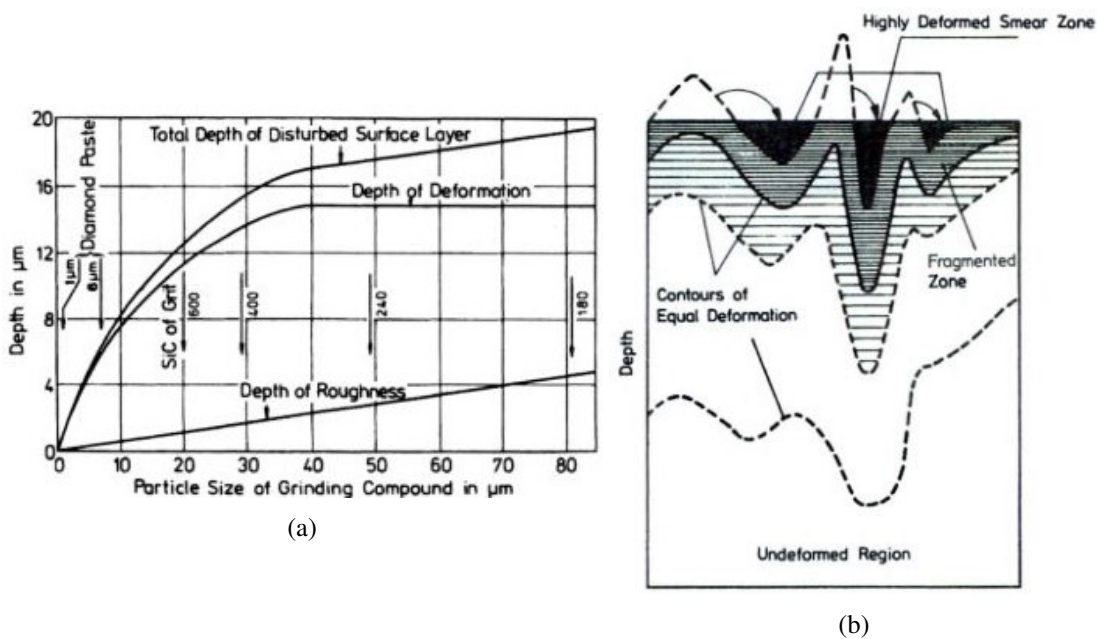

(a)

(b)

Figure 6.3: (a) Depth of surface roughness, deformation and total depth of the disturbed surface layer as a function of the abrasive particle size. (b) Schematic showing the cross-section of a surface region from a mechanically ground and polished sample [59].

The first zone is a system of misoriented local sections containing scratches and cracks. It can

be considered as a non-diffracting absorbing surface and conditionally amorphous layer. Cracks contain particles of abrasive and are surrounded by a system of dislocations. As a result of this, stressed regions appear at considerable distances leading to elastic deformations. Thus the second zone is like a mosaic crystal without mechanical damage, which absorbs radiation and scatters kinematically. In this zone due to the large elastic deformations the dimensions of the coherent scattering regions are much smaller than the extinction length. The phase difference along this length exceeds the distance between the dispersion surfaces, while during dynamic scattering it is much smaller.

This defected layer contributes to X-ray diffraction and the peak from it is wide and of low intensity. Thus improve the diffracted intensity it is necessary to remove the surface layer thicker. using chemical etching. Etching solution are capable of differentiation between local levels of potential energy at defect sites and normal level of potential energy in the perfect lattice. For the etching reaction at perfect lattice, the energy barrier is substantially higher than at the defect. Hence, etch rates at defect sites are higher than etch rates of the perfect lattice, giving rise to the formation of etching pits at defect sites. As a result of such etching, layers with deformations accumulated during mechanical treatment are removed and a single crystal remains with crystal parameters improved to theoretical calculations for an ideal crystal.

During the visit at Laboratoire de Physique des Solides in Paris, both mechanical polishing and chemical etching of chromium was carried out. This treatment was applied to the sample Cr #2 which was already used during PUMA setup commissioning, and it was not polished by supplier. First, chemical etching was applied for one hour on chromium using an etching acid from Sigma Aldrich (0.24 um/min etching speed at room temperature indicated). From the density of the material and the weight of the crystal, the volume could be calculated. Comparing the crystal volume before and after etching, the thickness of the removed layer is determined. However after placing whole crystal into etching for 65 min at room temperature with periodical stirring and refiling, the weight loss was much less than expected. Calculated from weight loss etching rate was 0.03 um/min, this is almost one order slower than the indicated etching speed. This difference may be related to the conditions and duration of acids mixture storage. Consequently, the rocking curves before and after this procedure did not really improve both in terms of FWHM and intensity of the Cr(002) peak. Thus, it was decided to carry out a manual mechanical polishing using diamond particle paper. The result of the surface change is easy to see with an optical microscope (Figure 6.4a). This treatment resulted in an increase in the width of the rocking curve as described above. Finally the sample was immersed in the etching acid again in two steps: first for 1 hour 45 minutes at room temperature (calculated etching rate = 0.007 um/min) and second for 1 hour 5 minutes at 40 degrees Celsius (calculated etching rate = 0.03 um/min) (Figure 6.4b). Important note is that no increase in etching rate at higher
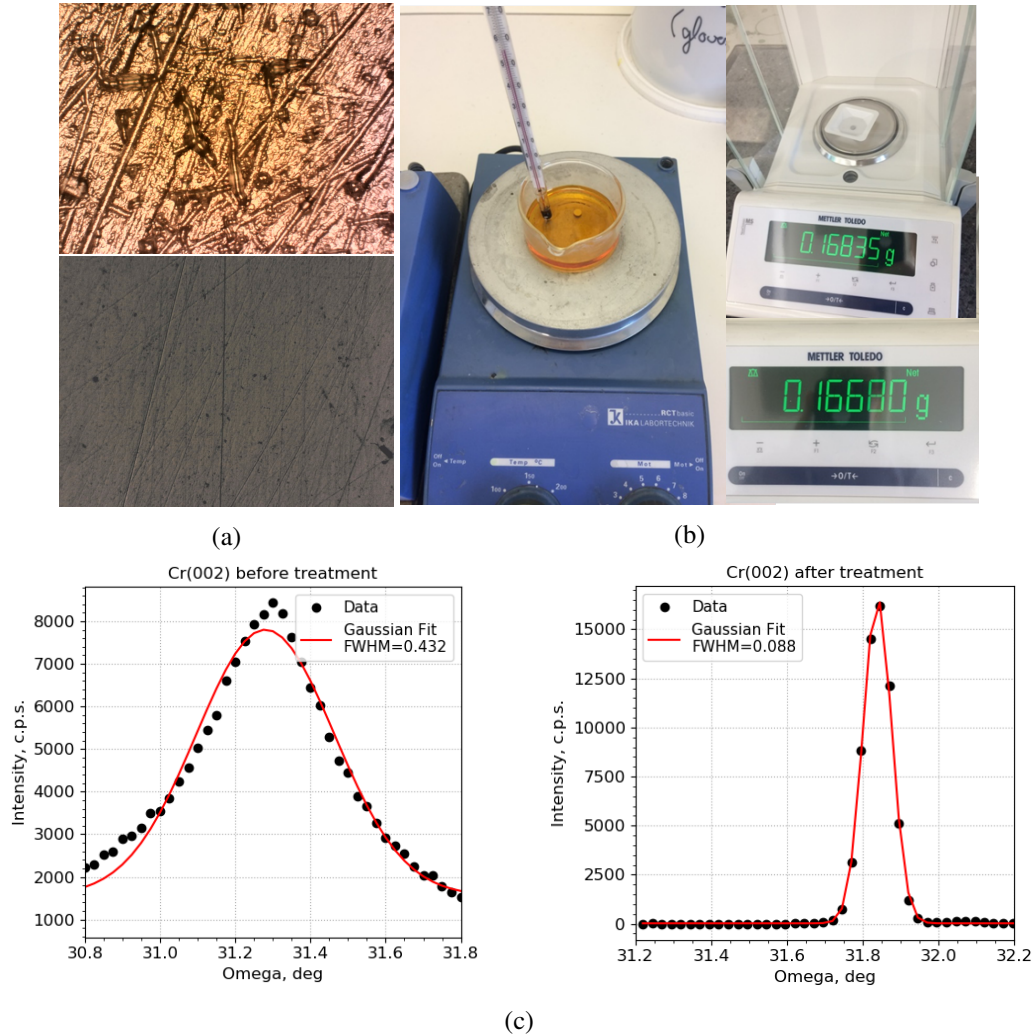
(a)

(b)

(c)

Figure 6.4: Mechanical polishing and chemical etching, which were carried out at LPS, Paris. (a) The sample surface made in the optical microscope before (top) and after (bottom) treatment (unfortunately, the dimension scale was not saved). (b) The sample is placed in the etchant on the heating plate. The thickness of removed layer was measured using sensitive scales. (c) The rocking curve Cr(002) for the sample measure before (left) and after (right) the treatment.

temperature was observed. However as the sum of all these steps the FWHM of Cr(002) was improved from 0.432 deg to 0.088 deg (Figure 6.4c). Despite the fact that the goal of improving the reflection was achieved, it would be useful to repeat and refine the procedure and study the temperature effects.

We did not observe expected etching rate increase both after mechanical polishing and during etching in above room temperature. There are many other parameters that affect the etching procedure, as described in variable literature sources (for example [58]). In this regard, procedure of Cr crystal structure improvement in laboratory need to be repeated more accurately.

6.3 Superconducting Quantum Interferometer Device

The critical temperature is characteristic for a sample which undergoes a magnetic transition. This temperature can differ from crystal to crystal based on a number of parameters: the conditions the crystal was growing under, the amount and types of defects in the bulk and at the surface, etc. As part of the experimental preparation in this project, it was useful to measure the spin-flip transition temperature in Cr, for this we used a Superconducting Quantum Interferometer Device (SQUID) at The Center for Free-Electron Laser Science (CFEL) in the Quantum Condensed Matter Dynamics group. This SQUID has sensitivity even to very small magnetic moments, its operation is based on three different physical phenomena: superconductivity, Josephson effect and magnetic flux quantization. This magnetometer consist of two parallel the Josephson junctions, which connects two halves of a superconducting ring. If a constant biasing current is maintained, the measured voltage fluctuation is associated with a change in the magnetic flux (Figure 6.5).

Superconducting material has a zero electrical resistance in low temperatures and form Cooper pairs electrons, which can tunnel through the weakly conducting layers (Josephson junction). Because of the phase difference of the Coopers pairs, wave functions on both sides of this contact an electrical direct current flow appears even in the absence of an externally applied voltage. Finally, the high sensitivity of this device is coming from the fact that superconducting rings can enclose magnetic flux only in multiples of a universal constant called the flux quantum, which is the smallest quantity of the magnetic flux [60].

Based on this construction SQUIDs detect the change of magnetic flux created by mechanically moving the sample through a superconducting pick-up coil, which is converted to a voltage. The standard sequence: $M(T)$ curve is measured in the field 1000 Oe from 2 K to 300 K (feild-heated) in the mode without stabilisation of the temperature from the actual measurement with 0.5 K/min from 2 K to 20 K and with 5 K/min from 20 K to 300 K. Afterwards the sample is cooled down to 2 K in nominally zero-field and another $M(T)$ curve is measured at 1000 Oe with
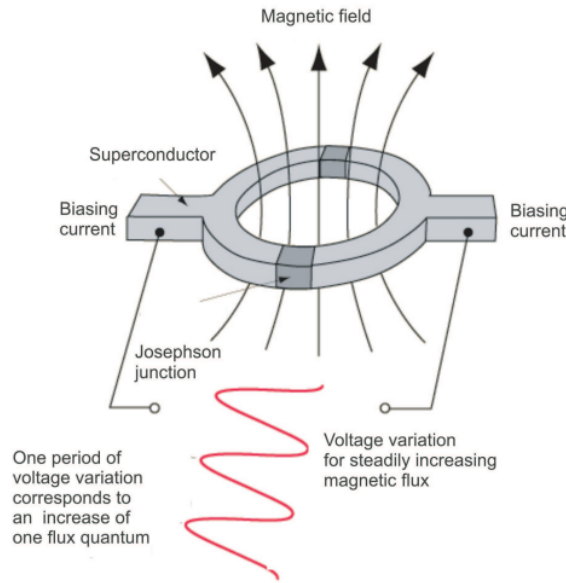
Figure 6.5: Principle of SQUID magnetometer [60].

identical step-sizes now cooling the sample from 300 K to 2 K [61]. Thus, in case of Cr samples we expect to see characteristic step on the smooth $M(T)$ curve around the spin-flip transition due to the change of spin density wave polarisation from TSDW to LSDW. This will be described in more detail in the results and discussion Chapter 8.

6.4 Laboratory tests of the cryostat operation

The early stages of this project were focused on improving and getting to know the setup: operation principle, essential components and basic characteristics. As a main part of laboratory preparation before the setup was mounted for the first time at MID the minimum achievable sample temperature was estimated. This measurements were carried out in the test chamber in sample environment laboratory and also included placing a sample in a magnet bore. Thus, in addition to liquid helium (LHe) cooling of the sample, liquid nitrogen (LN$_2$) was used as coolant for the magnet in order to reduce heat radiation from the coil to the sample.

   To achieve and stabilise operation at low temperatures it is important to minimise the contact with any heat sources to the sample. In this regard, the transfer rod, which is attached to mount the sample in the cryostat, potentially limits the lowest possible achievable temperature. First type of this connection was a grub screw. Therefore, in this case, it was impossible to detach the rod, but additional weight pressure on the connection of the sample with the cryostat improves the thermal contact. In this configuration:
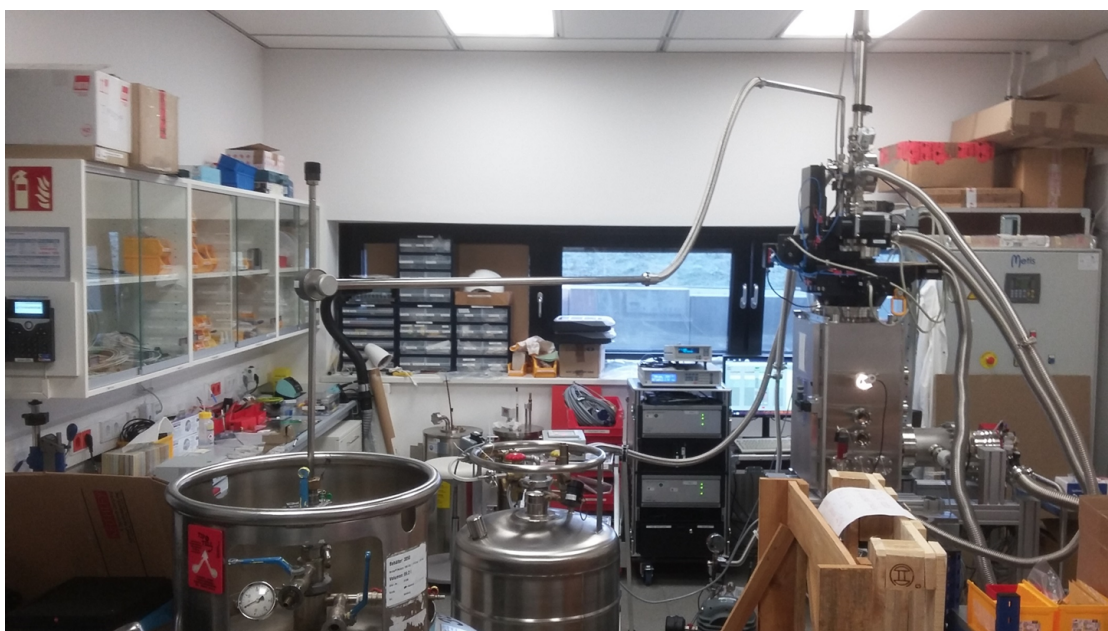
Figure 6.6: Laboratory tests of the cryostat operation

Grub screw connection

Time	Cryostat	Sample
5 min	6 K	32 K
60 min	5 K	20 K

Double thread connection

Time	Cryostat	Sample
5 min	6 K	38 K
60 min	5 K	60 K

Second type of sample stick connection is double thread. Thus, when screwing the sample rod into the cryostat and unscrewing the transfer rod from the sample rod, heat exchange with the rod is prevented. However this solution has a weak thermal connection, which results in an inefficient and unstable cooling. After the first cryostat commissioning third type of connection was developed with detaching possibility and used in all further experiments: combination of screwing sample holder into the cryostat dock and detaching from the transfer rode using banana pins. This concept showed good thermal connection, long-term stability and relatively easy assembly. The one disadvantage of screwing of sample stick into cryostat is mechanical force that can introduce inaccuracy in the reproduction of the angular positions for each newly mounted sample. With this type of sample holder connection the minimum sample temperature is 8 K, which is achieved in about an hour, depending on the cooling rate (1-5 K/min).

7 Experiments at the MID instrument

7.1 PUMA setup experimental protocol

As a first step in the experimental preparation the energy dependence of angular positions for the following Cr and Dy reflections was obtained. In Cr bcc structure with lattice parameter a = 2.88 Å fundamental reflection: Cr(002); the SDW with incommensurability parameter $\delta = 0.045$ Å reciprocal lattice units (r.l.u.) at 180 K is giving rise to two satellites around forbidden fundamental peak Cr(001): SDW(001+δ), SDW(001-δ) and the CDW as a second harmonic of SDW is giving rise to two satellite around allowed fundamental peak, but measurements are carried out only using one of them, due to technical limitations: CDW(002-2δ). In Dy hcp structure with lattice parameters a = 3.593 Å and c = 5.654 Å the measurements are carried out using fundamental reflection Dy(0002). The energy dependence of the angular position for all these reflections is demonstrated on Figure 7.1, the calculations for these plots were made based on theory from chapter 5. Since the analysis of these data is based on comparison of charge and spin waves behaviour, it was crucial to choose conditions, which remain as persistent as possible between different measurements. In addition to make the search for reflections more accurate and efficient, relative movement approach was chosen. This approach consists of moving the detector and the sample by the amount of relative difference in the position of the previously found reflection. Based on this concept and physical limitation of detector wide angle range at MID instrument of $2\theta = 50$ degrees, we chose the photon energy about ~ 10.5 K - 11 keV (depending on machine availability).

Since the first PUMA experiments introduced both a new setup and a new method the simplest possible instrument configuration was chosen, which means that no monochromator or any special focusing optics were used. The devices, which were in operation after undulator, are: XGM, CRL-1, Horizontal offset mirrors, different combination of attenuator sets and imagers, diamond detector in the diagnostic end station (DES). The XGM was used for monitoring the radiation intensity incident on the sample, for later experiments the option of using diamond detector placed in the MPC was also implemented for better accuracy.

From the first PUMA commissioning time to the current state of the experiment, a number of weak points were identified and improved.
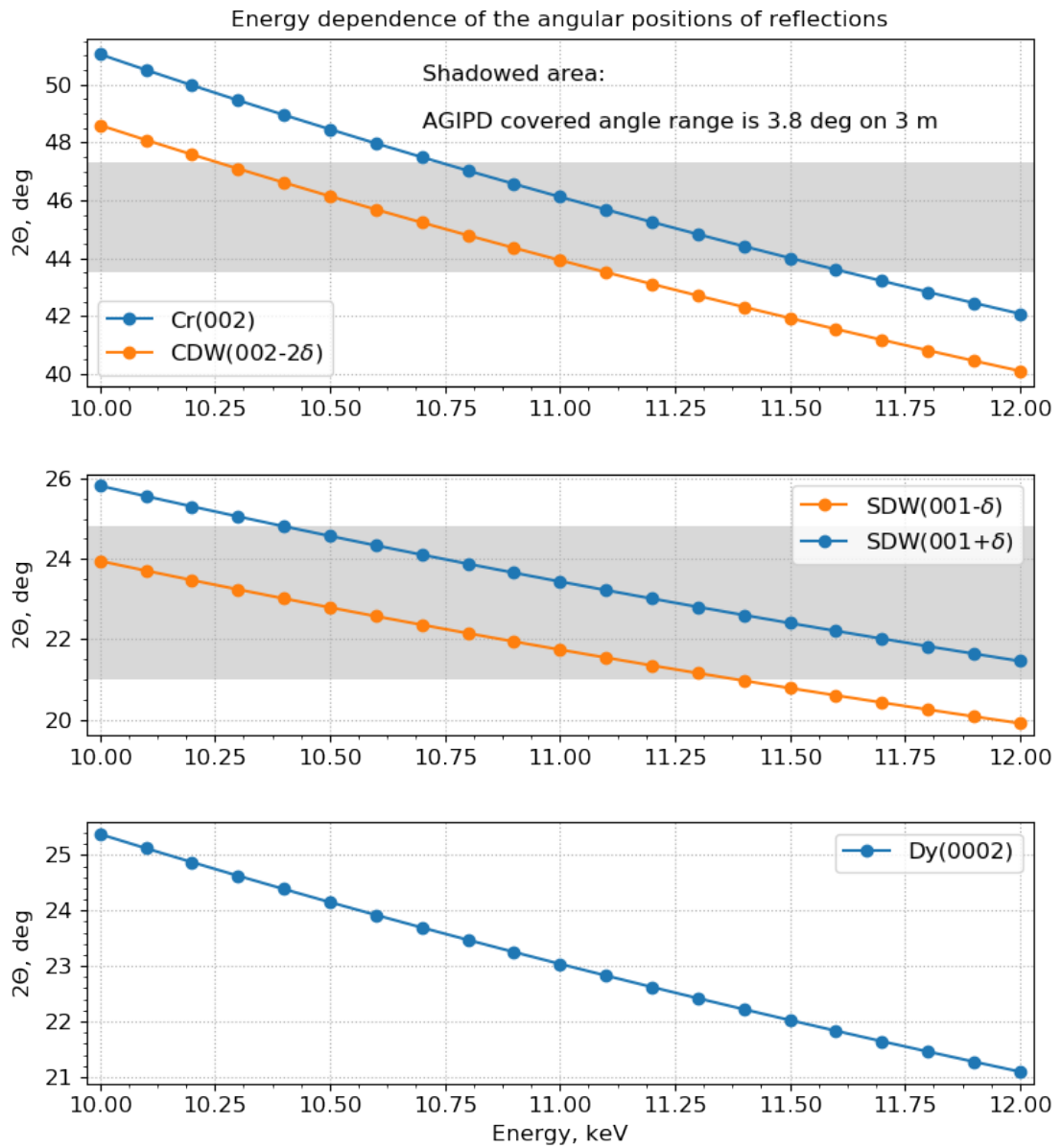
Figure 7.1: The dependence of the angular position for reflections: Cr(002) and CDW(002-2δ); SDW(001-δ) and SDW(001+δ); Dy(0002). The shadowed area (in gray) denotes field of view of AGIPD, which is calculated as two times arc tangent of the ratio of half detector width 0.1 m to distance sample - detector distance of 3 meters ($2 \cdot \arctan(\frac{0.1}{3}) = 3.8$ deg).

Unexpected limiting factor for the first commissioning period was that AGIPD detector was not yet in operation. Thus as a detector was used fluorescent screen with Basler camera pointed on it. Now the search for intense Bragg peaks is facilitated by the use of a fluorescent screen. It provides the bigger field of view due to opportunity to put fluorescent screen closer than any other detector as well as prevent from accidental damage of the detector with strong reflection. Another crucial factor for reflection search and measurements was, that big rotation motor of manipulator (for sample rotation) has difference of 0.3 degree between counter and clockwise directions. To solve this we installed an optical encoder, which increases the accuracy and reproducibility of the rotation motor position. Since the rotation range is about 180 deg, it is useful to align sample before placing it in the loadlock, otherwise it is not possible to match $\theta - 2\theta$ calculated positions with sample - detector angular positions. In this regard, for the symmetric Bragg reflection geometry the sample reflecting planes need to face the detector side.

We find it important to mention here the main issues connected with commissioning of the new setup, since these problems had a great influence on preparation and conducting of each experiment.

During this project, the PUMA setup was continuously improved to solve problems that affected the experiment performance. Here we describe the main changes along with the reasons that led to them.

The first one was already mentioned in setup description section, it concerns sample stick precession around the center of rotation. This problem has several crucial affects: alignment becomes very time consuming and imprecise, the rocking curves have increased width since the beam is travelling over the sample surface and the sample stick has big risk of breakage while moving inside of the magnet. As a first attempt to solve this issue we installed manual tilting stages both for the transfer rod and the cryostat to adjust the vertical position of the sample in the center of rotation. Another parameter affecting the position of the sample is the cooling transfer tube. The syphon exerts a lateral mechanical force on the cryostat due to its own weight. That is why it is useful to insert cooling connections before sample alignment also for every new sample during the experiment. In addition for the last beamtimes we installed on the manipulator flexible syphon holder, it decreases the weight load on cryostat, but leaves the rotational movement unlimited.

A next big step in the implementation of any new setup is the evaluation of safety requirements and fulfillment of all regulations. In our case, the main concern was the high magnetic fields produced and the high voltage in the experimental hutch. It has two aspects: prevention of short-circuits for fire protection purposes and personal protection, to prevent operation by staff without special electrical training. Hence, while the capacitor bank was located in the experimental hutch, which is not considered as a fire protected area, due to a risk evaluation the magnet

operation was limited to maximum of 5 T, because of a voltage limitation of 1000 V. After one year the capacitor bank was installed in the rack room, which is located above the experimental hutch and built as a fire protected room. This relocation required manufacturing of new and longer cables and tests of whether the extended length affected the signal synchronisation and timing as well as the: duration, strength and shape of the magnetic pulse. The PUMA setup is not permanently installed at the MID instrument, but it would be time consuming to transport the capacitor bank between the lab and the MID rack room. For this reason, a new capacitor bank was ordered and customised with safety relay connectors for voltage and temperature sensors. These relays are eliminating the risk that a magnet short circuit would affect other devices by disconnecting them from the network at the time of discharge. After fixing the position of this device and following several inspections an efficient grounding scheme was developed and implemented by MID's electrical engineer. Finally, to disable the discharge option during manipulations with wires and magnet in the experimental hutch (personal safety) the capacitor bank was connected with the interlock of the experimental hutch door.

Synchronisation of the capacitor bank discharge with the X-ray pulses was a crucial task for the PUMA setup implementation. The safe charge-discharge cycle rate for a commercial Metis capacitor bank device is less than 10 Hz, so it was necessary to prevent each pulse train from being used as a trigger for discharge. During early operation of the setup the question about length and type of input trigger signal was unclear. Thus, the first option for a discharge trigger was to use X-ray train on demand (TOD) . TOD is an operation regime, where no pulse trains are sent to the instrument, unless an OK signal is given (zero pulses as default). In our case we used the TOD mode with only one train, the beginning of which was assigned as trigger for a magnetic discharge, but the number of pulses within this train can be varied. The prohibition of having X-ray beam immediately before and after the single train delivered in TOD mode prevented the capacitor bank from starting another charge-discharge cycle. However, in such an operation mode useful information about sample scattering before and after the magnetic discharge is not accessible. This problem persisted for a long time despite different signal stretching, XFEL hardware updates and Karabo software developments. Finally, after discussion of this issue with the Metis company a firmware update was identified, which provided the solution to: not interpret every train arriving at 10 Hz rate as the beginning of a charge-discharge cycle, thus preventing multiple discharges with one trigger.

The last major issue to mention here, which appeared during several experiments and has still not been solved, is a vacuum leak in the magnet chamber. This problem could be solved by venting the sample chamber, tightening the magnet bore screws, pumping chamber down again and cooling the magnet, which took a significant amount of time. The first assumption is that a big temperature jump after magnet discharge cause loosening of the magnet bore screws. Thus,

the current PUMA setup operation procedure includes the keeping the magnet cold at all times during the entire period of the experiment. Unfortunately, during the last operation vacuum leak appeared again during high magnetic field operation a despite cooling of the magnet so this issue remains under investigations.

Along with the setup implementation, a standard procedure for the most frequently performed measurements was also developed.

Temperature measurements: Make a rocking curve scan to find the angular position where the reflection is the most intense. Optimise its position on the detector in such a way that the movement of the peak across the AGIPD detector due to temperature changes does not go beyond the physical limits of the detector module. This will prevent intensity losses in the gaps between the modules and is helpful for further comparative data analysis. Then several options for data collection are possible: continuous data acquisition during sample cooling (valid only for very small temperature step, due to thermal change of the cryostat and sample material, at large steps it is necessary to optimize the position on the rocking curve), waiting for stabilising on each chosen temperature and repeat the rocking curve measurement while collecting data. In the last experiment we considered also to check the sample position in height for each temperature because of the slight thermal deformation of cryostat material. During the laboratory test upon cooling from 300 K to 80 K the contraction of the cryostat length was estimated at about 1 mm. Taking into account the sample size (on our case 5 mm), presence of domains and defects, the big steps in sample height adjustment should be avoided.

Magnetic measurements: Every magnet operation as a standard pump-probe experiment starts by checking the synchronisation , i.e. the trigger and timing and overlap of the pump (B field) and the probe (X-ray train). The diamond detector, which is located either in the sample chamber or diagnostic end-station (DES), provides precise temporal characterization of the X-ray pulse arrival. The timing triggers for all devices connected within each other and depends on X-ray beam timing, it is set in units called clock, 1 clock = 9.23 ns. The fixed clock value corresponds to the moment of X-ray beam interaction with sample. Thus, it is necessary to choose the trigger for discharge relative to this clock value, taking into account the response time (delay from the moment of X-ray interaction with the sample). To check temporal overlap of X-ray beam and magnetic field we perform single discharge with small power of magnet field, while sample is out of magnet. Using simple python code both time dependencies for X-ray (measured with diamond detector in DES) and magnetic pulses (measured with FastADC) are plotted in one axis. The optimal trigger delay value for discharge corresponds to the coincidence of the magnetic field maximum with X-ray beam detection. In addition this procedure is needed to match the setting voltage values for the capacitor bank to obtain the desired magnetic field strength. Thus, when magnet preparation is finished, for the chosen temperature value the magnetic scan as a

sequence of several discharges on static position of the sample can be made manually or using the pulse sequence option in the Karabo control system that has been developed. One run of data acquisition contains several discharges with the same magnetic field power and the same value for triggering signal of the capacitor bank. No readjustment was made between data collecting runs with voltage or trigger steps.

In addition the static measurements using the thin Cr samples, i.e without any additional kind of pump (no magnetic field, no temperature change) or motors movement, are useful to estimate sample heating and radiation damage imposed by the intense X-ray beam of an XFEL. In this case data acquisition is carried out with varying X-ray exposure time, transmission, and number of pulses per train.

7.2 Dy measurements

A Dy single-crystal was mounted in the cryostat and cooled to 160 K while inserted into the split-coil magnet. The symmetric (0002) Bragg reflection ($\mathbf{Q}$ along the c-axis) was tracked in horizontal scattering geometry by using AGIPD during a series of magnetic discharges ($\mathbf{H} \perp$ c-axis) with varying amplitudes and a pulse duration of 1 ms. The fundamental Dy(0002) reflection in hcp crystal structure with a = 3.593 Å and c = 5.654 Å was found for 11 keV around $2\theta \simeq 23.04$ deg and $\theta \simeq 11.52$ deg angles. During the first attempt to measure the effect of magnetic field at low temperatures on fundamental Dy reflection, the sample was glued to the holder using GE varnish. It is traditionally used for thermal fixation at cryogenic temperatures and can be easily dissolved in ethanol, which is harmless for the sample. However, with applied magnetic field of 2 T, the sample was detached from the holder presumably because the ferromagnetic state was reached. Thus, for the next experiments samples were fixed using Stycast epoxy. For next experiment two temperatures were chosen to observe the helix to "fan I" transition at 150 K and the helix to "fan II" transition at 170 K. The sample was cooled down so that fluctuations of the temperature stabilise around 0.1 K and series of magnetic scans were carried out with a voltage discharge ranging from 300 V to 405 V with steps of 15 V (0.6 T to 1.6 T). On a final stage the full range of temperatures were chosen from 185 K down to 80 K with the same stabilisation, on each temperature we carried out rocking scan to check the alignment of the sample and series of magnetic discharges with voltage discharges from 100 V up to 550 V with steps of 30 V (0.5 T to 2.25 T, with updated capacitor bank software and new split-coil). In additional for several temperatures we tested magnetic scans with changing the trigger value and keep voltage the same. As we mentioned above optimal trigger delay for the discharge of the capacitor bank corresponds to the coincidence of the magnetic field maximum and X-ray beam with sample interaction. However, in case of tracking sample dynamics in various moments of

magnetic field, we have an option to change the trigger delay relatively with step of 9.23 ns (1 clock). For one of the tests the delay values were varied in the range from 6305182 clock till 6280182 clock with step of 2500 clock. However no protocol for delay variation was confirmed yet, range and step selection should be improved to fit fast sample dynamics.

7.3 Cr measurements

The Cr measurements were carried out using different type of samples, we will describe the measurement parameters using the example of Cr(100) since in other cases they were similar. In Cr bcc structure with lattice parameter a = 2.88 Å the fundamental Cr(002) reflection was found for 11 keV around $2\theta \simeq 46.12$ deg and $\theta \simeq 23.06$ deg angles. After that, the sample is cooled down to 180 K and with the relative movement of the detector and the PUMA rotation motor was found CDW(002-2δ) around $2\theta \simeq 43.93$ deg and $\theta \simeq 21.97$ deg. This position relative to the fundamental Cr(002) reflection corresponds to the incommensurability parameter $\delta = 0.045$ Å at 180 K. Here we carry out temperature measurements in the range from 300 K down to 50 K with steps of 50 K, later in smaller range, but covering the transition temperature of 123 K. At the temperature above spin-flip transition the CDW peak was optimised again and magnetic measurements were carried out with voltages from 300 V up to 3000 V ($\sim$ from 0.5 T to 12 T, may vary for different split-coil), then the same procedure was repeated for the temperatures below the transition. After all measurements carried out using CDW(002-2δ) reflection, sample temperature was maintained around 180 K, while detector and manipulator rotation motor (sample rotation) were relatively moved to find SDW reflations. The SDW(001-δ) peaks was found around $2\theta \simeq 21.74$ deg and $\theta \simeq 10.87$ deg angles. To find the second satellite, which is symmetrical around forbidden Cr(001) Bragg peak, we measured the rocking curve with relative θ change at least $\pm$ 1 deg. Thus, a reflection SDW(001+δ) was found that was separated from the first by an angle $\Delta 2\theta \simeq 1.7$ deg and $\Delta\theta \simeq 0.85$ deg. Since the idea behind these measurements is a comparison of the behavior of magnetic and charge reflections, it was necessary to repeat the procedure. However, for the temperature dependent measurement a smaller range of temperature values from 140 K to 80 K was chosen, but with a smaller step size of 10 K and a wider rocking scan range. The measurements were repeated several times at each set-point, since these reflection has significantly lower intensity. For the magnetic measurements, we also chose the same temperature positions and magnetic range and tracked each SDW satellites separately. In addition to comparative measurements, tracking of one of the SDW reflections was done during warming up of the sample from room temperature up to 340 K with steps of 10 K, in order to cross the Neel transition.

8 Results and discussion

8.1 Data treatment

Despite the different phenomena we are investigating for dysprosium and chromium, there is a significant overlap in the measurement procedure and this also applies to the initial steps of data analysis.

The first step in working with AGIPD detector data was converting the analog-to-digital units (a.d.u.) into photons (photonisation) after dark (no X-rays) image subtraction (background corrections). To do this, we build a histogram of the distribution of all pixels by a.d.u values, thus the position of the most intense first peak in the histogram corresponds to one photon, the next peak indicates two photon events and so on. Applying this correspondence at the beginning for each data set improves the signal-to-noise ratio and "bad" pixels with too low or too high values are ignored. The shape and size of all observed reflections fit on one AGIPD module, including their change under the influence of temperature and magnetic field. This allows us to speed up data processing by analysing only one selected module instead of all 16. In addition, the insensitive areas between modules and quadrants of the detector can be ignored. A remaining issue is the influence from the area between two ASICs (Application Specific Integrated Circuits), where counts are doubled (due to the double pixel size) and the values in the corresponding pixels need to be halved. The next crucial filtering step is to choose the right X-ray pulse trains for the analysis depending on the measurement type. As it was mentioned in the previous chapter the data analysis is based on the three different standard measurement procedures that usually are applied:

1. a rocking curve scan at a given temperature for which we select trains corresponding to a change in the position of the motor θ from minimum to maximum;

2. for magnetic scanning at a given magnetic field, we select the trains that occur during the discharge and variable number (depending on statistical distribution) of trains before and after (Figure 8.2);

3. for statistical measurements (i.e. with zero magnetic field and without changing the tem-

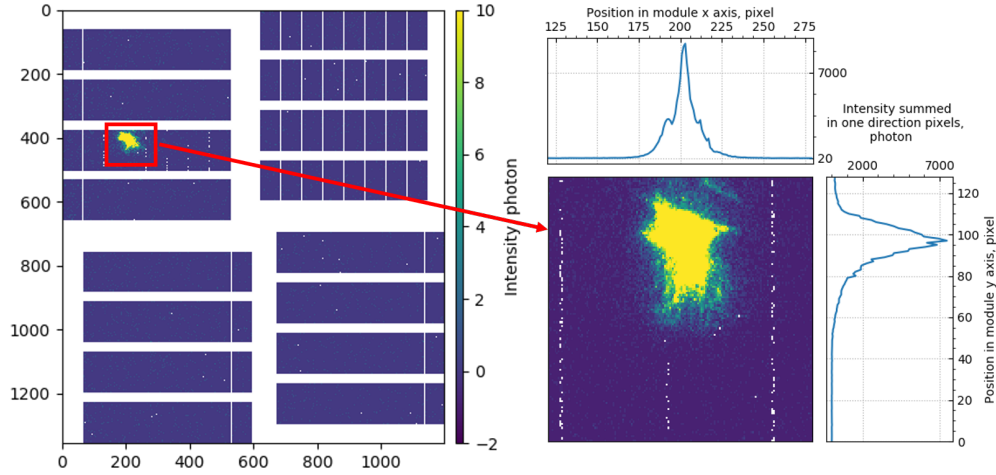perature) we select either all trains, or amount of trains enough to show the radiation effect.

Figure 8.1: Full AGIPD view with all 16 modules after background corrections and photonisation, one of which contains the Dy(0002) reflection. On the right side: region of interest(ROI) around Dy(0002) on AGIPD; beam profile in y, obtained by summing photons over x axis (horizintal); beam profile in x, obtained by summing photons over y axis (vertical).

The data acquisition (DAQ) system at European XFEL assigns a TrainID number to the data which acts as a time stamp and allows to synchronize and compare data from different devices; however, it is important to check that there is no missing stamp (happened often in the early versions of the DAQ) and that it is properly aligned for all data sources used in the analysis. Finally, to describe the shape and position of the peak, it is convenient to work with 1D profiles along the x and y axes, obtained by integration over pixel rows and columns, respectively (Figure 8.1).

To avoid multiple repetitions of basic data analysis algorithms, we describe here two standard algorithms for this project.

The first algorithm consists of plotting the rocking curve and the temperature dependence of the integrated intensity. The intensity for each motor step θ is calculated as a sum of the values of all pixels in the region of interest (ROI) and normalised on the values from the source, which was used in the particular experiment as incident intensity monitor. In case of Dy(0002) and Cr CDW measurements, as the incident intensity source, the XGM was chosen. In case of Cr SDW measurements, the fluorescent signal on the module closest to the module containing the reflection acted as an indicator of the incident radiation. If there are several intensity values
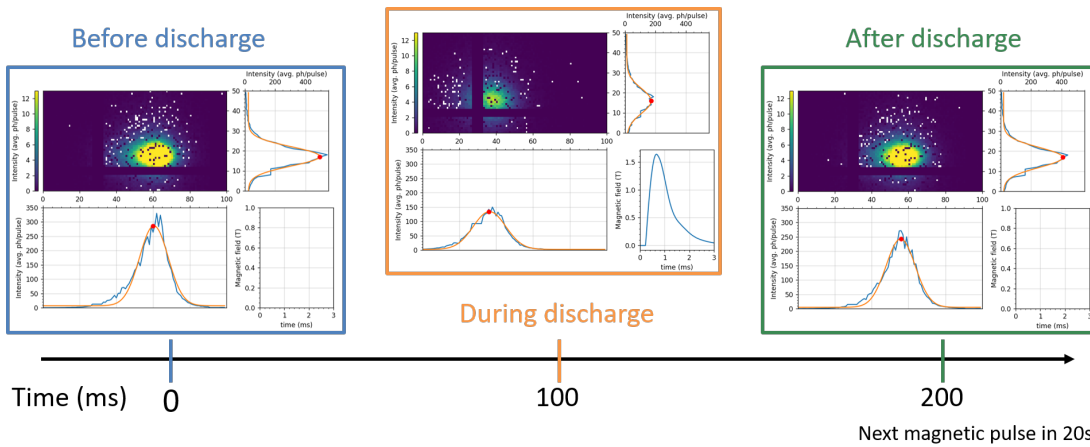
Figure 8.2: Timing scheme of magnetic measurements using the PUMA setup. The three boxes demonstrate three EuXFEL trains consisting of one X-ray pulse: train containing the discharge of the capacitor bank and hence the magnetic pulse (middle, orange), the last train before discharge (left, blue) and the first train after discharge (right, green), both without magnetic pulse. In each box: ROI of Dy(0002) on AGIPD; beam profiles along x and y; magnetic pulse curve B as a function of time for train with discharge. Beam profiles have Gaussian fit curves (orange) and center position marked (in red).

for unique motor value the mean of these intensity values is taken. Finally, the temperature dependence consists of the rocking curve integral (integrated intensity) in accordance with the temperature value from the cryostat sensor.

The second algorithm consists of plotting magnetic or temperature dependencies of the crystal lattice constant. Since an angular encoder for the two theta motion was not yet implemented for the current project, the procedure to convert the physical peak position on the detector into the Bragg angle position was needed. The reflection peak profile along the x-axis, which was mentioned above, is calculated in the angular position of the sample θ corresponding to the maximum of the rocking curve. From a simple fit of this profile with the Gaussian model, the position of the reflection on the detector in mm units is obtained. Thus equation for the double Bragg angle for each temperature measurements:

$$2\theta_{\text{Bragg theory}} \pm \Delta\theta = 2\theta_{\text{Bragg theory}} \pm \arctan\left(\frac{\text{start position - current position}}{\text{sample detector distance}}\right) \tag{8.1}$$

This approach assumes that the first temperature point corresponds to the theoretically predicted Bragg angle for the given conditions and the starting position is equal to the current

position, thus $\arctan 0° = 0$. Substituting the obtained angular values into the equation for the Bragg law, we obtain dependencies for the lattice constant.

8.2 Dy results and discussion

The magnetic phase transitions in bulk Dy are accompanied by a series of structural transitions [62]. The coupling between the magnetic and structural transitions is stronger or weaker depending, for instance, on the temperature. In zero magnetic field bulk Dy has a Neel temperature of T_N = 179 K below which it shows an incommensurate helical AFM structure. Upon further cooling, below the Curie temperature at T_N = 91.5 K, it becomes ferromagnetic. Within the AFM region (91.5 - 179 K) the spin rotation angle per layer is temperature dependent and decreases from 44 ° upon cooling. In a non-zero magnetic field applied along the easy-magnetisation direction **a**, various intermediate magnetic structures presumably have been observed that deviate from the simple helix, but no consensus has been reached. Different versions of the magnetic phase diagram for Dy includes a spin-flop phase, a vortex phase, and possibly a new phase [63–65]. In these experiments, we focus on the structural Dy(0002) Bragg reflection and the response to an applied H-field up to 2.2 T as a function of temperature in the AFM phase. The applied field triggers an ultrafast perturbation of spins that distort the helix structure, which in turn leads to a structural distortion and phase transition through magnetostriction [66].

As a first step, the Dy(0002) reflection has been observed at various temperatures in the helix phase by measuring the rocking curve for each temperature value in the range of 125 - 165 K (Figure 8.3). The temperature dependence of the integrated intensity shows a slight increase of about 7% with cooling. The slight change in intensity can be explained as a Debye - Waller effect, which shows that the elastic Bragg scattering is increased in intensity by mean-squared displacement decrease with cooling down.

Also instead of normal thermal contraction we see the increase in lattice constant with temperature decrease due to positive magnetostriction. In case of Dy, a linear magnetic lattice change is described by Kittels theory of exchange inversion due to magnetic exchange forces [49]. Measurement carried out on PUMA setup are in good agreement both with the measurements made in one of the early articles and theory [62].

Starting at 179 K the magnetostriction is observed along with the temperature decrease till 86 K [69], where magnetic transition takes place and the crystal structure changes from hexagonal to orthorhombic lattice (first-order transition). However, under the influence of an external magnetic field this transition appears in higher temperature as shown in Figure 8.4a. This phase diagram predicts two different fan structures between the antiferromagnetic and the ferromag-
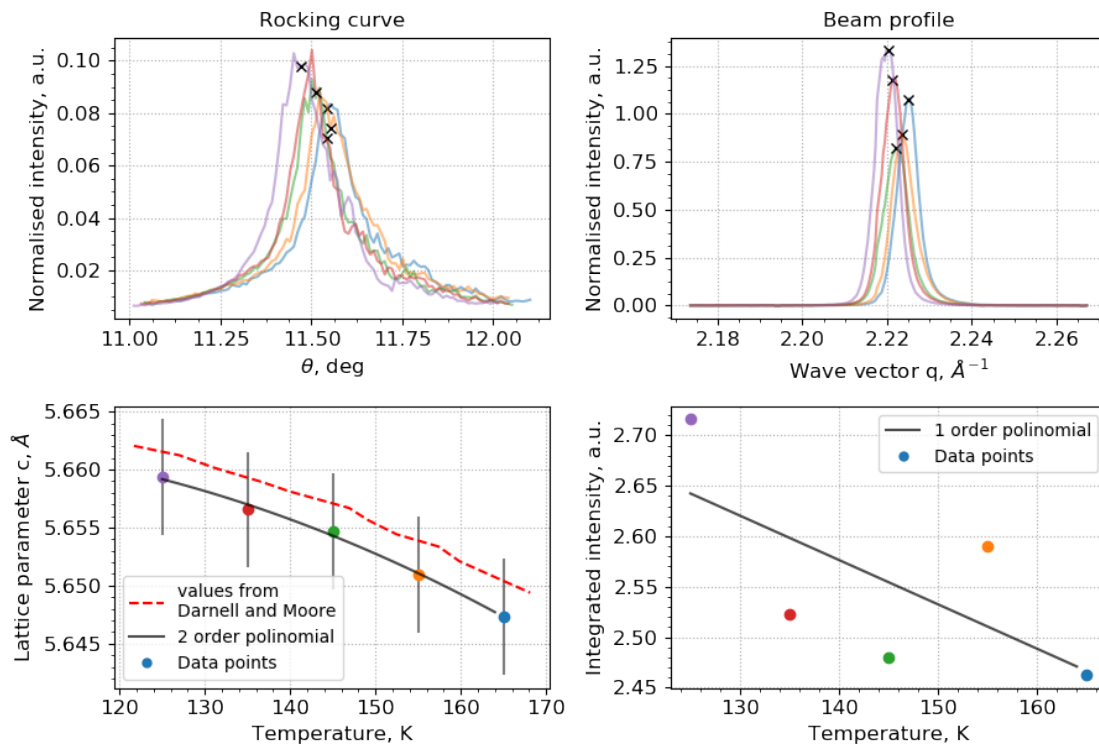
Figure 8.3: For Dy(0002) reflection: Rocking curves for, each color corresponds to different temperature and cross mark in the center of the peak (left, up). Beam profile at the angular position corresponding to the center of rocking curve, here cross mark corresponds to the center of peak profile curve (right, up). The temperature dependence of lattice parameter calculated from center position of beam profile. The black line shows fit of experimental points. The red dotted line shows values previously reported in the literature (left, bottom) [67]. The temperature dependence of integrated intensity of presented rocking curves (right, bottom).
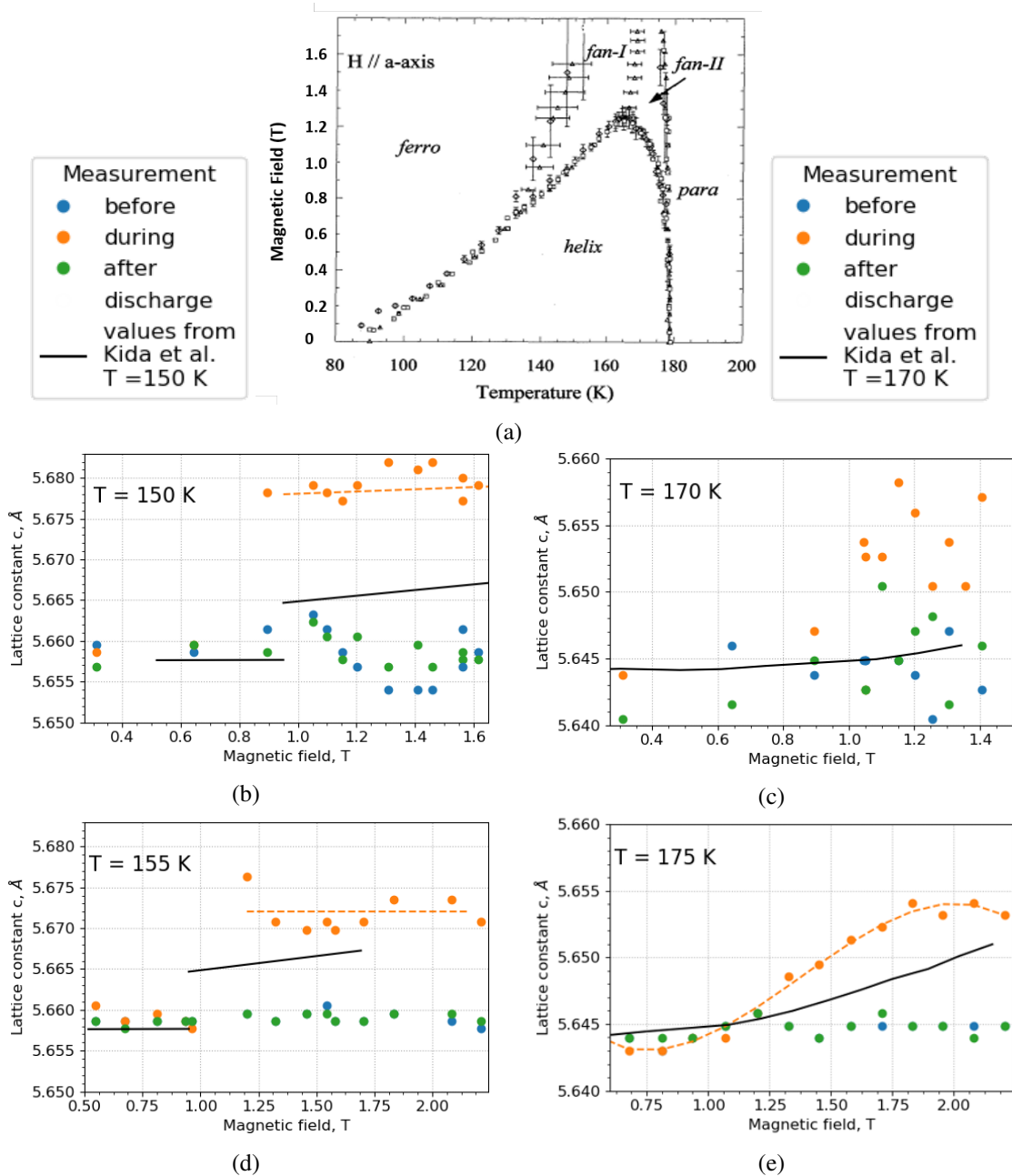
Figure 8.4: (a) The magnetic phase diagram determined by specific heat measurements in [68]. The magnetic field dependence of the *c* lattice parameter obtained by the Dy(0002) reflection at temperature: (b) 150 K (c) 170 K (d) 155 K (e) 175 K. The colored dots on the plot represent measured lattice constant values: (orange) sample in magnetic field, sample state before (blue) interaction with magnetic field and after (green). The black solid line shows experimental values from the article [66].

netic states in a magnetic field stronger than 1 T. To study the difference between these two transitions for the first experiment two temperature values were chosen: 150 K and 170 K.

As we mentioned above the origin of the helical spin structure lies in the strong positive nearest-layer exchange interaction ($J_1 > 0$) and a weak negative next-nearest-layer interaction ($J_2 < 0$). The characteristic angle between spins in neighboring layer is defined from $cos\theta = \frac{J_1}{4J_2}$. In the presence of an external field B applied in the basal plane the total energy is:

$$E = -M^2 \sum_p \{J_1 \cos(\theta_p - \theta_{p-1}) + J_2 \cos(\theta_p - \theta_{p-2})\} - MB \sum_p \cos(\theta_p) \qquad (8.2)$$

where, θ_p is the angle between the moment in the plane p and the field B. In the case of a fields applied perpendicular to the axis of the helix, this angle $\theta(z)$ is a function of the coordinate z on the c-axis [70]. Exchange magnetostriction occur as J_1 and J_2 are functions of distance between two atoms. Thus, the strain along the c-axis can be calculated from minimising the exchange energy of magnetostriction [71].

The lattice constant at 150 K shows a significant change already at a field of 0.9 T (Figure 8.4b). Such an abrupt structural change at 150 K starting around 0.9 T is in good agreement with earlier investigations [66]. This first-order phase transition corresponds to the transformation from helical antiferromagnetic ordering to the fan structure, which is marked on phase diagram as "fan I". The same dependence at 170 K shows a smooth change of the lattice constant starting from 1.05 T with full recovery before and after discharge (Figure 8.4c). Thus, at 170 K with fields above 1 T Dy undergoes a second-order phase transition, which is characterized by a smooth change from helical antiferromagnetic ordering to the fan structure, which is marked on phase diagram as "fan II".

Her the fan structure is a state, when fraction of spins are aligned along direction about 60 deg away from the external field direction. In a previous research it is shown that moments have a tendency toward aligning perpendicular to an applied field [72]. And two different types of this fan structure "fan I" and "fan II" on the phase diagram denote different types of phase transitions.

In order to study the difference between these transitions we repeated this experiment by expanding the region of temperatures and magnetic field values. It is important to note that all experiments were carried out in parallel with the development of the installation and the improvement of the measurement protocol. On the Figure 8.4d,e we show magnetic field dependency for lattice constant with temperature values 155 K and 175 K. At 155 K the jump in values is reproduced and has a better agreement with values from the same article for 150 K. Also the transition appears in slightly higher magnetic field around 1.2 T, which also corresponds to the phase diagram. The curve of lattice constant change at 175 K has a clearly visible slope characteristic of the second-order phase transition, that matches to the phase diagram. At 170 K we can

be too close to the boundary of two different transitions, which can lead to less pronounced trend for the lattice constant dependence of magnetic field than expected from the previous studies.

Finally, the Figure 8.5 shows the Dy crystal lattice parameter change in the temperature range from 125 K till 175 K to cover both "fan I" and "fan II" regions of phase diagram. Accordingly, the range of magnetic fields was chosen from the minimum B = 1.25 T required for the transition boundary at 125 K up to B = 2.25 T to also cross the antiferromagnetic to ferromagnetic transition. As the temperature decreases, the curves start from higher values; this once again demonstrates the effect of magnetostriction shown in the previous graphs. The increase in the curves slope shows the transition from the first to the second order phase transition, which moves to the lower magnetic values with cooling. In the magnetic range covering the ferromagnetic state, the lattice parameter remains constant, provided that the sample is securely attached to the holder.

Previous studies came to the conclusion that there is not intermediate state between helical and fan structure in Dy unlike the case of Holmium, which has a similar magnetic structure and temperature characteristics. The mean-field calculations [72] showed the free energy of the helifan phase is always greater than the free energy of the helix or fan phases. However, in the recent study [64] the "fan I" region is described as the co-existence of two structures fan and helix and the new intermediate state is added, which defined as short-range order fan located between ferromagnet state and fan (which is called long-range order fan).

To describe beam profiles during for all Dy(0002) reflection data we used Skewed Voigt model, which is defined as the probability distribution given by a convolution of a Lorentz distribution and a Gaussian distribution with allowing of non-zero skewness. It was noticed that for some values of the magnetic field, instead of changing position and maintaining the shape, the profile changes both: shape and position. Thus for last part of analysis we made the assumption, that during the increase of magnetic field the peak is splitting in two peaks. This approach corresponds to the proposal from [64] that two structures (helical and fan) co-exist. Depending on temperature and magnetic field we can see three states: right peak (only green curve), left peak (only red curve), double structure peak (demonstrated in figure 8.7 for three different B fields). Several restrictions were implemented during the fitting procedure for double skewered Voigt model: the shape of the peak is defined from the peak shape in the zero field, switching between left and right positions is forbidden (the right peak can not have a lower position value than the left one). Earlier studies ([66]) also mention such double peak mechanism of the transition region with further change in position while maintaining the single peak shape. Based on the results of fit within the framework of the double peak model, we calculated the magnetic field dependence of Q wave vectors for left and right peak Figure 8.8. We assume that left peak corresponds to the helix structure, which is present in low magnetic field and disappear above
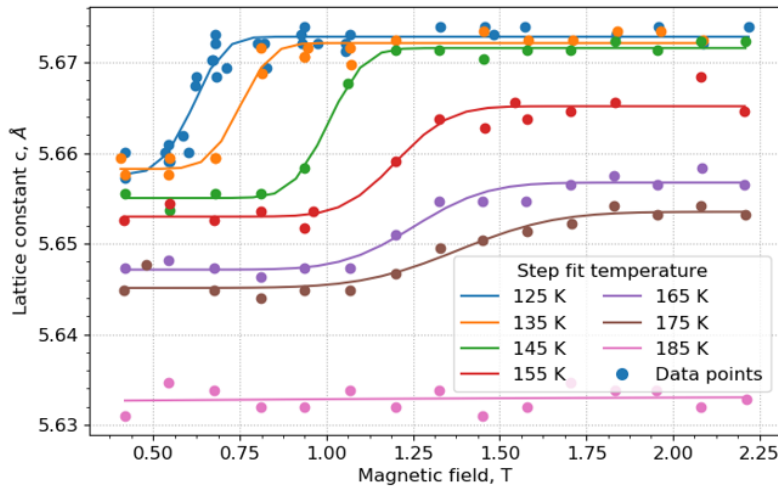
Figure 8.5: The magnetic field dependence of lattice constant obtained by the Dy(0002) reflection. Different colors represent different sample temperature in a range from 185 K down to 125 K. The dots indicate experimental data and the solid line - step function fit.

1.5 T. Then the right peak corresponds to the fan structure, which appears in magnetic field from 0.75 T and remains as a single peak above 1.5 T with slight decrease of the wave vector with magnetic field increase. Here we plot the values of the wave vector with the condition that the amplitude of the peak is nonzero. On Figure 8.9 we show magnetic field dependence for left and right peak amplitudes for different temperatures. At 185 K the sample is in paramagnetic state and only right peak appears in whole range of B fields. During sample cooling the transition from left to right peak moves into lower magnetic power, this trend agrees with phase diagram. Finally, we use step function to analyse the interface of peaks amplitudes switch obtained from double peak model fit, and build the resulting phase diagram. The phase diagram is based on values for starting point of each slope and slop duration, which corresponds to area of coexistence of two structures (area, which marked "fan I" on phase diagram at Figure 8.4a).
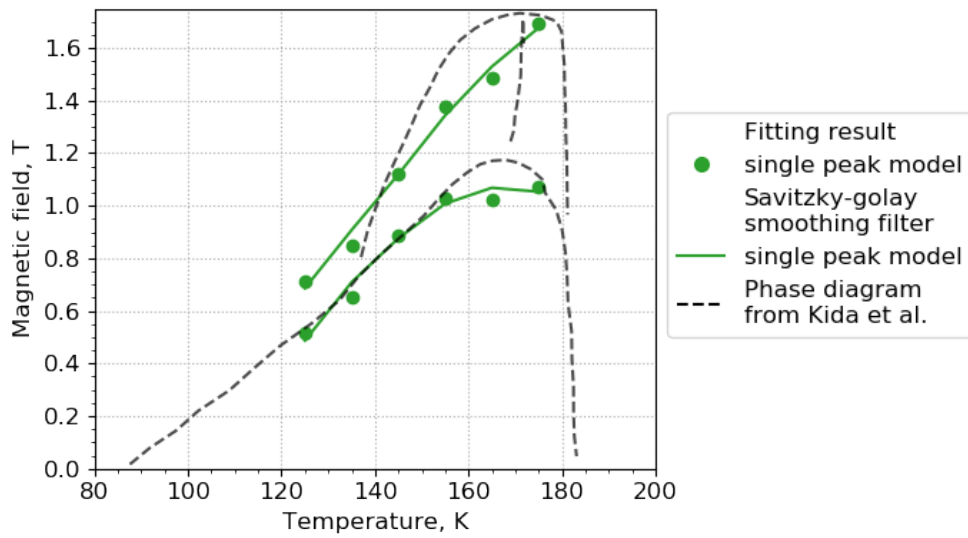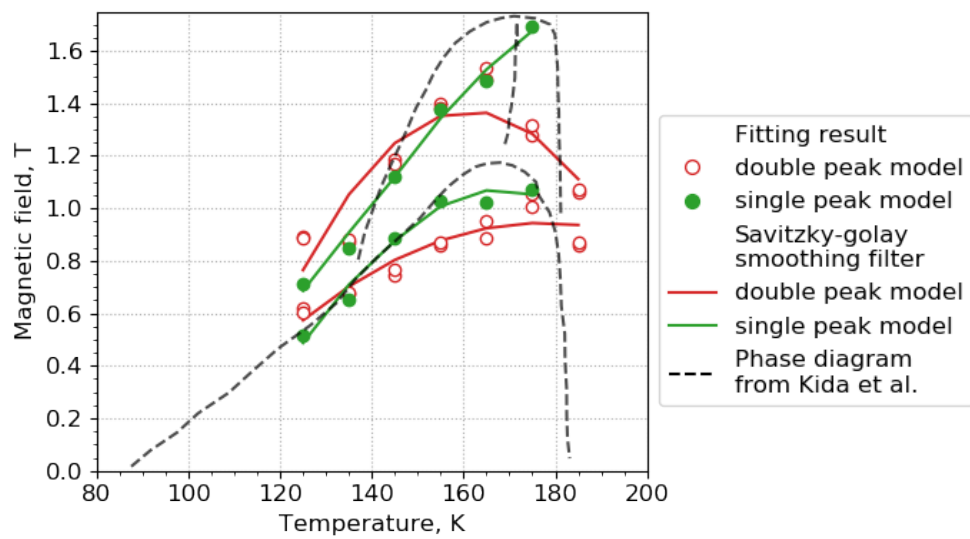
Figure 8.6: The dotted line indicates the magnetic phase diagram determined by specific heat measurements from [68]. The green dots indicates the results of step function fit of the magnetic field dependence of lattice constant obtained by the Dy(0002) reflection. The green solid line is a result of savizky-golay smoothing filter of fitting results.
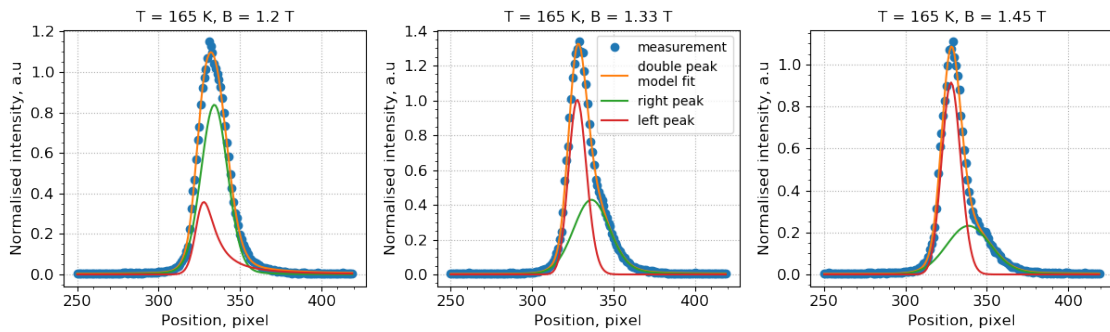
Figure 8.7: Three normalised intensity Dy(0002) reflection profiles in x-axis (horizontal), measured at 165 K at different magnetic fields B = 1.2 T, 1.33 T and 1.45 T respectively. Blue dots indicate experimental data, orange curve - double Skewed Voigt model fit, red and green curves - the first and second Skewed Voigt peaks with fixed center position in smaller and bigger pixels values respectively.
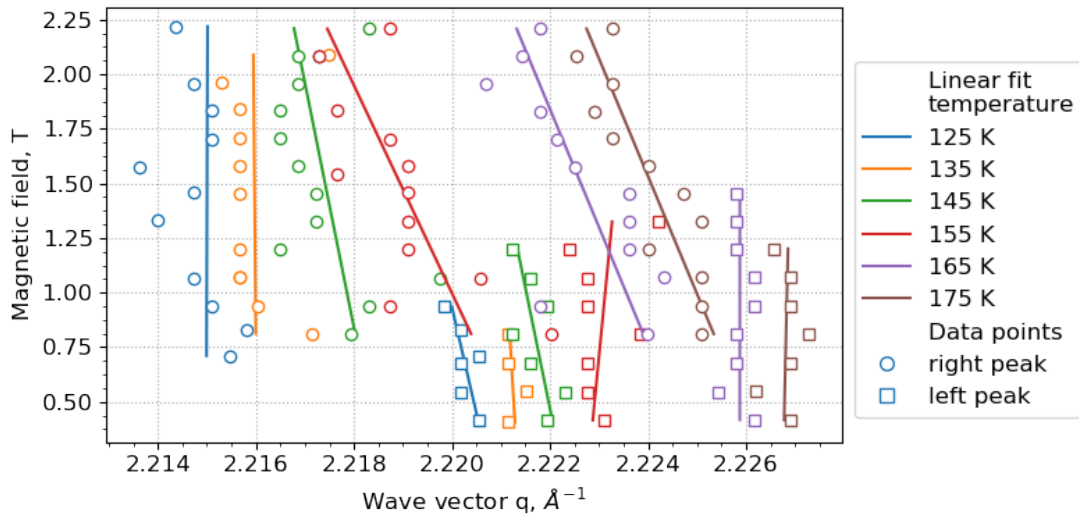
Figure 8.8: The magnetic field dependence of Q wave vectors for left and right obtained by the Dy(0002) reflection fit using Skewed Voigt model. Different colors represent different sample temperature in a range from 175 K down to 125 K. The dots and the squares indicate amplitude values from left right peaks fit of experimental data respectively. The solid line is the first degree polynomial fit.
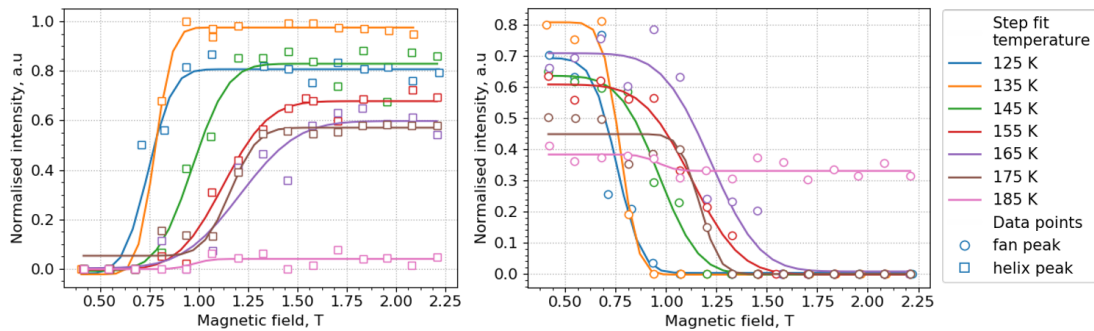
Figure 8.9: The magnetic field dependence of left and right Skewed Voigt peaks integrated intensity obtained by the Dy(0002) reflection fit. Different colors represent different sample temperature in a range from 185 K down to 125 K. The dots indicate amplitude values from fit of experimental data and the solid line is a step function fit.

Figure 8.10: The dotted line indicates the magnetic phase diagram determined by specific heat measurements from [68]. The red dots indicates the results of step function fit of the magnetic field dependence of integrated intensity of left and right peaks obtained by the Dy(0002) reflection. The red solid line is a result of savizky-golay smoothing filter of fitting results.

8.3 Cr results and discussion

Cr is a transition metal with a body-centered-cubic (bcc) crystal structure. Below the Neel temperature T_N = 311 K it organises as an antiferromagnetic structure made of coexisting charge and spin density waves (CDW and SDW). In the case of a commensurate antiferromagnetic structure, the magnetic moments at the corners of the bcc unit cell are opposite to the one in the center. A pure Cr exhibits incommensurate SDW with the lattice period, where the magnitude of the spins varies in a periodic fashion. The period of the SDW modulation is about 27 lattice constants at T_N [73], thus the length of the modulation wave vector is $\mathbf{Q} = 2\pi\delta/a$, where $a = 2.88$ Å (Figure 8.11). These magnetic moments can be oriented parallel to any of the main crystallographic axes, thus three different wave vectors are expected to coexist and giving a rise to six satellites. Between 311 K and 122 K the SDW is transverse (TSDW), where the spin modulation is perpendicular to the modulation wave vector $\mathbf{Q}$, but at 122 K a spin-flip transition changes the spin modulation to the parallel direction (longitudinal wave: LSDW). The coexisting CDW is associated to a periodic lattice distortion and its period is twice shorter than SDW. Both modulation phenomena appear below T_N, but unlike the SDW the CDW is not affected by the spin-flip transition. There has been a lot of debate about the connection between the SDW and the CDW that has a period of half the SDW and is either caused by a magnetically induced lattice distortion (magnetostriction) or a purely electronic effect based on nesting of the Fermi surface [74–77].

There are several theories describing the presence of the CDW in pure Cr, here we mention two of them. The first one was developed by Young and Sokoloff, it is based on three-band model calculation and states the existence of the second harmonic due to the Fermi nesting properties [79]. The second theory [80] suggests that CDW reflection is a result of magnetostriction, which couples strain to SDW. But so far no magnetic field measurements have been performed to induce a magnetic transition and probe the influence on the CDW. If the CDW strongly couples to the lattice, the timescales for suppression of the CDW will be relatively long. If the coupling of the CDW to the SDW is direct and the pinning influence by lattice defects are less a much faster timescale of the SDW dynamics is expected.

Magnetism of Cr has been the subject of much interest since its first discovery in 1959 by two independent groups using neutron scattering [81, 82]. The first explanation of the satellite peaks as an incommensurate spin density wave was made by Overhauser in 1962 [42]. An extensive review of the bulk properties of Cr was given by Fawcett [83] and in addition a review of Cr at the surface and in thin films was given by Zabel [84]. With the development of facilities providing bright, high coherent X-rays and time-resolved methods there was an opportunity for SDW domain imaging [85], magnetic X-ray diffraction [86], Non-resonant X-ray magnetic diffraction
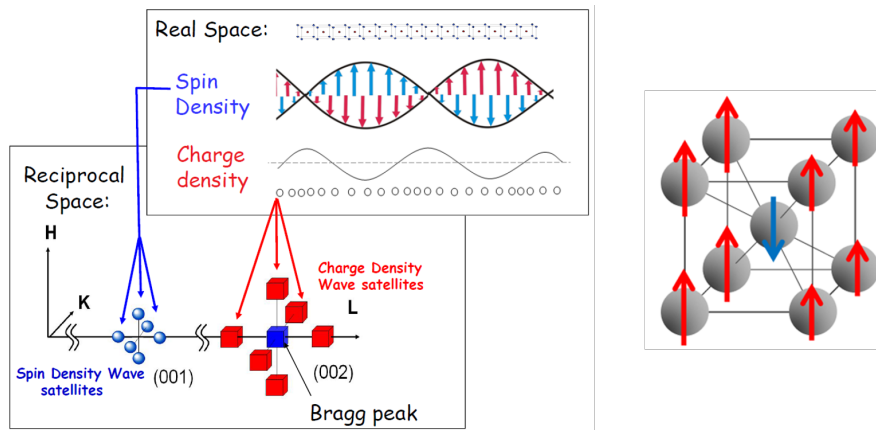
Figure 8.11: On the right side the body-centered cubic (b.c.c.) Cr structure with a transverse SDW with wave vector in the [001] direction and magnetic moments normal to the wave vector. Schematic of incommensurate SDW and CDW in reciprocal and bulk Cr in real space. In reciprocal space: blue spheres represent six SDW satellites around forbidden Cr(001) lattice reflection, red cubes - six CDW satellites around Cr(002) Bragg peak, which is shown as blue cube. For SDW red and blue arrows represent the spin of corner and body-center Cr atoms in the b.c.c. lattice above spin-flip transition [78].

[87, 88], time- and angle-resolved photoemission spectroscopy [89], laser pump - X-ray probe method [90] and many other. Despite the great interest and wide range of studies of CDW and SDW in Cr, there are only a small number of articles from the 20th century mentioning the effect of the magnetic field on these phenomena [91–95]. For this reason, most of the experimental expectations are based on these studies.

8.3.1 Sample damage

Since in the case of Dy all data was obtained using intense lattice Bragg reflection, we were using only little fraction of incidence X-ray energy. However, in the case of Cr our goal is to study both charge and magnetic reflections, which are much weaker than the Cr lattice reflection. According to Overhauser [96], the CDW satellite intensity relative to ordinary Bragg reflection is 10^{-2} and from work of Blume [97] the ratio between scattering cross-section of magnetisation and charge densities is about $\frac{\sigma_{\text{mag}}}{\sigma_{\text{charge}}} \sim 10^{-6}$. In this regard in order to have sufficient noise to signal ratio, we use a great fraction of incident X-ray energy up to 100 %. Thus, it is important to start presenting the results from discussion of a possible effect of radiation damage. To evaluate the radiation damage we carry out static measurements (zero magnetic field, constant temperature) using a

thin 50 micron sample by tracking changes of CDW(002-2δ) reflection from pulse to pulse with varying impinging X-ray intensity.

For this study, the following measurement scheme was chosen: during each data collecting run the sample illumination started with 1 pulse per train, after some time the number of pulses per train was increased up to 30 and at the end it was switched back to 1 pulse/train. According to this scheme, several runs were collected with different X-ray energies, using different combinations of attenuators, with non focused beam with size $\sim$ 1 mm. The temperature of the cryostat with the sample for the first runs was kept at 293 K, and for later runs set at 250 K. The measurement scheme consists of changing the number of pulses per train, since the radiation damage is not present during 10 Hz measurements (Figure 8.12). The first measurement with 30 pulses per train showed that radiation effect is irreversible on short time scale; thus for each run the sample position was slightly changed to reproduce reflection on the detector.
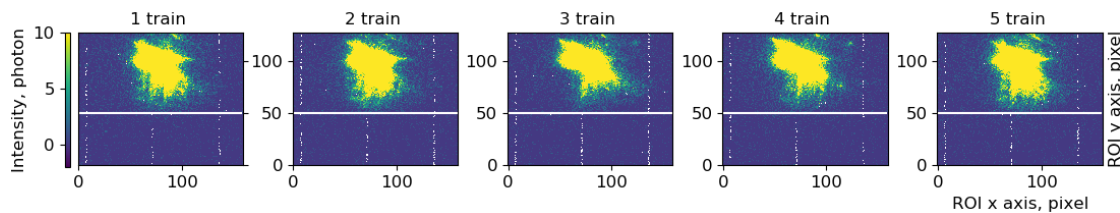
Figure 8.12: The CDW(002-2δ) reflection in a sequence of 5 trains measured with 1 pulse per train and X-ray energy 176.58 uJ per pulse.

The Figure 8.13 shows the CDW degradation peak through the first 10 pulses (out of 30 pulse/train mode) in the first and second trains containing more than 1 pulse with X-ray energy 176.58 uJ per pulse. In the first pulse of the first train reflection appeared as a bright dense cluster of pixels. However, in the second pulse the intensity drops crucially, split on parts occurs, and sectioned expansion with intensity fading is progressing in the following pulses. The intensity range for all plots of Figure 8.14 remains the same, so the decrease in reflected intensity can be seen. The white horizontal line, which indicates the peak center of mass position, gives the reference for spreading in the vertical direction. After the 100 ms break between X-ray pulse trains both the shape and the overall intensity do not recover to the initial values.

To illustrate the ability of recovering the scattered intensity on a slower time scale the Figure 8.14 presents a comparison of peak profile along the x-axis. The Figure 8.14 only shows the profile of the first pulse per train, regardless of how many pulses per train was used (indicated on the figure).

The CDW reflection summed intensity and the position obtained using X-ray energy 176.58 uJ per pulse with 1 pulse/train remains relatively stable during the 100 train. However, with an
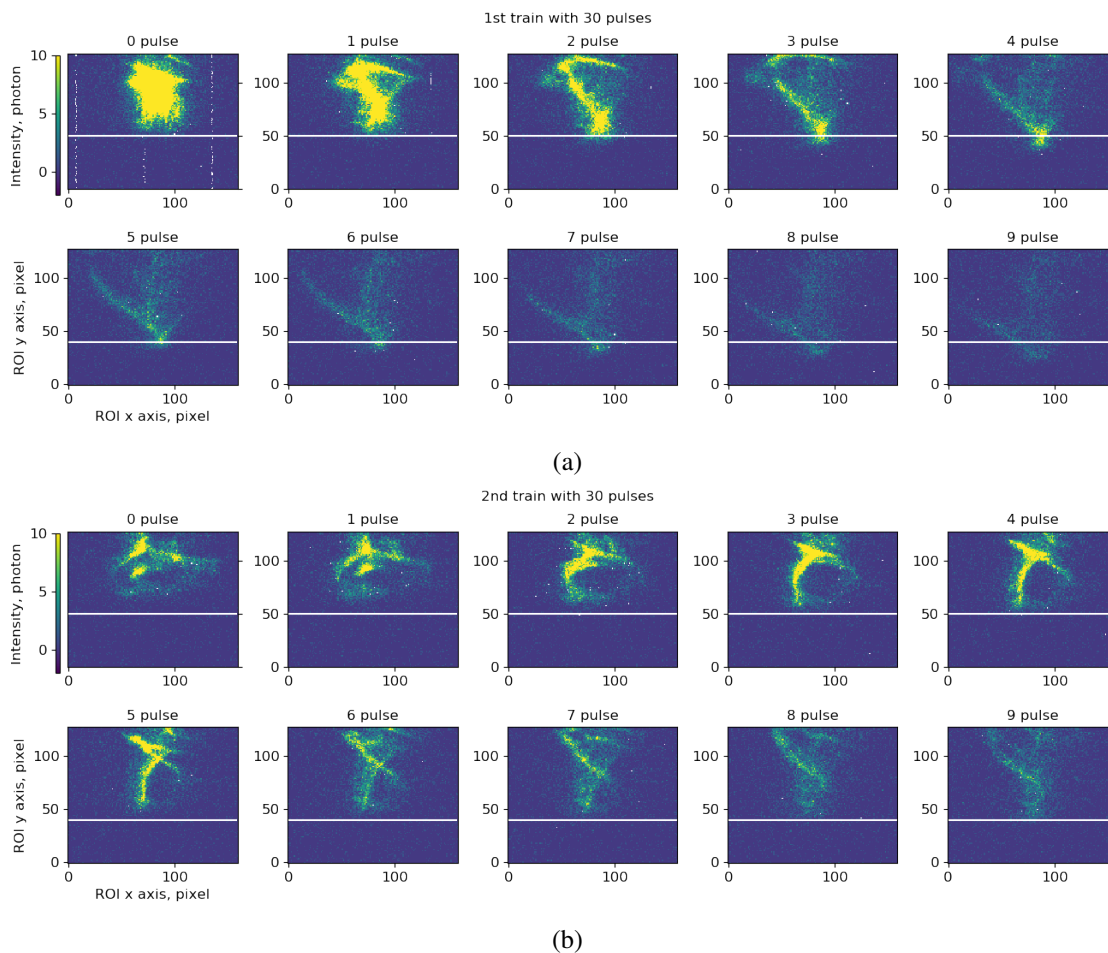
Figure 8.13: The CDW(002-2δ) reflection change due to X-ray illumination with X-ray energy 176.58 uJ per pulse. The first 10 pulses out of 30 pulses/train are shown: (a) the 1st (b) the 2nd train consist of 30 pulses after the switch from 1 pulse per train mode.
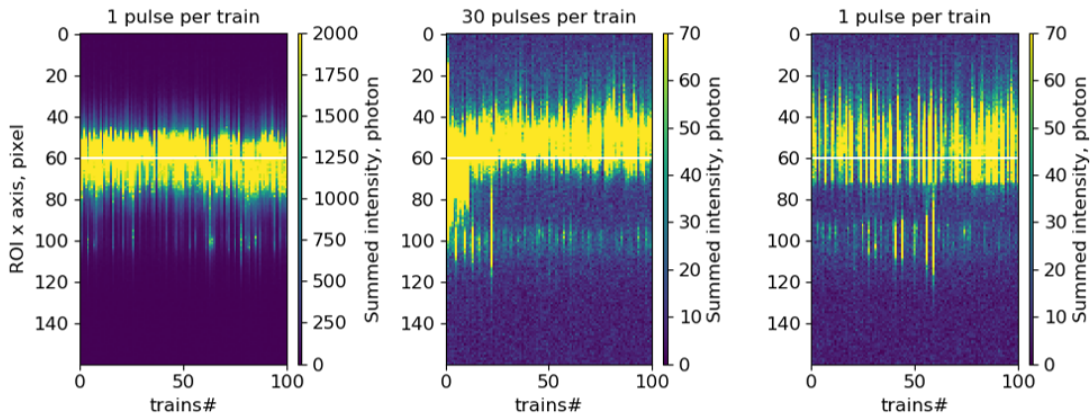
Figure 8.14: The CDW(002-2δ) peak profile in along the axis of the first pulse for 100 trains in three consecutive measuring regimes: 1 pulse per train, 30 pulses per train, 1 pulse per train. The white line represent the peak center of mass position during the first regime and facilitates a visual comparison of the movement of the peak along x-axis as a result of the X-ray illumination. The X-ray energy 176.58 uJ per pulse.

increase in the number of pulses per train up to 30 the summed intensity scale value drops to 3.5 % from the initial value. Also during 30 pulse/train mode the peak profile position shifts in x-axis within the first 10 trains as demonstrated on Figure 8.13 by changing the position of the peak intensity relative to the white line. Also after changing the total amount of pulses back to 1 pulse/train both position and intensity values do not recover even within 100 trains. To recover the intensity of reflection it was necessary to move on a non-illuminated sample area, by changing the height position of the holder. It is clear that main damage is happening in the first trains of multiple pulse regime and position as well is not recovered with time. The Figure 8.13 also shows the second weak peak on the profile, the intensity of which is anticorrelated with the bright peak. This double peak structure is a sign of some mosaisity in the sample, which also might be caused by radiation damage from previous experiments. The influence on a sample by the XFEL beam canbe caused by different physical effects: sample heating, radiation damage and dynamics of the CDW. To separate the effect of sample heating from other more complex damaging processes, pulse resolved calculations of the heat distribution over the depth of the sample have been carried out. These simulations were performed using Python code, which was developed in at European XFEL [98]. First of all, to verify whether there is enough time between XFEL trains to have a uniform temperature over the thickness of the sample, we use the equation for the characteristic decay time of a temperature gradient over a distance L (thickness of the sample):

$$t_{\text{char}}(L) \sim \frac{L^2}{D}, \text{where } D(T) = \frac{K(T)}{\rho c_p(T)} \text{ is the thermal diffusivity} \qquad (8.3)$$

Here ρ is the mass density, $c_p(T)$ is the specific heat and $K(T)$ is the temperature dependent thermal conductivity. Thus, for Cr, $D(250K) \approx 0.304 \; cm^2 s^{-1}$ and for 50 um thick sample $t_{\text{char}} \approx 800 \; ns$, which is much shorter than the 100 ms between pulse trains. Thus, by the time the next XFEL train arrives, the crystal is fully recovered to the initial temperature. In Figure 8.15 is demonstrated the heat increase and distribution for up to 30 pulses for different transmission values. Since only a limited part of the sample contributes to the diffraction (limited by absorption) the vertical black line marks half of the attenuation length $\xi \sim 5$ um for Cr at 11 keV with at an angle of incidence of about 23 degrees. We decided to mark half, because due to the definition of attenuation length the depth into the material measured along the surface normal, where the intensity of X-rays falls to e^{-1} of its value at the surface. However in reflective geometry, the X-ray must not only enter but also exit the sample. Therefore, the penetration depth will be half the full path. Another important mark for analysing the results of temperature and magnetic dependencies of SDW and CDW reflections is Neel temperature: horizontal dotted line. Unfortunately, with X-ray energy 176.58 uJ per pulse the penetration depth is heating up over Neel temperature after 10 to 15 X-ray pulses of a train and for X-ray energy 218.4 uJ per pulse the critical temperature is reached after 5 pulses.

To demonstrate the effect of temperature rise on CDW($002\text{-}2\delta$) the temperature dependencies for integrated intensity and wave modulation vector was plotted and fitted with sum of exponential and first degree polynomial model. As demonstrated in Figure 8.16 curves for integrated intensity have a big spread within trains, thus to apply fitting procedure it was necessary to average these curves for all trains with same number of pulses. However, here already without averaging it is easy to notice the difference in the shape of the curves for X-ray energy 176.58 uJ and 218.4 uJ per pulse. We assume that, up to a certain threshold energy of X-ray radiation, sample damage consists in significant but gradual thermal heating, while after a critical energy, X-ray radiation causes direct defects in the lattice structure.

The modulation wave vector values were calculated from the center mass position of the reflection on the detector module for each pulse in averaged trains and each pulse was assigned a temperature from the estimations. The green and red curves on Figure 8.17 corresponding to X-ray energy per pulse 17.3 uJ and 46.08 uJ, respectively, have a good agreement with the theory curve taken from reference [94]. In both these cases the temperature (averaged temperature on half of absorption length) does not cross Neel temperature. However orange and blue curves, corresponding measurements with energies about 63 uJ per puslse, remain constant in opposition to theory. These measurements had higher starting temperature ~ 293 K and are expected to
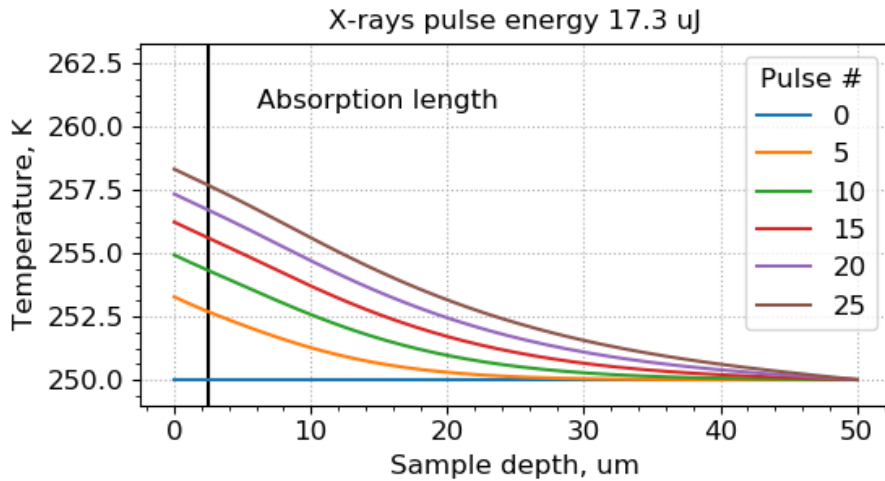
(a)
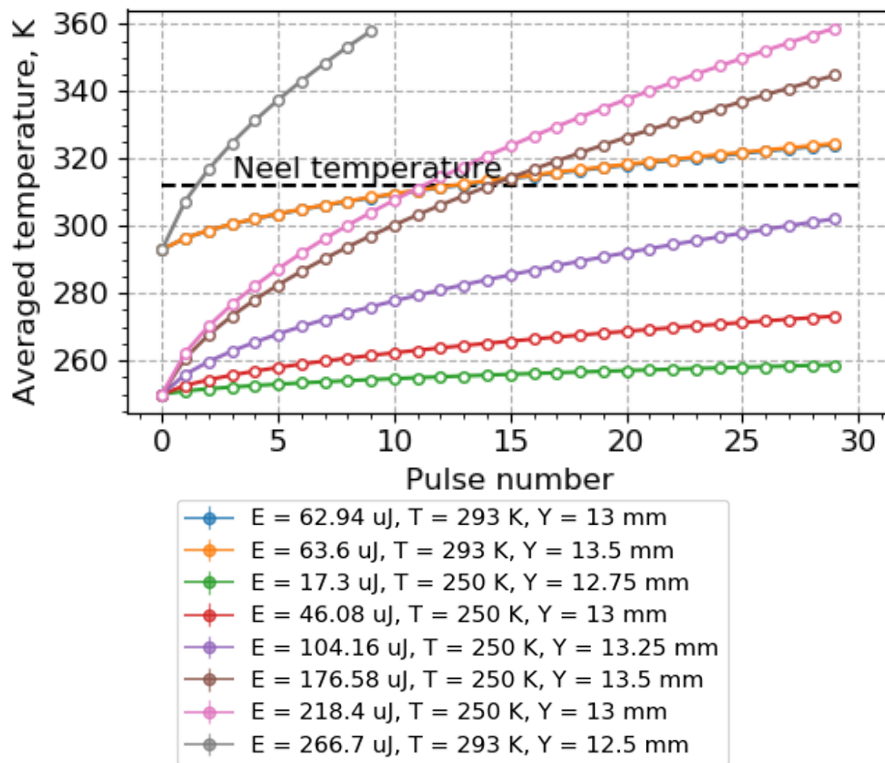
(b)

Figure 8.15: (a) Temperature profiles along sample depth for every 5th pulse in the train containing 30 pulses with X-ray energy 17.3 uJ per pulse. The black solid line indicates the sample depth equal to half of absorption length. (b) The pulse number dependence of averaged temperature on half of absorption length for different X-ray energies. The dotted line indicated the Neel temperature for Cr.
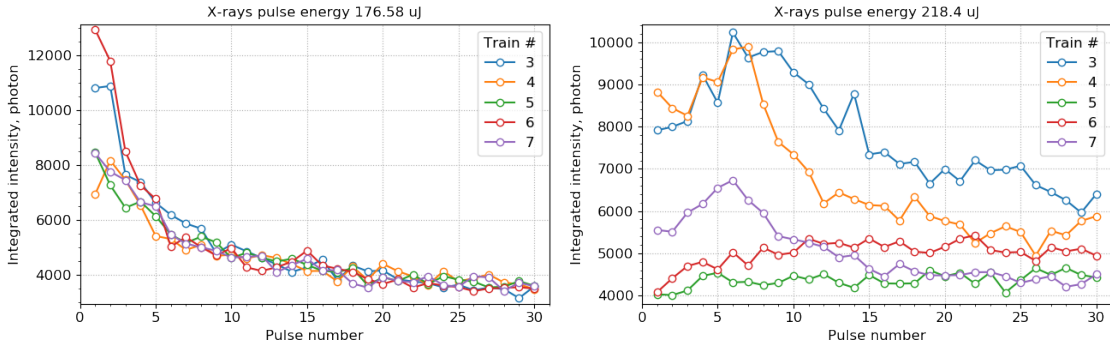
Figure 8.16: The dependence of the integrated intensity of CDW(002-2δ) reflection from pulse number. The measurements were obtained at 250 K with 30 pulses per train with X-ray energy 176.58 uJ (left) and 218.4 uJ (right) per pulse.

cross Neel temperature due to simulation model. The same constant trend shows curves for higher X-ray energy values, which also exceed 311 K within 30 pulses per train.

As it was shown earlier (Figure 8.16) the integrated intensity curves for each train have a big variation with a maximum intensity in the first pulse. Thus after averaging error bars have significant values, in addition curves were normalised on the first pulse and here we are focused the decay of scattered intensity with respect to the first pulse. The first plot on the Figure 8.18 demonstrates three curves with small X-ray energy spread: 46.08 uJ, 62.94uJ and 63.6 uJ, but with different initial temperature 250K, 293 K, 293 K, respectively (the color match is the same as on Figure 8.17). The red line has faster exponential decay and shorter region of polynomial slope, while blue and orange lines has slower exponential decay, which is going up to the critical temperature and above has a flatter polynomial slope. We also see a similar trend in the second plot on Figure 8.16 for different X-ray energies: green and red curves are far from Neel temperature and has fast decay, while brown and purple curves have elongated exponential decay with almost flat polynomial part. For two maximum values of transmission curves has completely different shape. Relative integrated intensity on pink curve increase in first pulses and only after ~ 10 pulses has gentle decline close to constant.

X-ray energy (uJ)	17.3	62.94	63.6	46.08	104.16	176.58	218.4	266
Exponential decay	8.38	2.16	1.52	2.05	3.07	3.74	0	0
Polynomial slop	-9.49	-15.01	-14.83	-194.25	-13.95	-16.12	-18.42	-92.92

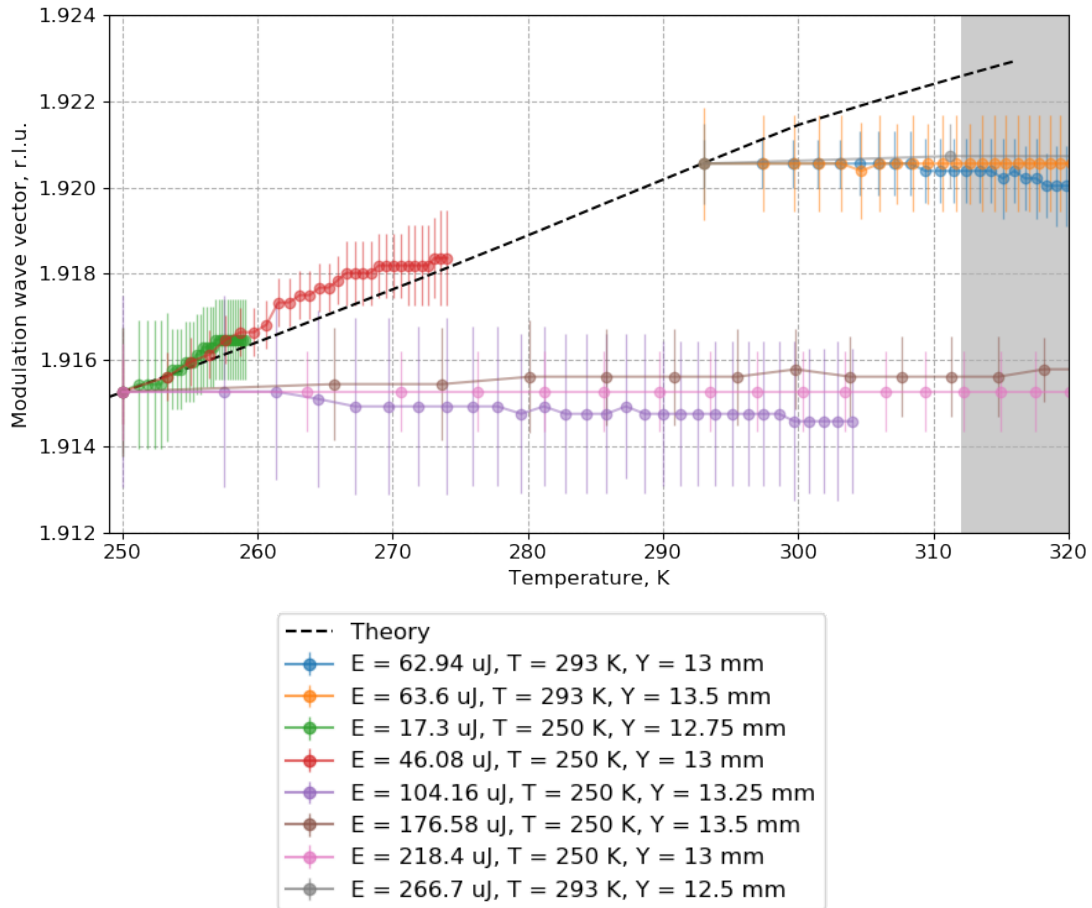The anomalous behavior of the modulation wave vector indicate that the CDW satellites seem

Figure 8.17: The temperature dependence of modulation wave vector obtained on CDW(002-
2δ) reflection. The different colors represent different measurement conditions de-
scribed in the legend. The dotted black line represents theory values, calculated
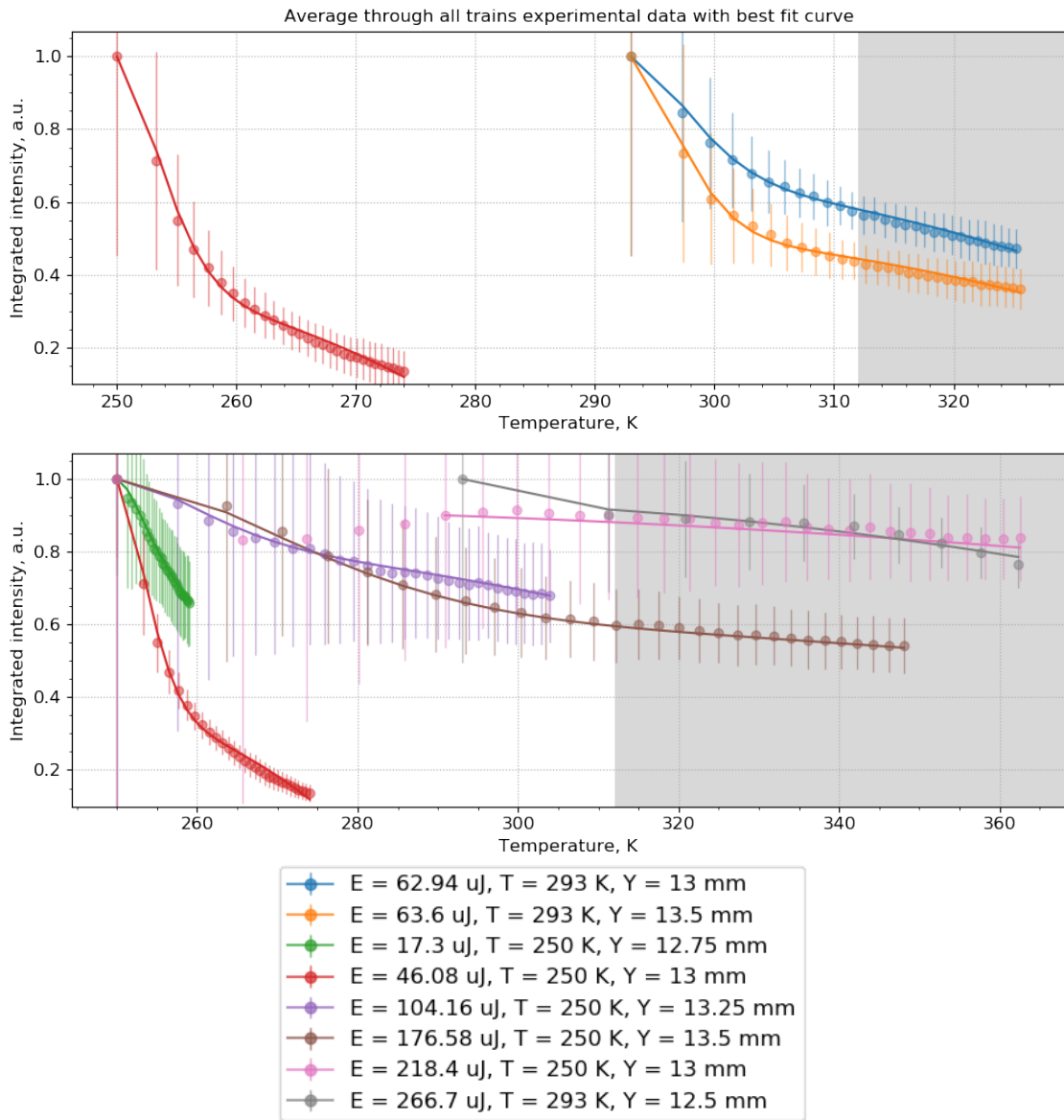using δ values from [99]. The shaded area indicates the temperature range above
Neel temperature.

Figure 8.18: The temperature dependence of integrated intensity of CDW(002-2δ) reflection. The dots indicate experiment data, the solid lines indicate fit with combination of exponential and polynomial models. The different colors represent different measurement conditions described in the legend. The shaded area indicates the temperature range above Neel temperature.

to stay locked in at that specific temperature below Neel temperautre, even if the X-ray pulses keep warming up the crystal. For the X-ray energy values below 46.08 uJ the nature of the wave vector change correspond to simpe sample heating. However, the anomalous behavior of integrated intensity depending on X-ray energy indicate, that for the X-ray energy values above 46.08 uJ the sample damage sample undergo more complicated damage effect such as creation of crystal structure defects. Such a comprehensive X-ray analysis of the consequences of damage was carried out only after the last experiment of this project. For this reason, all subsequent measurements of SDW satellites were made with X-ray energy $\sim$ 900 uJ per pulse, due to the low signal to noise ratio without taking into account sample damage. In order to minimise this effect in the analysis, we will take only the first pulse from the train. Finally, these results emphasize the importance of evaluating X-ray beam heating and choosing the optimal radiation parameters for studying solid samples at European XFEL.

8.3.2 Temperature dependence

In regard to sample damage, it is important to mention here that all temperature measurements were carried out with maximum 5 pulses per train, also only the first pulse in train is used for data analysis. As mentioned above all the experiments were carried out in parallel with the development of the PUMA setup and the improvement of the measurements protocol for this particular device. Thus, conditions were not fully reproduced from experiment to experiment. However, by developing a single strategy for processing data from early and late stages, the difference in measurement is negligible for comparison. In this section all experiment were carried out using bulk single crystals with thickness of 1 mm and two possible surface orientations: (100) and (111).

Since we use a new setup and not standard photon energy for magnetic reflection in order to confirm that the found reflections at expected angular positions behave as expected from the literature review. In this regard, we start from temperature dependence of Q wave vector and integrated intensity of CDW($002\text{-}2\delta$) satellite in Cr(100) sample. The Figure 8.19 shows two sets of measurements: in range from room temperature down to 50 K and later with more narrow range from 160 K till 115 K. In both cases Q value decreases during cooling and the rate of decline corresponds to the reported [99] increase of δ in low temperatures. The integrated intensity in the wider range of temperatures has gradual rise, which flattened between 100 and 50 K, the same trend was described in [94]. In a narrower temperature range, the curve does not reach the constant region, but also shows a slow growth predicted by mean-field theory.

From relatively simple case of intense CWD with only one satellite reachable in MID instrument geometry, we move to significantly less intense SDW. Under normal conditions bulk Cr forms a magnetic poly-domain state, i.e three domains (Q_x, Q_y, Q_z) are formed in different regions of crystal, each containing a single magnetisation wave. These domains give rise to six magnetic satellites in reciprocal space. At the first stage of the project such multi-domain sample is used in assumption with the assumption that in such a sample there will be more opportunities to observe the effect of temperature and magnetic field on different satellites. In this regard, two reflections, which assumed to be SDW($001\text{-}\delta$) and SDW($001\text{+}\delta$), were found at a distance of $2\Theta \sim 1.6$ deg from each other, which corresponds to theoretical calculations. By measuring wide angle range rocking curve we track both satellites on the Figure 8.20, in addition the beam profiles for both reflections are demonstrated with correspondence to AGIPD position converted into degrees.

The measurements were carried out using Cr(111) sample in the temperature region from 140 K down to 80 K, where SDW is undergoing a spin-flip transition from TSDW to LSDW. It is expected that satellites with polarisation perpendicular to wave vector show a dramatic
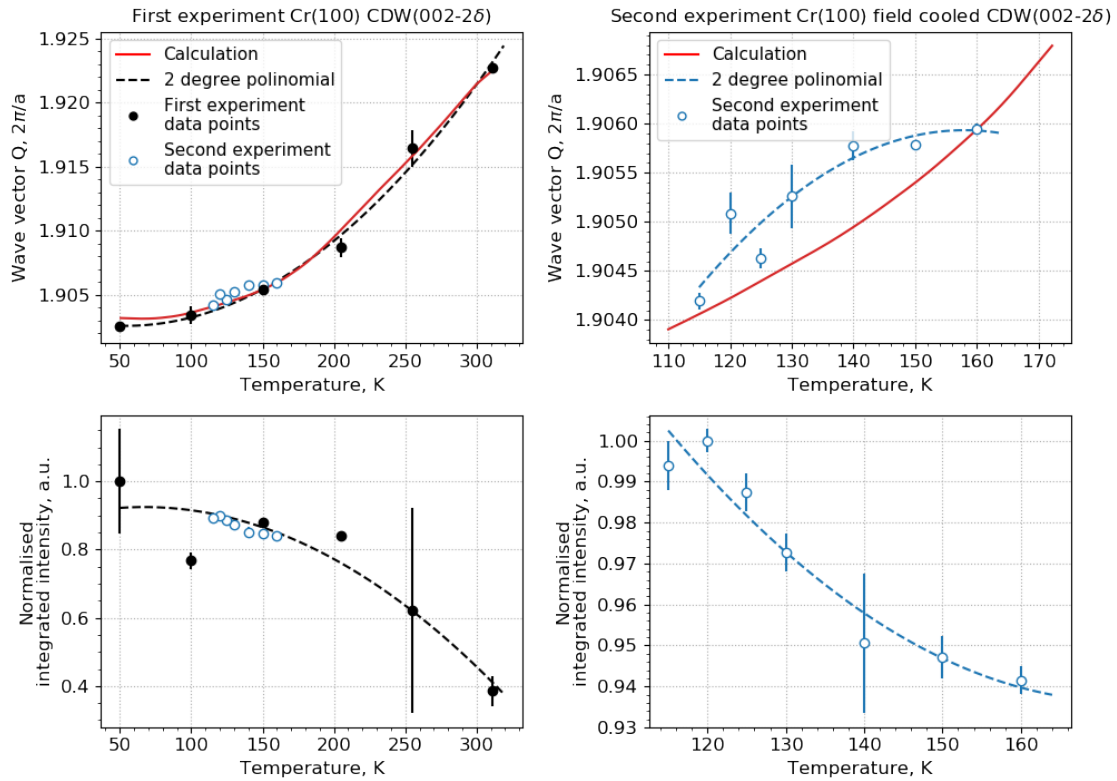
Figure 8.19: The temperature dependencies of wave vector (up) and of integrated intensity (bottom) obtained on CDW(002-2δ) reflection in early (left) and later (right) project stage. The dots indicate experimental data, the dotted line indicate a fit, the red solid line indicate theoretical calculations using δ values from [99].
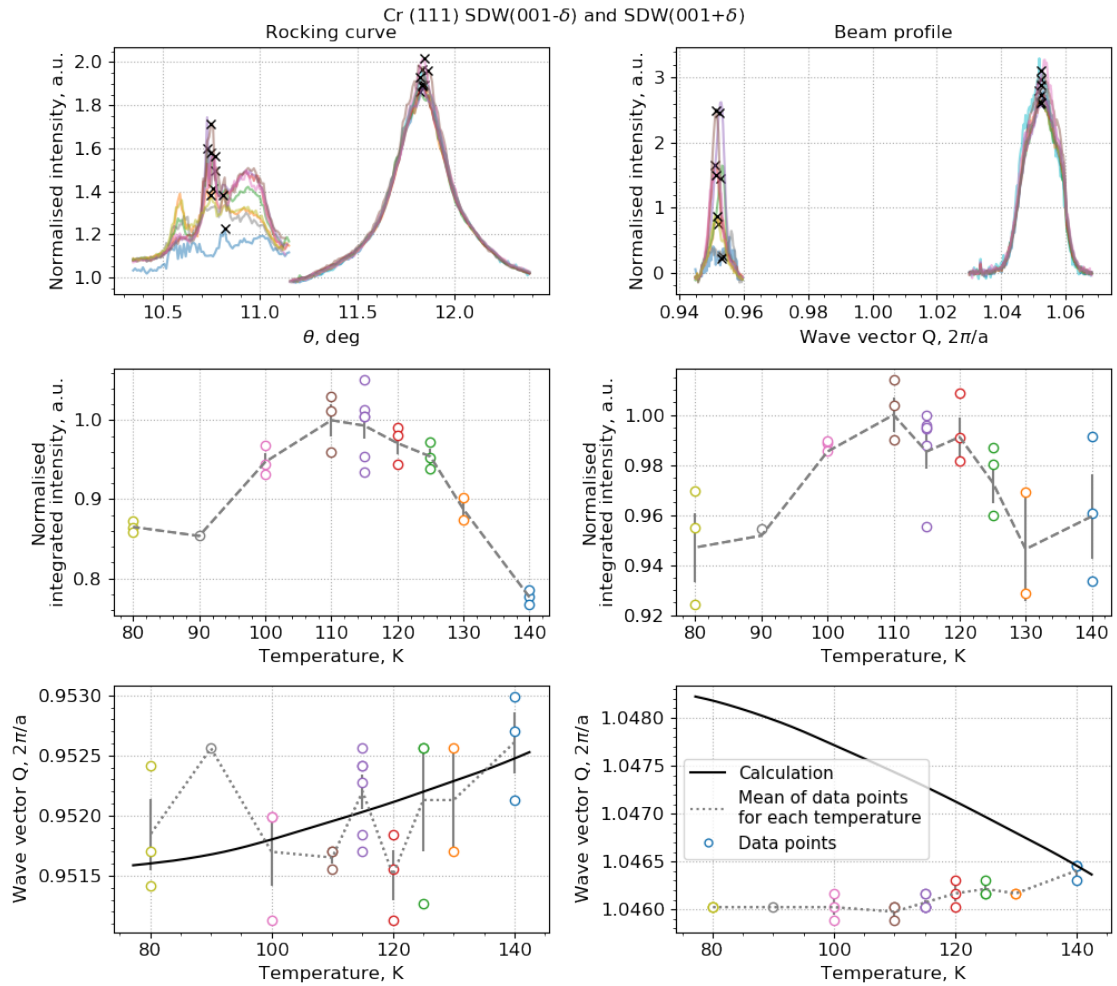
Figure 8.20: For two SDW satellites Cr(111) sample: rocking curves for both SDW(001-δ) and SDW(001+δ), each color corresponds to different temperature and cross mark in the center of the peak (left, up). Beam profiles for two peaks at the angular position corresponding to the center of rocking curve, here cross mark corresponds to the center of peak profile curve (right, up). The temperature dependence of integrated intensity of presented rocking curves for SDW(001-δ) (left, middle) and SDW(001+δ) (right, middle). The temperature dependence of lattice parameter calculated from center position of beam profile for SDW(001-δ) (left, bottom) and SDW(001+δ) (right, bottom). The black solid line shows values, which were calculated using δ values from [67].

drop in reflection intensity due to a decrease of scattering cross-section. It was shown [55] that the non-resonant cross-section of magnetic scattering is most sensitive to the component of the spin-density wave with polarisation perpendicular to the scattering plane:

$$\left(\frac{d\sigma}{d\Omega}\right)_{\text{magnetic}} = r_0^2 \left(\frac{\lambda_c}{d}\right) |S_\perp|^2 \tag{8.4}$$

where, r_0 is the classical electron radius, λ_c is the Compton wavelength, d is the lattice spacing and S is the spin component perpendicular to the scattering plane. The drop of intensity of the magnetic scattering below spin-flip transition temperature was demonstrated in experiment [73]. To improve statistics of low photon reflections at each temperature rocking curve was measured several times, thus points with the same color at integrated intensity plot corresponds to one averaged rocking curve and beam profile respectively. After this procedure, a dotted line was drawn through the averaged values. For both peaks the line has a peak around 110 K and the slight values drop is coming only around 90 K, thus we do not see the expected level of decline at 122 K. There are several explanation for these: The alignment of SDW domains is so that LSDW and TSDW polarisation for SDW(001-δ),SDW(01-δ0) and SDW(1-δ00) satellites relatively to scattering plane is such that during the transition intensity redistributed almost equally [100]. Another reason might be in X-ray thermal effect, which was described in the previous section, due to the heating up, the sensor reading might differ from actual temperature. In this case slight drop of intensity around 80 K is a beginning of transition region. Also depending on the sample manufacturing spin-flip temperature can be shifted up or down, however this was checked afterwards using SQUID method for all sample. On Figure 8.21 the temperature dependence of magnetic moment for Cr(111) sample the spin-flip transition is found around 123 K as well as for Cr(100).

Finally, temperature dependence of wave vector for the positive satellite SDW(001+δ) has satisfying agreement with theoretical calculations based on $\delta(T)$ published in [99]. In contrast to this, the simulation predicted Q values increase for the opposite reflection, however the negative satellite SDW(001-δ) has slight drop and flattening with cooling (Figure 8.20). We assume that such a discrepancy between the experimental data for one of the reflections, together with a significant difference in the shape of the rocking curve for SDW(001+δ) and SDW(001-δ), may already be a sign of sample damage, caused by X-ray energy 900 uJ and long exposure time.

In order to get rid of redistribution of magnetic scattered intensity between different magnetic domains, the field-cooling procedure was applied using SQUID setup with Cr(100) sample. This method is described in details in Brown et al. [101] and Bastow [102] and mentioned in number of articles afterwards [83, 86]. This simple procedure consist of two steps: to heat the sample above the Neel temperature and place it in a magnetic field and cool it below this critical
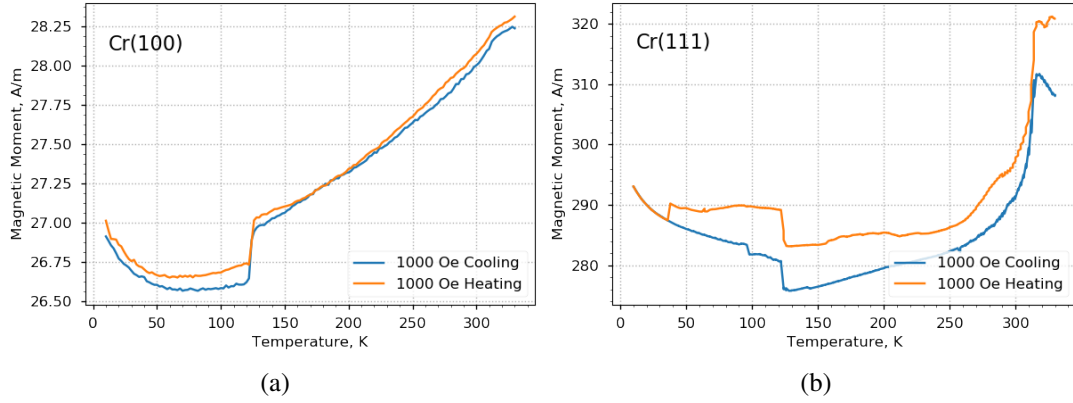
Figure 8.21: Temperature dependence of magnetic moment for two samples: (a) bulk Cr(100), (b) bulk Cr(111).

point. The direction of the magnetic field in this procedure is defining the single magnetic modulation $\mathbf{Q}$ vector direction . Thus in our case to have single-Q transversely polarised SDW state characterized by the incommensurate magnetic satellites at $\mathbf{Q}_{\pm} = (1 \pm \delta, 0, 0)$ B-field was directed perpendicular to the crystal surface. This rotation of magnetic moments is irreversible only if external magnetic field exceeds 2.4 T [93], in our case was applied 7 T field.

The same measurements were carried out using field cooled Cr(100) and repeated before sample was exposed to magnetic field upto 12 T (within the framework of magnetic measurements on PUMA setup) and after. These temperature dependencies around spin-flip transition of wave vector and integrated intensity are demonstrated on Figure 8.22. Upper plot corresponds to SDW(001+δ) satellite and lower plot to SDW(001-δ) and in addition curves of dependencies before magnetic field exposure are highlighted in orange, after exposure to a magnetic field in blue. Since a rather narrow temperature region is chosen, the change in parameters is rather small which, together with the low signal-to-noise ratio, complicates comparison with expectations. However, all intensity curves has characteristic drop around 115 K, after which negative peak loses the intensity and the positive has a slight increase. In the same state wave vector has similar shape at 115 K and both peaks moving the same direction at the detector, thus SDW(001-δ) agrees with theoretical line and SDW(001+δ) not. After magnetic measurements were carried out and the same temperature measurements repeated, the expected transition feature at spin-flip temperature is smoothed out. Also the wave vectors behaviours are switched so that SDW(001+δ) satellite curve agrees with estimations, but SDW(001-δ) values stay constant.

In combination with the conclusions drawn about sample damage with X-Ray and estimations of sample heating up with single pulse, we conclude that field-cooling procedure was not

successful. Also two Cr samples with different simple surface orientation demonstrate same unexpected SDW satellites behaviour.
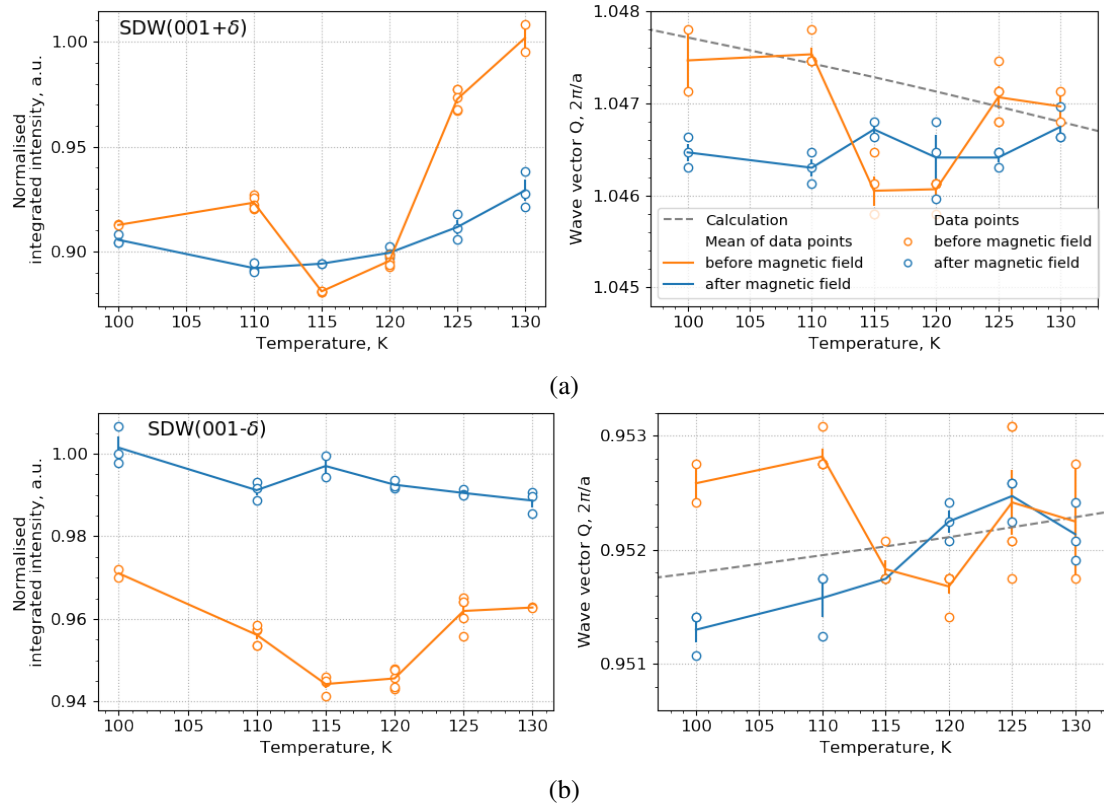

Figure 8.22: Temperature dependencies of integrated intensity and wave vector before and after applying magnetic field obtained on (a) SDW(001+δ) satellite and (b) SDW(001-δ) satellite. The black doted line shows values, which were calculated using δ values from [67].

After observing the absence of a significant drop in the intensity of reflections at spin-flit transition, it was decided to check if found reflections fade away with crossing antiferromagnetic-paramagnetic transition. This measurement were carried out using the first sample Cr(111), which was first warmed up from room temperature up to 340 K and cooled down. The wide rocking curve scan covering angular range for both reflections was made on each temperature in this range and the final hysteresis plots are demonstrated on Figure 8.23. The level of the background is marked with grey line, since peaks are located on different modules it was evaluated separately and noise values are slightly shifted. Although the intensity has a crucial decrease none of the reflections disappeared completely, we assume this to be connected to presence of defects in the crystal resulting in pinning of SDW and CDW.
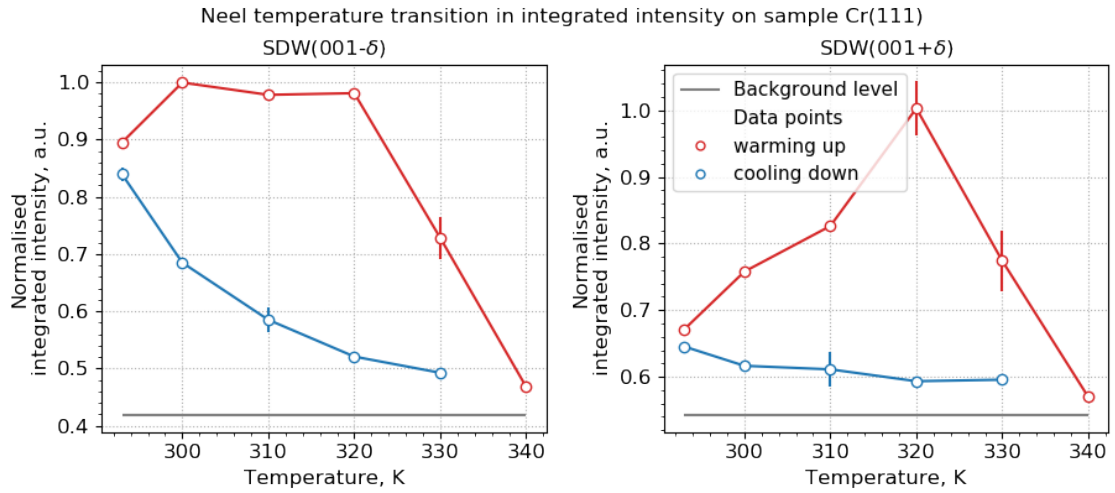
Figure 8.23: Temperature dependencies of integrated intensity during warming up and cooling down obtained on SDW(001-δ) satellite (left) and SDW(001-δ) satellite (right). The black solid line indicate background level of AGIPD module.

8.3.3 Magnetic dependence

The theory of magnetic ordering says that each antiferromagnetic structure has a critical value of external magnetic field, such that under the influence of this field, the magnetic moments will be reoriented. We already mentioned one such example, it is field-cooling, where a relatively low, but constant magnetic field force all domains wave vectors to align parallel. There are very few studies which explains the effect of external magnetic field on Cr antiferromagnetic state. In the work of Werner et al. [93] was measured the minimum magnetic field necessary to produce a single-Q SDW sate. In the same work was demonstrated that LSDW reflections were missing after applying 16 T B-field, which consistent with the conclusion from [92] with 11 T magnetic field. The formation of a twisted SDW under influence of low magnetic field on TSDW reflection was shown in the work of Tsunoda and Nicklow [95].

For these measurements we used the field-cooled Cr(100) bulk sample and two temperature states: above and below the spin-flip transition based on SQUID data 8.21: ~ 100 K and ~ 140 K. In addition to a low signal-to-noise ratio, a particular analysis challenge for these measurements is a big difference in statistics: one data set contains a lot of trains with zero magnetic field and a significantly smaller number of trains during the discharge. Also based on the section about sample damage, to avoid mixing heating and magnetic effects, even though every train contains 10 pulses, we take into account one the first one. The low signal-to-noise ratio leads to large errors when trying to fit the peak with some model. Thus, the approach to the analysis of magnetic data, which was applied in the case of Dy, is not suitable here.
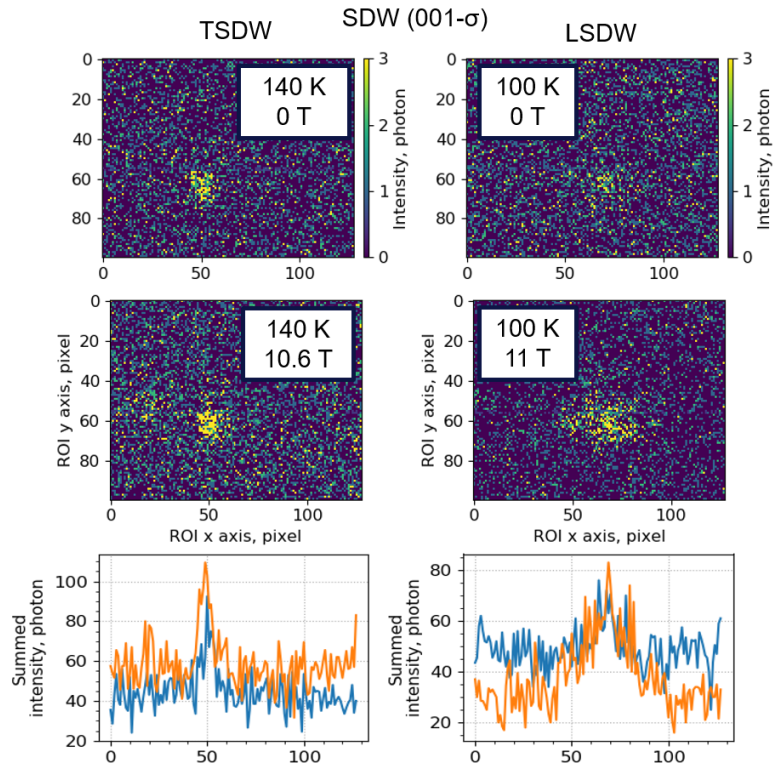
Figure 8.24: Demonstration of low signal to noise ratio with X-ray energy 560 uJ using SDW(001-δ) reflection in zero and non-zero magnetic field for two temperatures: 140 K (above spin-flip transition) and 100 K (below spin-flip transition).
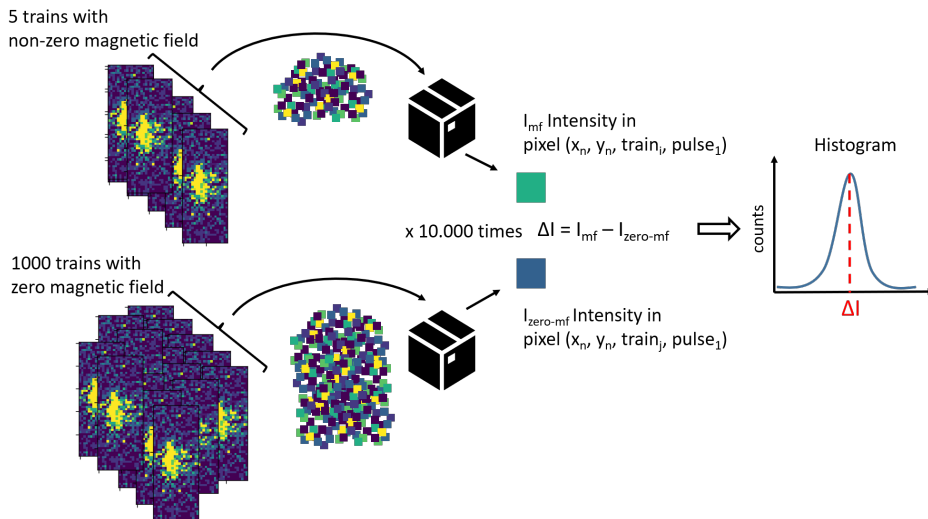

Figure 8.25: The bootstrap method scheme for analysis of magnetic data. A detailed description of this scheme is given in the text.

103

For kind of data sets we chose the bootstrap method with replacement [103]. The bootstrap method is a statistical technique for estimating quantities about a population by averaging estimates from multiple small data samples. The samples are constructed by random observations from data set, one at a time and returning them back into the data set after they have been chosen (this part is called "with replacement").

The scheme for this data analysis method is shown on the Figure 8.25. In our case, there are a set of 5 trains (events) containing non-zero magnetic field and a set of 1000 trains (events) containing zero magnetic field. For both sets we choose the same region of interest (ROI) containing the reflection and split each ROI on pixels. Thus, we form two "boxes" corresponding to two sets (trains with non-zero magnetic field and with zero magnetic field) consist of independent from each other pixels. Each pixel has intensity value and four assigned coordinates: x_n,y_n,train_i,pulse_1, the first two coordinates are positions of the pixel on the module in x and y axis, the third is train number from the set and the last one is the pulse number, which in our case is equal to one. The next step we select one pixel from the first "box" and one pixel from another "box", these pixels have the same coordinates, but different random train numbers. The intensity difference of these two pixels is our first point the first value to make the intensity difference histogram. We make a large number (in our case 10000) of such pixels comparisons: one pixel with random train coordinate from set of discharges and another one from set of zero magnetic field. The result is the histogram for intensity differences between these two magnetic states. The median of this distribution for each pixel with x_n and y_n coordinates is the position dependence of intensity difference. Finally, for the asymmetric error bars we take difference between median and 5th percentile and between median and 95th percentile. Here percentile is the value at which 5 % (or 95 %) of the distribution values lie above that value and 95 % (or 5%) of the answers lie below that [104].

Using this approach the differences between sample intensity in zero magnetic field and different power of magnetic field are plotted on Figure 8.26 for CDW(002-2δ) reflection at 140 K and 110 K and for SDW(001-δ) reflection at 140 K and 100 K. For all values of the magnetic field, this difference tends to zero for spin and charge ordering. Despite expectations that the magnetic reflections are sensitive to the external magnetic field no change was observed. There are several explanation for this. The critical magnetic field is $\sim$ 11 T, however the maximum field, which was reached in the last experiment of this project was 12.5 T. It was not possible to apply such high magnetic field for many repetitions due to high mechanical stress causes vacuum leak inside of sample chamber, which takes sufficient for duration of experiment time to fix. The second assumption is that SDW satellites the most sensitive to external magnetic field influences have a wave vector that is parallel to the direction of the magnetic field [93]. Thus, in order to be able to observe the effect using non-resonant X-ray diffraction on magnetic ordering

with external magnetic field value close to critical a different experimental geometry would be preferable. Finally, coming back to the problem of sample heating with X-rays, the sensitivity to the field is determined not only by the direction of the wave vector, but also by the polarization of the spins. Therefore, if to follow one type of SDW reflection, but maintain the temperature above spin-flip the polarisation can be wrong for detecting the change in peak parameters [99].
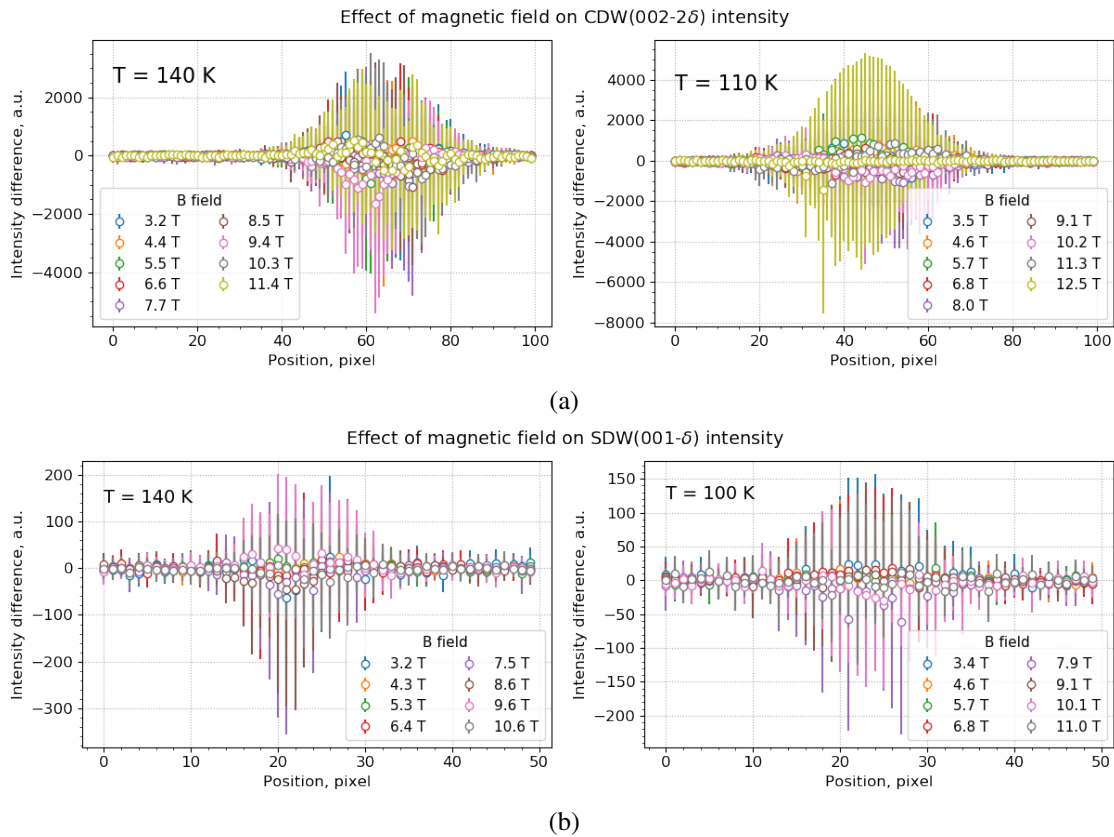

Figure 8.26: Effect of magnetic field on (a) CDW(002-2δ) reflection (b) SDW(001-δ) reflection at two temperatures 140 K (left) and 100-110(K). Intensity difference between a sample in zero and non-zero magnetic fields along position. Different colors correspond to different magnetic field strengths.

9 Conclusion and Outlook

For long time antiferromagnetic materials were considered to be interesting, but did not wide spread applications in modern life so far. Despite this they have several properties favorable elements in spintronic devices, including ultra-fast dynamics, zero stray fields and insensitivity to external magnetic fields. This holds the potential for competition with ferromagnetic materials in solving the problem of magnetic memory storage. A research of fundamental properties and dynamics in magnetic materials actively uses X-ray and neutron diffraction methods. In this regard X-ray radiation produced on big facilities like European XFEL is in high demand in these studies, due to unique characteristics like: high brilliance, coherence and temporal structure. In addition to continuously improving illumination properties new methods and devices are developed. In this project we study two different types of antiferromagnets Dysprosium and Chromium using newly developed pulsed magnet setup and method type of pump-probe and non-resonant X-ray diffraction at MID instrument at European XFEL.

The PUMA setup was successfully commissioned and several experiments were carried out including user research, where was used the cryo-cooling part of our device. During this project we tested and fixed operation of each part and worked out the order of elements installation in the limited period of time between beamtimes. This device fully operational through XFEL controlling system Karabo and has user-friendly interface including all safety precautions. Several standard operating procedures have been developed such as: sample change, sample alignment in X-ray beam, rocking curve scans in reflecting geometry, temperature and magnetic field scans. Finally, PUMA setup demonstrated high stability against vibrations, confidently cooled and maintain sample in temperature down to 8 K and reached magnetic field power up to 12.5 T. In this regard, it is planned to improve split-coil manufacturing to reach higher magnetic field power, however, maximum power operation still causing vacuum leak in multipurpose chamber, which need to be addressed in future. In addition, wide range of research would benefit from different geometry, where B-field direction is lying in diffracting plane. For the long-term plans, since a lot of sample has very small dimensions, more accurate azimuthal and tilting manipulation for different reflections search would be also beneficial.

As a part of preparations for experiments different sample treatment was carried out such as:

chemical and mechanical polishing, laboratory X-ray diffractometer characteristics and SQUID magnetometer measurements.

The first part of research was done using Dysprosium sample, carried out experiments on Dy(0002) crystal reflection covered full range of temperatures and magnetic fields on a phase diagram, which showed antiferromagnet – ferromagnet transition with two different intermediate states named "fan I" and "fan II". Using developed data analysis procedures, a temperature dependence for lattice parameter was plotted and it agreed with theoretical expectations. As a next step two temperatures 170 K and 150 K, which correspond to two types of fan structures and two types of phase transitions, were chosen. Here the first type of phase transition was demonstrated as an abrupt jump in value of lattice constant, while the second type had smooth change of the same parameter. After this difference was proved the same measurement sequence was reproduced for the wider range of temperatures and for magnetic field up to 4 T. We proved that our setup and data analysis can reproduce result with good agreement with previously demonstrated phase diagrams. In addition, we showed that the mechanism of lattice parameter transition is going through appearing of two peaks with two slightly different positions, but the same shape. The PUMA setup opens a new perspective for Dy research using resonant X-ray diffraction on the charge-forbidden antiferromagnetic Bragg peak caused by lattice modulation in various magnetic field. The time duration of 1 ms of magnetic pulse with use of all 2700 pulses can give more details of both transitions. The same goal can be reached with thin setting of trigger timing of the capacitor bank discharge. As a bit more, ambitious step would be combined experiment with PUMA setup and split-delay line to resolve even faster magnetic dynamics of the first type of phase transition.

We studied number of phenomena in single crystal Chromium samples with different characteristics: two orientations of the crystal surface (100) and (111), magnetic poly-domain and mono-domain by feild-cooling, as well as two different thicknesses 1 mm and 50 um. Comparison of the static illumination with variable number of pulses and intensity showed that high-repetition rate bright XFEL beam has a not only heating up effect, which may influence studied magnetic dynamics and mix up measurements with theoretically predicted behaviour, but also act as a sort of pump on its own, inducing more complex dynamics. In this regard, as a part of preparation for any experiment on crystalline sample, it is absolutely necessary to evaluate the sensitivity of the sample to the desired emission parameter, especially for low-intensity reflections that require either long illumination or high incident intensity. Despite the lack of information about this detrimental effect, we conducted a series of temperature measurements on both charge and spin density waves. The CDW reflection demonstrated decrease of the wave vector value caused by temperature decrease, which is a good agreement with theoretical calculation based on lattice and incommensurability parameter. The same measurements for low

intense SDW peaks turned out to be more tricky. Two reflections were found on the angular positions for SDW(001-δ) and SDW(001+δ) satellites, however only one of them had wave vector dynamics aligned with theoretical trend. In addition to this, temperature dependence of intensity curves do not have pronounced drop due to the spin-flip transition, which was proved to be around 123 K for both samples using SQUID magnetometer. Due to the assumption that in magnetic poly domain sample in the spin polarisation transition equal redistribution between of the intensity between different domains can occur, the field-cooling procedure was applied on one of the samples. Despite this special preparation, the temperature dependence curve have only a slight change, which might be connected with the heating up effect of X-ray beam, which ruined the effect of field-cooling. Also this might change transition point, since the sensor readings differ from the temperature of the upper layers of the sample, which are most involved in the formation of reflection. As part of the confirmation of the magnetic nature of the found reflections, they were tracked also along with the warming up over Neel temperature. Here the transition from ferromagnetic to paramagnetic state showed up as an intensity decrease and disappearance of reflection from the detector. Finally, we did not see any kind of changed in bot CDW and SDW reflections with application of magnetic field up to 12.5 T neither about nor below assumed spin-flip transition temperature. However, even with very limited literature overview on this topic, there is a number of technical reasons, which might cause absence of effect: as we mentioned above. We could be out of spin-flip transition area due to wrong choice of illumination parameters for Cr sample, the modification out for this part of experiment is coming from the radiation damage part results. Also, we assume that we just got close to the required power of magnetic field to trigger the rotation of magnetic moment, thus more stable operation accompanied with split-coil modifications would allow to repeat this measurement in the desired range of B-fields. Finally, it is needed to try other geometries for this experiment such as a transmission, which is already implemented in the setup and magnetic field aligned with the tracked reflection, which require either different sample orientation or holder modification. We are sure that this experiment has an interesting perspective and need to be repeated with several preparation steps in advance. In this thesis, we presented new setup and new type of pump-probe method that gives wide range of experimental possibilities in MID instrument at Euroepan XFEL.

Bibliography

[1] Louis Néel. "Magnetism and Local Molecular Field." In: *Science* 174.4013 (Dec. 1971), pp. 985–992.

[2] Ignasi Fina and Xavier Marti. "Electric control of antiferromagnets." en. In: *IEEE Transactions on Magnetics* (2016), pp. 1–1.

[3] T. McGuire and R. Potter. "Anisotropic magnetoresistance in ferromagnetic 3d alloys." In: *IEEE Transactions on Magnetics* 11.4 (July 1975), pp. 1018–1038.

[4] Zhiqi Liu et al. "Antiferromagnetic Piezospintronics." en. In: *Advanced Electronic Materials* 5.7 (2019), p. 1900176.

[5] T. Jungwirth et al. "Antiferromagnetic spintronics." en. In: *Nature Nanotechnology* 11.3 (Mar. 2016), pp. 231–241.

[6] Claude Berthier and Laurent P. Levy. *High Magnetic Fields: Applications in Condensed Matter Physics and Spectroscopy*. en. Springer Science & Business Media, 2001.

[7] Koichi Katsumata. "Synchrotron X-Ray Diffraction Studies of Magnetic Materials under Extreme Conditions." en. In: *Physica Scripta* (2005).

[8] V. L. R. Jacques et al. "Laser-Induced Charge-Density-Wave Transient Depinning in Chromium." en. In: *Physical Review Letters* 117.15 (Oct. 2016), p. 156401.

[9] M. Yabashi et al. "Design of a beamline for the SPring-8 long undulator source 1." en. In: *Nuclear Instruments and Methods in Physics Research Section A: Accelerators, Spectrometers, Detectors and Associated Equipment* 467-468 (July 2001), pp. 678–681.

[10] Peter J. E. M Van Der Linden et al. "The ESRF Miniature Pulsed Magnetic Field System." en. In: Melbourne (Australia), 2010, pp. 107–110.

[11] Peter J. E. M. Van Der Linden et al. "Miniature pulsed magnet system for synchrotron x-ray measurements." en. In: *Review of Scientific Instruments* 79.7 (July 2008), p. 075104.

[12]   A. Madsen et al. "Materials Imaging and Dynamics (MID) instrument at the European X-ray Free-Electron Laser Facility." en. In: *Journal of Synchrotron Radiation* 28.2 (Mar. 2021), pp. 637–649.

[13]   *All segments of first light-generating system installed in European XFEL.* URL: https://www.xfel.eu/news_and_events/news/index_eng.html?openDirectAnchor=1299&two_columns=0 (visited on 08/14/2023).

[14]   Valerio Cerantola et al. "New frontiers in extreme conditions science at synchrotrons and free electron lasers." en. In: *Journal of Physics: Condensed Matter* 33.27 (July 2021), p. 274003.

[15]   Ilia Petrov et al. "Effect of Heat Load on Cryo-Cooled Monochromators at the European X-Ray Free-Electron Laser: Simulations and First Experimental Observations." en. In: *Proceedings of the 39th Free Electron Laser Conference* FEL2019 (2019), 4 pages, 0.464 MB.

[16]   T. Roth et al. "Pulse-resolved intensity measurements at a hard X-ray FEL using semi-transparent diamond detectors." en. In: *Journal of Synchrotron Radiation* 25.1 (Jan. 2018), pp. 177–188.

[17]   J. Strempfer et al. "Resonant scattering and diffraction beamline P09 at PETRA III." en. In: *Journal of Synchrotron Radiation* 20.4 (July 2013), pp. 541–549.

[18]   Y. H. Matsuda et al. "High Field X-ray Diffraction Study on a Magnetic-Field-Induced Valence Transition in YbInCu$_4$." en. In: *Journal of the Physical Society of Japan* 75.2 (Feb. 2006), p. 024710.

[19]   Zahirul Islam et al. "A portable high-field pulsed-magnet system for single-crystal x-ray scattering studies." en. In: *Review of Scientific Instruments* 80.11 (Nov. 2009), p. 113902.

[20]   Fritz Herlach. "Strong and ultrastrong pulsed magnetic fields." en. In: *Journal of Magnetism and Magnetic Materials* 11.1 (Apr. 1979), pp. 300–307.

[21]   F. Herlach, T. Peng, and J. Vanacken. "Elements of pulsed magnet design." en. In: *Journal of Physics: Conference Series* 51.1 (Nov. 2006), p. 599.

[22]   F Cau, P Bruzzone, and M Vögel. "Design study of a superconducting magnet system for the European Synchrotron Radiation Facility." en. In: *Superconductor Science and Technology* 23.5 (May 2010), p. 055006.

[23] L. Pust. "A simple continuous-flow helium cryostat for magnetic measurements." en. In: *Journal of Physics E: Scientific Instruments* 15.10 (Oct. 1982), p. 1013.

[24] S. Hauf et al. "The Karabo distributed control system." en. In: *Journal of Synchrotron Radiation* 26.5 (Sept. 2019), pp. 1448–1461.

[25] W Lenz. "Beitrag zum Verständnis der magnetischen Erscheinungen in festen Körpern." In: *Z. Phys.* 21 (1920), pp. 613–615.

[26] R. Peierls. "On Ising's model of ferromagnetism." en. In: *Mathematical Proceedings of the Cambridge Philosophical Society* 32.3 (Oct. 1936), pp. 477–481.

[27] Ernst Ising. "Beitrag zur Theorie des Ferromagnetismus." de. In: *Zeitschrift für Physik* 31.1 (Feb. 1925), pp. 253–258.

[28] Sacha Friedli and Yvan Velenik. *Statistical Mechanics of Lattice Systems: A Concrete Mathematical Introduction.* Cambridge: Cambridge University Press, 2017.

[29] J. J. Sakurai. *Modern Quantum Mechanics, Revised Edition.* Revised Edition. Addison Wesley Longman, Jan. 1994.

[30] Joachim Stöhr and Hans Christoph Siegmann. *Magnetism.* en. Berlin, Heidelberg: Springer, 2006.

[31] N. Mermin and Neil Ashcroft. *Solid State Physics.* English. New ed edition. New York: Brooks/Cole, Jan. 1976.

[32] Walter Greiner, Ludwig Neise, and Horst Stöcker. *Thermodynamics and Statistical Mechanics.* New York, NY: Springer, 1995.

[33] Jens Jensen and Allan R Mackintosh. "Structures and Excitations." en. In: ().

[34] R. J. Elliott. "Phenomenological Discussion of Magnetic Ordering in the Heavy Rare-Earth Metals." en. In: *Physical Review* 124.2 (Oct. 1961), pp. 346–353.

[35] Stephen Blundell. *Magnetism in Condensed Matter (Oxford Master Series in Physics).*

[36] Takeo Nagamiya. "Helical Spin Ordering-1 Theory of Helical Spin Configurations." en. In: *Solid State Physics.* Vol. 20. Elsevier, 1968, pp. 305–411.

[37] Wolfgang Nolting and Anupuru Ramakanth. *Quantum Theory of Magnetism.* en. Berlin, Heidelberg: Springer Berlin Heidelberg, 2009.

[38] *The Annals of Electricity, Magnetism, and Chemistry; and Guardian of Experimental Science.* en. 1842.

[39] M. Doerr *, M. Rotter, and A. Lindbaum. "Magnetostriction in rare-earth based antiferromagnets." In: *Advances in Physics* 54.1 (Jan. 2005), pp. 1–66.

[40] Takeo Nagamiya, Kazukiyo Nagata, and Yoshiharu Kitano. "Magnetization Process of a Screw Spin System." en. In: *Progress of Theoretical Physics* 27.6 (June 1962), pp. 1253–1271.

[41] Hiroyuki Ohsumi. "Magnetoelastic Effect in Holmium Studied by X-Ray Diffraction." en. In: *Journal of the Physical Society of Japan* 71.7 (July 2002), pp. 1732–1739.

[42] A. W. Overhauser. "Spin Density Waves in an Electron Gas." en. In: *Physical Review* 128.3 (Nov. 1962), pp. 1437–1452.

[43] Herbert Fröhlich. "On the theory of superconductivity: the one-dimensional case." In: *Proceedings of the Royal Society of London. Series A. Mathematical and Physical Sciences* 223.1154 (May 1954), pp. 296–305.

[44] Rudolf Ernst Peierls. *Quantum Theory of Solids*. en. Clarendon Press, 1955.

[45] G. Grüner. "The dynamics of spin-density waves." en. In: *Reviews of Modern Physics* 66.1 (Jan. 1994), pp. 1–24.

[46] George Grüner. *Density waves in solids*. en. Frontiers in physics v. 89. Reading, Mass: Addison-Wesley Pub. Co., Advanced Book Program, 1994.

[47] David Phillips. "William Lawrence Bragg. 31 March 1890-1 July 1971." In: *Biographical Memoirs of Fellows of the Royal Society* 25 (1979), pp. 75–143.

[48] Jens Als-Nielsen and Des McMorrow. *Elements of Modern X-ray Physics*.

[49] Charles Kittel. *Introduction to solid state physics*. en. 8th ed. Hoboken, NJ: Wiley, 2005.

[50] M.J. Cooper. "Magnetic Compton scattering from HoFe2." en. In: *Physica B: Condensed Matter* 192.1-2 (Oct. 1993), pp. 191–199.

[51] J. Strempfer et al. "The non-resonant magnetic X-ray scattering cross-section for photon energies up to 500 keV." en. In: *Europhysics Letters* 40.5 (Dec. 1997), p. 569.

[52] Doon Gibbs et al. "Polarization and resonance studies of x-ray magnetic scattering in holmium." en. In: *Physical Review B* 43.7 (Mar. 1991), pp. 5663–5681.

[53] Paul G Evans and Eric D Isaacs. "Magnetic x-ray microdiffraction." en. In: *Journal of Physics D: Applied Physics* 39.15 (Aug. 2006), R245–R263.

[54] O Klein and Y Nishina. "Uber die Streuung yon Strahlung durch freie Elektronen nach der neuen relativistischen Quantendynamik yon Dirac." de. In: ().

[55] M. Blume and Doon Gibbs. "Polarization dependence of magnetic x-ray scattering." en. In: *Physical Review B* 37.4 (Feb. 1988), pp. 1779–1789.

[56] Bellec Ewen. "Study of charge density wave materials under current by X-ray diffraction." PhD thesis. Nov. 2019.

[57] N. V. Latukhin, V. A. Rozhkov, and I. V. Seliverstova. "Chemical etching of rare earth metal oxides." ru. In: *Fizika I Khimiya Obrabotki Materialov* 5 (1996).

[58] K. Sangwal. *Etching of Crystals*. 1990.

[59] G. Petzow. *Metallographic Etching, 2nd Edition: Techniques for Metallography, Ceramography, Plastography*. en. ASM International, Jan. 1999.

[60] P Marcon and K Ostanina. "Overview of Methods for Magnetic Susceptibility Measurement." en. In: (2012).

[61] M. Buchner et al. "Tutorial: Basic principles, limits of detection, and pitfalls of highly sensitive SQUID magnetometry for nanomagnetism and spintronics." en. In: *Journal of Applied Physics* 124.16 (Oct. 2018), p. 161101.

[62] V A Finkel' and V V Vorob'Ev. "Crystal structure of dysprosium at 77-300°K." en. In: ().

[63] A. S. Chernyshov et al. "Magnetic and magnetocaloric properties and the magnetic phase diagram of single-crystal dysprosium." en. In: *Physical Review B* 71.18 (May 2005), p. 184410.

[64] J. Yu et al. "Exploring the magnetic phase diagram of dysprosium with neutron diffraction." en. In: *Physical Review B* 91.1 (Jan. 2015), p. 014404.

[65] A. S. Chernyshov et al. "Temperature and magnetic field-dependent x-ray powder diffraction study of dysprosium." en. In: *Physical Review B* 77.9 (Mar. 2008), p. 094132.

[66] Yoshitoshi Kida et al. "Effect of Magnetic Field on Crystal Lattice in Dysprosium Studied by X-Ray Diffraction." In: *Journal of the Physical Society of Japan* 68.2 (Feb. 1999), pp. 650–654.

[67] F. J. Darnell and E. P. Moore. "Crystal Structure of Dysprosium at Low Temperatures." en. In: *Journal of Applied Physics* 34.4 (Apr. 1963), pp. 1337–1338.

[68] Tomohisa Izawa et al. "Magnetic Phase Diagram of Dy Determined by AC Calorimetry." en. In: *Journal of the Physical Society of Japan* 65.8 (Aug. 1996), pp. 2640–2644.

[69] A. E. Clark, B. F. DeSavage, and R. Bozorth. "Anomalous Thermal Expansion and Magnetostriction of Single-Crystal Dysprosium." en. In: *Physical Review* 138.1A (Apr. 1965), A216–A224.

[70] U. Enz. "Magnetization Process of a Helical Spin Configuration." In: *Journal of Applied Physics* 32.3 (Aug. 2009), S22–S26.

[71] E. W. Lee. "The magnetoelastic behaviour of antiferromagnets having helical spin configurations." en. In: *Proceedings of the Physical Society* 84.5 (Nov. 1964), p. 693.

[72] N Wakabayashi, J.W Cable, and J.L Robertson. "Magnetic structures of Dy in applied fields." en. In: *Physica B: Condensed Matter* 241-243 (Dec. 1997), pp. 517–523.

[73] J. P. Hill, G. Helgesen, and Doon Gibbs. "X-ray-scattering study of charge- and spin-density waves in chromium." en. In: *Physical Review B* 51.16 (Apr. 1995), pp. 10336–10344.

[74] V. L. R. Jacques et al. "Charge- and spin-density waves observed through their spatial fluctuations by coherent and simultaneous x-ray diffraction." en. In: *Physical Review B* 89.24 (June 2014), p. 245127.

[75] P. G. Evans et al. "X-ray Microdiffraction Images of Antiferromagnetic Domain Evolution in Chromium." en. In: *Science* 295.5557 (Feb. 2002), pp. 1042–1045.

[76] Yejun Feng et al. "Pressure-Tuned Spin and Charge Ordering in an Itinerant Antiferromagnet." en. In: *Physical Review Letters* 99.13 (Sept. 2007), p. 137201.

[77] D. Lamago et al. "Measurement of strong phonon softening in Cr with and without Fermi-surface nesting by inelastic x-ray scattering." en. In: *Physical Review B* 82.19 (Nov. 2010), p. 195121.

[78] O. G. Shpyrko et al. "Direct measurement of antiferromagnetic domain fluctuations." en. In: *Nature* 447.7140 (May 2007), pp. 68–71.

[79] C. Y. Young and J. B. Sokoloff. "The role of harmonics in the first order antiferromagnetic to paramagnetic transition in chromium." en. In: *Journal of Physics F: Metal Physics* 4.8 (Aug. 1974), p. 1304.

[80] Y. Tsunoda et al. "Strain wave in pure chromium." en. In: *Solid State Communications* 14.3 (Feb. 1974), pp. 287–289.

[81] L. M. Corliss, J. M. Hastings, and R. J. Weiss. "Antiphase Antiferromagnetic Structure of Chromium." en. In: *Physical Review Letters* 3.5 (Sept. 1959), pp. 211–212.

[82] V. N. Bykov et al. In: 4 (1958), p. 1149.

[83] Eric Fawcett. "Spin-density-wave antiferromagnetism in chromium." en. In: *Reviews of Modern Physics* 60.1 (Jan. 1988), pp. 209–283.

[84] Hartmut Zabel. "Magnetism of chromium at surfaces, at interfaces and in thin films." en. In: *Journal of Physics: Condensed Matter* 11.48 (Dec. 1999), pp. 9303–9346.

[85] P. G. Evans et al. "X-ray Microdiffraction Images of Antiferromagnetic Domain Evolution in Chromium." en. In: *Science* 295.5557 (Feb. 2002), pp. 1042–1045.

[86] D. Mannix et al. "The chromium spin density wave: magnetic X-ray scattering studies with polarisation analysis." en. In: *The European Physical Journal B* 20.1 (Mar. 2001), pp. 19–25.

[87] V. L.R. Jacques et al. "Spin density wave dislocation in chromium probed by coherent X-ray diffraction." en. In: *The European Physical Journal B* 70.3 (Aug. 2009), pp. 317–325.

[88] P.C. De Camargo et al. "Origin of single Q charge-density wave domains in chromium." en. In: *Journal of Magnetism and Magnetic Materials* 233.1-2 (July 2001), pp. 65–68.

[89] C. W. Nicholson et al. "Ultrafast Spin Density Wave Transition in Chromium Governed by Thermalized Electron Gas." en. In: *Physical Review Letters* 117.13 (Sept. 2016), p. 136801.

[90] A. Singer et al. "Photoinduced Enhancement of the Charge Density Wave Amplitude." en. In: *Physical Review Letters* 117.5 (July 2016), p. 056401.

[91] A. Arrott, S. A. Werner, and H. Kendrick. "First-Order Magnetic Phase Change in Chromium at 38.5°C." en. In: *Physical Review Letters* 14.25 (June 1965), pp. 1022–1024.

[92] B.R. Watts. "The De Haas-Van Alphen effect in chromium and the magnetic structure." en. In: *Physics Letters* 10.3 (June 1964), pp. 275–276.

[93] S. A. Werner, A. Arrott, and H. Kendrick. "Changes in Apparent Symmetry with Magnetic Field in Chromium." en. In: *Journal of Applied Physics* 37.3 (Mar. 1966), pp. 1260–1261.

[94]   B. J. Sternlieb et al. "Silent Satellites: Critical Fluctuations in Chromiun." en. In: *Physical Review Letters* 75.3 (July 1995), pp. 541–544.

[95]   Y Tsunoda and R M Nicklow. "Spin-density waves in Cr under a magnetic field." en. In: *Journal of Physics: Condensed Matter* 8.15 (Apr. 1996), pp. 2655–2662.

[96]   A. W. Overhauser. "Observability of Charge-Density Waves by Neutron Diffraction." In: *Physical Review B* 3.10 (May 1971), pp. 3173–3182.

[97]   M. Blume. "Magnetic scattering of x rays (invited)." In: *Journal of Applied Physics* 57.8 (Apr. 1985), pp. 3615–3618.

[98]   I. Petrov. "Characterization and tailoring of MHz-repetition-rate XFEL pulses using dynamical diffraction in crystals." eng. PhD thesis. Universität Hamburg Hamburg, 2022.

[99]   S. A. Werner, A. Arrott, and H. Kendrick. "Temperature and Magnetic-Field Dependence of the Antiferromagnetism in Pure Chromium." en. In: *Physical Review* 155.2 (Mar. 1967), pp. 528–539.

[100] P. Böni et al. "Polarization dependence of the magnetic fluctuations in Cr below T N." en. In: *Physical Review B* 57.2 (Jan. 1998), pp. 1057–1065.

[101] P J Brown et al. "Some observations on the higher temperature antiferromagnetic phase of chromium." en. In: *Proceedings of the Physical Society* 85.6 (June 1965), pp. 1185–1189.

[102] T J Bastow and R Street. "The antiferromagnetic phases of field-cooled chromium." en. In: *Proceedings of the Physical Society* 86.5 (Nov. 1965), pp. 1143–1145.

[103] B. Efron. "Bootstrap Methods: Another Look at the Jackknife." In: *The Annals of Statistics* 7.1 (1979), pp. 1–26.

[104] Kandethody M. Ramachandran and Chris P. Tsokos. "Chapter 13 - Empirical methods." en. In: *Mathematical Statistics with Applications in R (Third Edition)*. Ed. by Kandethody M. Ramachandran and Chris P. Tsokos. Academic Press, Jan. 2021, pp. 531–568.

Acknowledgement